NONLINEAR PLASMONICS WITH APPLICATIONS TO SENSING

by

Franklin Mbende Che

Submitted in partial fulfillment of the requirements
for the degree of Doctor of Philosophy

at

Dalhousie University
Halifax, Nova Scotia
September 2017

I dedicate this thesis to my dear wife Mavis Che Mbende for her endless love, sacrifice, support and superhuman patience.

Table of Contents

List of Tables

List of Figures

Abstract

Recent progress in laser science has led to the development of ultrashort pulses, which have a broad spectral bandwidth and high peak intensities. When these pulses interact with nonlinear plasmonic materials, the combination of high peak powers and large bandwidth opens up new possibilities of novel nonlinear spectral effects and potential applications.

In this dissertation, we study the nonlinear optical effects of generating second-order electromagnetic fields in reflection from a conducting thin film close to surface plasmon resonance using an ultrashort polychromatic light source. Suitable and realistic femtosecond polychromatic incident sources were formulated for these studies, and the nonlinear fields generated from these sources are explored. The potential of using such a system as a nonlinear refractive index sensor was also investigated leading to the following results.

1- It was demonstrated for the first time, to the best of our knowledge, the generation of plasmon enhanced sum- and difference-frequency waves from the surface of a metal thin film using a single polychromatic source. We used ultrashort femtosecond Gaussian and dual-wavelength Gaussian pulses to generate sum- and difference-frequency waves, respectively. Nonlinear waves in the visible and mid infra-red range were generated with a very strong enhancement of the nonlinear waves close to surface plasmon resonance of the incident light source.

2- Spectral shifts and switches in the nonlinear spectra reflected from a metal film, were observed close to surface plasmon resonance. We also demonstrated a strong correlation between these spectral effects and properties of the incident wave such as the pulse duration, with stronger effects observed for shorter pulses. Finally, we demonstrated a strong dependence of the reflected nonlinear spectral peak position on the material properties of the dielectric material surrounding the metal film.

3- A simple, robust and high sensitivity refractive index sensor was proposed and investigated, based on the second-order nonlinear processes of sum- and difference-frequency generation. The calculated sensor performance parameters showed very high sensitivity and figure of merit values with the ability to operate over a wide wavelength range. We demonstrated a spectral sensitivity at mid-infrared wavelengths, that was two orders of magnitude higher than current values available in the literature.

4- Successful estimation of the relative strengths of second-harmonic generation, reflected from a large variety of conducting thin films using an infrared femtosecond laser source. The films were sputtered on a glass substrate with thickness of 50nm and 100 nm. We also showed that the second-harmonic generation intensities from tungsten and antimony were comparable to that of silver and gold.

List of Abbreviations and Symbols Used

$A(\omega)$	Spectral amplitude
D	External flux density
$E^{<}$	Electric field at lower metal interface
$E^{>}$	Electric field at upper metal interface
L_{spp}	SPP propagation length
L_z	SPP decay length
$P^{<}$	Nonlinear polarization at lower metal interface
$P^{>}$	Nonlinear polarization at upper metal interface
P_{3z}^{S}	Surface sum-frequency polarization
P_L	Linear polarization
P_{NL}	Nonlinear polarization
P_S	Surface polarization
$S(\lambda)$	Wavelength sensitivity
$S(\omega)$	Energy spectrum of a polychromatic wave
$S_n(z)$	Source term at frequency ω_n
U/N	Average energy of a fermion
$\Delta\lambda$	Spectral shift
Δn	Change in refractive index
$\Delta\omega$	Pulse bandwidth
Γ	Collision frequency
β	SPP wave vector
β'	Real part of complex SPP propagation constant
β''	Complex part of complex SPP propagation constant
β_{spp}	Complex SPP propagation constant
$\chi^{(n)}$	n^{th} -order susceptibility
$\chi_S^{(n)}$	n^{th} -order surface susceptibility
κ	Complex SPP decay constant
λ_c	Spectral minimum of reflected wave

$\mathcal{E}(\mathbf{r},\omega)$	Complex electric field amplitude
$\mathcal{H}(\mathbf{r},\omega)$	Complex magnetic field amplitude
μ_0	Free space permeability
ω	Optical frequency
ω_b	Bulk plasma frequency
ω_p	Plasma frequency
ω_{sp}	Surface plasmon frequency
τ	Relaxation time
$\theta_0(\omega)$	Fundamental wave angle of incidence
$\theta_c(\omega)$	SPP coupling angle
$\tilde{r}_{\alpha\beta}$	Fresnel reflection coefficient for TM light between media α and β
ε_0	Free space permittivity
ε_∞	Static dielectric constant
ε_j	Relative permittivity of medium j
$a(\omega_i,\omega_j)$	Second-order susceptibility dimensionless parameter, $(i,j=1,2)$
$b(\omega_i,\omega_j)$	Second-order susceptibility dimensionless parameter, $(i,j=1,2)$
d	Thickness of metal film in Kretschmann configuration
e	Electronic charge
k_x	Transverse SPP propagation constant
m_{eff}	Effective mass
$n(z,t)$	Carrier density
$n_0(z)$	Equilibrium carrier density profile
$p(n)$	Thomas-Fermi pressure
$r_{\alpha\beta}$	Coefficient of reflection between media α and β
r_{ij}	Coefficient of reflection between media i and j
t_{ij}	Coefficient of transmission between media i and j
t_p	Pulse duration
$u(z,t)$	Carrier velocity field

Ag	Silver
Al	Aluminum
Au	Gold
Co	Cobalt
Cr	Chromium
DFG	Difference-frequency generation
DFW	Difference-frequency wave
FCC	Face-centered cubic
FOM	Figure of merit
FW	Fundamental wave
Ge	Germanium
HD	Hydrodynamic
ITO	Indium tin oxide
LSP	Local Surface plasmon
MIR	Mid-infrared
Ni	Nickel
Sb	Antimony
SFG	Sum-frequency generation
SFG	Sum-frequency wave

SHG	Second-harmonic generation
Si	Silicon
SNR	Signal to noise ratio
SP	Surface plasmon
SPP	Surface plasmon polaritons
SPR	Surface plasmon resonance
THG	Third-harmonic generation
Ti	Titanium
TiN	Titanium nitride
W	Tungsten
Zn	Zinc

Acknowledgements

My profound gratitude and appreciation goes out to Dr. Sergey Ponomarenko and Dr. Michael Cada for their guidance, continuous support and encouragement during my Ph.D studies. Dr. Ponomarenko was very helpful, understanding and patient during my transition from experimental to theoretical based research. Dr. Cada's constant push towards research independence and insightful discussions were helpful in developing the critical thinker and independent researcher in me. I am greatly indebted to Dr. Serge Grabtchak, who first offered me the opportunity to pursue doctoral studies under his guidance at Dalhousie University. I learned a lot from him during those early years of my studies and would not be here without his support .

I would also like to thank my other supervisory committee member, Dr. William Whelan for his support and encouragement during my studies. Bill made the first two years of this process possible through funding from the university of Prince Edwards Island.

I am thankful to all members past and present of the "Theoretical Optics and Plasmonics" and "Photonics" groups at Dalhousie University, who contributed to my thesis. Special thanks goes to Dr. Mohamed Eldlio, Dr. Laleh Mokhtarpour, Dr. Daniela Valente, Dr. Mumuni Amadu and Dr. Nghia Nguyen-Huu for their encouragement, support and many lively discussions.

I am grateful to my parents, Joseph and Mariana for their love, sacrifice and support. A huge thank you goes out to my siblings Mirabel, Gerald, Linda, Stella, Modesius, Emmanuel and Mariana. Graciana my love, I still cant believe you are gone, I could not have done it without your love and direction, until we meet again. Belinda dear, thank you for all those warm meals and advice in Buea. I am also extremely indebted to Linda and David for opening up their home and hearts to my family and for their continuous moral support.

Chelsy and Nathan, daddy finally made it, we can now move out of Peter Green Hall. To God be the glory.

Chapter 1

Introduction

1.1 Preface

In this thesis, we focus on the nonlinear interaction of polychromatic light within a thin metal film deposited on a glass prism in the Kretschmann geometry and its application as a refractive index sensor. This chapter starts with an introduction to the general theme of our thesis. Then, thesis objectives, contributions, and organization are presented.

1.2 Thesis Theme

The invention of the first laser in 1960 by Maiman [4] opened up new areas of research and applications. One such area was the field of nonlinear optics, which was the first and largest field to benefit from the invention of the laser [5]. The first experimental observation of second-harmonic generation (SHG) and sum-frequency generation (SFG) by Franken et al [6] in quartz heralded a period of rapid development in the field of nonlinear optics.

Early experiments in nonlinear optics were based on the bulk nonlinearity of dielectric crystals [7–10]. The theory of the generation of harmonic light at the boundary of a nonlinear dielectric medium was subsequently developed [11] and experimentally observed in reflection from non-centrosymmetric semiconductor interfaces [12]. Further studies in surface nonlinearities led to the first observation of SHG from the surface of a conducting centrosymmetric material [13], with the lack of symmetry at the surface creating a nonlinear surface susceptibility. This surface nonlinearity accounts for the generated second harmonic field, since most centrosymmetric materials have a negligible bulk nonlinearity.

Over the years since the first observation of SHG from metal surfaces, very little was done in the field of surface nonlinearities in metals and the experiments during this time were geared towards proving theoretical predictions of SHG rather than exploring the potential applications of this surface nonlinearity [5]. This all changed with new developments in the field of surface plasma waves, which were first theoretically analyzed by

Ritchie in 1957 [14] and latter experimentally excited by Otto [15] and Kretschmann [16]. The propagation of electromagnetic waves at the surface of conducting media had been studied before as early as the beginning of the 20th century by Zeneck [17] and Sommerfeld [18] in the framework of the interaction of radio waves with the Earth. The benefits of combining the fields of surface harmonic generation and surface plasmons (SP) was first demonstrated by Simon et al [19], where they observed an enhancement of the optical SHG field reflected from a silver surface due to the excitation of surface plasmons. Another effect that also helped attract renewed interest to this field was the discovery of surface-enhanced Raman scattering (SERS) in 1974 by Fleishman et al. [20], who demonstrated a six order-of-magnitude increase in the Raman output from molecular adsorbates on a roughened silver surface. This ushered in the field of nonlinear plasmonics. Since then, there has been a lot of fundamental research in this field directed towards generation, modification and enhancement of harmonic frequencies [21–26]. The field of nonlinear plasmonics has dedicated the bulk of its research to the study of second-order nonlinear effects such as SHG, SFG and difference-frequency generation (DFG). This is primarily due to the fact that it is easier to measure them experimentally compared to higher order nonlinear effects such as third harmonic generation (THG), whereby increasing the incident source intensity to compensate for the small THG susceptibilities can lead to material damage. The ability to discriminate the bulk from the surface contribution to the second-order nonlinear field generated from most metals [24, 27] also makes these effects desirable. These second-order reflected fields have found a wide range of applications such as nonlinear spectroscopy [28–32], microscopy [33–36], sensing [37–41], nonlinear optical frequency conversion processes [42–44] development of coherent light sources [45–49] and surface studies [50–52]. A great portion of these applications are based on nano-plasmonic structures, which have become increasingly easy to fabricate, synthesize and manipulate, thanks to rapid developments in the field of nano-fabrication [53].

Most of the applications mentioned above are based on quasi-monochromatic incident light sources with very narrow bandwidths, where there is negligible interaction between different frequency components within the bandwidth of the incident fundamental wave (FW). Applications such as sum- and difference-frequency spectroscopy [54, 55] and generation of mid-infrared ultra short pulses [56, 57] involves frequency mixing of two distinct monochromatic laser sources. However, with recent developments of ultrashort laser

pulses [58, 59], we have input pulses with bandwidths spanning over a wide frequency range making them polychromatic. There is a possibility of frequency components within the bandwidth of the polychromatic source to interact nonlinearly in very interesting ways close to plasmon resonance. To the best of our knowledge, there is very little research done on plasmon assisted nonlinear effects in metal thin films using polychromatic light sources, making it an important area to explore.

1.3 Thesis Objectives

The main goal of this body of research is to explore the optical effects of generating second-order optical signals in reflection from a metal thin film close to SP resonance using a polychromatic light source and the potential applications of these effects. We attain this objective by exploring in detail the topics below.

1. We plan to study the generation of sum-frequency and difference-frequency waves using the Kretschmann configuration and a single polychromatic incident light source. Both nonlinear waves are usually generated using two distinct quasi-monochromatic sources. We aim to use a single polychromatic source to achieve this through the surface nonlinearity of the metal film.

2. We aim to explore the spectral effects in the generated nonlinear fields and the dependence of these effects on the incident pulse properties and material parameters. We use femtosecond pulses as our incident light source, with the pulse duration determining the bandwidth of the pulse as well as the range of frequencies within the bandwidth. Thus, we expect the incident pulse duration to be an important variable in our nonlinear studies.

3. We intend to investigate the potential use of these reflected nonlinear fields to design a robust and high sensitivity refractive index sensor. Using the Kretschmann geometry for illumination, we expect the nonlinear signal to be affected by the refractive index of the material surrounding the thin film. We hope to exploit this for refractive index sensing applications.

4. We explore the SHG of a variety of conducting thin films, to determine their suitability in sensor applications. Since experimental data for nonlinear parameters of metal thin films are difficult to come by, we expect to gain insight into the relative intensity of nonlinear signals reflected from different thin films, by investigating the SHG signal reflected from these films at normal incidence.

1.4 Thesis Contribution

The set objectives in this study were all met with the results published as journal papers. The journal papers have been included in the thesis as chapters. My contributions are summarized below,

1. We assisted in developing the theory of reflected SFG from a gold thin film on a glass prism in the Kretschmann configuration using a polychromatic source after investigating reflected SHG from the same geometry [60].

2. Developed the theory and simulated the generation of difference-frequency light through reflection from a gold film in the Kretschmann configuration. Specifically, we demonstrated the generation of MIR wave using an incident ultrashort dual-wavelength gaussian pulse at optical frequencies. There was a very strong enhancement of the difference-frequency wave close to the surface plasmon resonance (SPR) of the incident light source [61].

3. Demonstrated spectral shifts and switches in the reflected difference-frequency wave close to plasmon resonance and was able to correlate this effects to the properties of the incident FW such as the pulse duration, with stronger effects for shorter pulses. We also demonstrated a strong dependence of the reflected nonlinear spectral peak position to the material properties of the dielectric material surrounding the metal film [61].

4. Proposed a simple yet robust refractive index sensor, based on the second-order processes of sum- and difference-frequency generation. The calculated sensor performance parameters showed very high sensitivity and figure of merit (FOM) values, coupled with its ability to operate over a wide wavelength range [62].

5. Finally we successfully estimated the relative strengths of SHG waves, reflected from a large variety of conducting thin films using an infrared femtosecond laser source. Information gathered from this study can be used to determine suitable conducting thin films for our proposed nonlinear plasmonic sensor [63].

1.5 Thesis Organization

This thesis is in a paper-based format. We start with a brief introduction of the scope of the thesis, followed by a presentation of the key theoretical concepts used in our study. We then include the published journal articles and present concluding remarks at the end.

Chapter 1 presents the general theme, objectives and contribution of the thesis. The remainder of the thesis is organized as follows.

Chapter 2 covers the fundamental electromagnetic theory of SPPs, their dispersion relation and SPP coupling techniques. A general overview of linear refractive index plasmonic sensors is presented. We discuss different sensor configurations, performance parameters and limitations.

Chapter 3 introduces the concept of optical nonlinearity, focusing on the second order nonlinear effects of SHG, SFG and DFG. We also discuss the theoretical formulation of the nonlinear surface susceptibility of metals and conclude with a theoretical description of the polychromatic sources used in our studies.

Chapter 4 focuses on the generation of MIR light using the nonlinear process of DFG. Spectral effects in the reflected nonlinear wave close to plasmon resonance are presented with its potential for use as a refractive index sensor also demonstrated.

Chapter 5 proposes a Kretschmann-based nonlinear refractive index sensor. Both the SFG- and DFG-based sensors are presented, with their wavelength sensitivities and FOM calculated. An estimation of the signal strength and limitation of the sensor is also presented.

Chapter 6 covers the relative SHG generation characterization of a variety of conducting thin films in reflection. We discuss the deposition of the films and measurement technique used to characterize the thin films. The strength of the reflected nonlinear signals from the thin films is also estimated.

Chapter 7 summarizes the main results from this study and provides suggestions for future work.

Chapter 2

Surface Plasmon Polaritons (SPPs)

The aim of this chapter is to briefly describe the general concept of surface plasmon polaritons at the interface between a conductor and a dielectric medium. We lay out the theoretical formulations of surface plasmon waves on thick and thin metal films and discuss different surface plasmon coupling geometries.

We conclude the chapter by reviewing at SPP based refractive index sensing, with a presentation of the sensing performance parameters and their limitations.

2.1 SPP Theory

SPPs are propagating electromagnetic waves at an interface separating a dielectric from a conductor, which are evanescently confined in the direction normal to the interface. SPPs arise via electromagnetic field coupling to free electrons inside the conductor [64]. This confinement leads to electromagnetic field enhancement at the interface, resulting in SPPs being very sensitive to surface conditions.

2.1.1 Two Semi-Infinite Media

Let us consider two semi-infinite nonmagnetic media shown in Fig. 2.1, where $\varepsilon_1(\omega)$ and ε_2 represent the relative permittivities of metal and dielectric, respectively. To examine SPP properties, we apply Maxwell's equations to electromagnetic fields on both sides of the flat interface separating metal and dielectric.

Both electric and magnetic fields are assumed to have a harmonic time dependence, with complex amplitudes $\boldsymbol{\mathcal{E}}(\mathbf{r},\omega)$ and $\boldsymbol{\mathcal{H}}(\mathbf{r},\omega)$ respectively. We can represent these fields as,

$$\mathbf{E}_j(\mathbf{r},t) = \boldsymbol{\mathcal{E}}_j(\mathbf{r},\omega)e^{-i\omega t}, \quad \mathbf{H}_j(\mathbf{r},t) = \boldsymbol{\mathcal{H}}_j(\mathbf{r},\omega)e^{-i\omega t}. \tag{2.1}$$

Figure 2.1: Schematic showing interface between two semi-infinite media.

With Maxwell's equations being transformed such that

$$\nabla \times \mathbf{E}_j = -\mu_o \frac{\partial \mathbf{H}_j}{\partial t} \quad \Rightarrow \quad \nabla \times \boldsymbol{\mathcal{E}}_j = i\mu_o \omega \boldsymbol{\mathcal{H}}_j, \tag{2.2}$$

$$\nabla \times \mathbf{H}_j = \varepsilon_j \varepsilon_0 \frac{\partial \mathbf{E}_j}{\partial t} \quad \Rightarrow \quad \nabla \times \boldsymbol{\mathcal{H}}_j = -i\varepsilon_j \varepsilon_0 \omega \boldsymbol{\mathcal{H}}_j, \tag{2.3}$$

$$\nabla \cdot \mathbf{E}_j = 0 \quad \Rightarrow \quad \nabla \cdot \boldsymbol{\mathcal{E}}_j = 0, \tag{2.4}$$

$$\nabla \cdot \mathbf{H}_j = 0 \quad \Rightarrow \quad \nabla \cdot \boldsymbol{\mathcal{H}}_j = 0. \tag{2.5}$$

Taking the curl of Eq. (2.2), eliminating $\mathbf{H}$ using Eq. (2.3) and applying the divergence equation, Eq. (2.4), for the electric field yields the wave equation in the form

$$\nabla^2 \boldsymbol{\mathcal{E}}_j + \frac{\varepsilon_j \omega^2}{c^2} \boldsymbol{\mathcal{E}}_j = 0. \tag{2.6}$$

We assume plane wave solutions on either side of the interface in the form,

$$\boldsymbol{\mathcal{E}}_j \propto e^{i(k_{xj}x + k_{zj}z)}. \tag{2.7}$$

Boundary solutions require that the lateral components of the wave vectors match on either side of the interface. That is,

$$k_{x1} = k_{x2} = k_x. \tag{2.8}$$

Solving Eq. (2.6) using the proposed wave solution and the boundary conditions gives the dispersion relation

$$k_{xj}^2 + k_{zj}^2 = \frac{\varepsilon_j \omega^2}{c^2}. \tag{2.9}$$

Assuming the wave is TM-polarized, the transversality condition ($\nabla \cdot \boldsymbol{\mathcal{E}}_j = 0$) implies that

$$k_x \mathcal{E}_{xj} + k_{zj} \mathcal{E}_{zj} = 0. \tag{2.10}$$

It follows that

$$\boldsymbol{\mathcal{E}}_j = \mathcal{E}_{xj}(\mathbf{e}_x - \frac{k_x}{k_{zj}}\mathbf{e}_z) e^{i(k_x x + k_{zj} z)}. \tag{2.11}$$

For Maxwell's equations to be satisfied on both sides of the interface, the tangential component of the electric field and the normal component of the flux density on both sides should be matched. This simply means that,

$$\mathcal{E}_{x1} = \mathcal{E}_{x2}, \tag{2.12}$$

and

$$\varepsilon_1 \mathcal{E}_{z1} = \varepsilon_2 \mathcal{E}_{z2}. \tag{2.13}$$

Eq. (2.10), (2.12) and (2.13) form a homogeneous system of four equations for the four unknown field components. This system is solvable when the determinant vanishes. This happens when $k_x = 0$, which is not a desirable solution since there is no travelling surface wave, and also when

$$\varepsilon_1 k_{z2} = \varepsilon_2 k_{z1}. \tag{2.14}$$

The above equation and the dispersion relation Eq. (2.9) imply that,

$$k_x^2 = \frac{\omega^2 \varepsilon_1 \varepsilon_2}{(\varepsilon_1 + \varepsilon_2) c^2}. \tag{2.15}$$

and

$$k_{zj}^2 = \frac{\omega^2 \varepsilon_j^2}{(\varepsilon_1 + \varepsilon_2) c^2}. \tag{2.16}$$

We can only obtain a surface wave between media 1 and 2 (Fig. 2.1) if k_x is real and if k_{zj} are purely imaginary. This means, the wave must propagate along the boundary and decay exponentially in the normal direction. This is possible only when

$$\varepsilon_1\varepsilon_2 < 0, \quad and \quad \varepsilon_1 + \varepsilon_2 < 0. \tag{2.17}$$

This is satisfied when one of the permittivities say, ε_1 is negative with an absolute value greater than that of ε_2 , i.e $\varepsilon_1 < -\varepsilon_2$. This condition is fulfilled for metals ($\varepsilon_1(\omega) < 0$) at frequencies below the bulk plasmon frequency (ω_p). If we introduce the notation $k_{zj} = i\kappa_{zj}$, we can concluded that

$$\kappa_{jz} = \frac{\omega}{c}\sqrt{\frac{\varepsilon_j^2}{|\varepsilon_1+\varepsilon_2|}}, \tag{2.18}$$

and

$$k_x = \frac{\omega}{c}\sqrt{\frac{\varepsilon_1\varepsilon_2}{\varepsilon_1+\varepsilon_2}}. \tag{2.19}$$

The electric field in each medium behaves as

$$\boldsymbol{\mathcal{E}}_j \propto e^{ik_x x}\begin{cases} e^{-\kappa_1 z} & , z \geq 0; \\ e^{\kappa_2 z} & , z \leq 0. \end{cases} \tag{2.20}$$

The surface wave described by Eq. (2.20) is referred to as a surface plasmon polariton. In Eq. (2.19), ε_1 is complex for conductors, thus we can rewrite the complex SPP propagation constant (β_{spp}) as

$$\beta_{spp} = \beta' + i\beta'' = \frac{\omega}{c}\sqrt{\frac{\varepsilon_1\varepsilon_2}{\varepsilon_1+\varepsilon_2}}. \tag{2.21}$$

where β' and β'' denote the real and imaginary parts of the complex propagation constant. β' represents the wave number of the SPP and β'' determines SPP attenuation. Thus a decaying SPP is characterized by the propagation length (L_{spp}), which is defined as the distance in the direction of propagation at which the SPP energy decreases by a factor of $1/e$,

$$L_{spp} = \frac{1}{2\beta''}. \tag{2.22}$$

This damping is caused by ohmic losses of the electrons participating in the SPP propagation. The decay length (L_z) of the SPP electric fields in the direction normal to the interface can be obtained from Eq. (2.18) and is defined as

$$L_z = \frac{1}{k_{zj}}. \tag{2.23}$$

with the $1/e$ decay lengths typically longer in the dielectric compared to the metal.

2.1.2 Surface Plasmon Polariton Dispersion Curves

We now take a closer look at the dispersion relation at a planar metal-dielectric interface, defined in Eq. (2.19). The dispersion relation is plotted for a metal with negligible damping described by the Drude dielectric function in Eq. (2.24) [64] and a dielectric with dielectric constant ε_2.

$$\varepsilon(\omega) = 1 - \frac{\omega_p^2}{\omega^2}, \tag{2.24}$$

where ω_p is the plasma frequency of the metal, given by

$$\omega_p = \sqrt{\frac{ne^2}{m_{eff}\varepsilon_0}}. \tag{2.25}$$

Here n is the carrier density, e is the electronic charge, m_{eff} is the carrier effective mass and ε_0 is the permittivity of free space. The dispersion curve is shown in Fig 2.2, from which we can identify the surface plasmon and bulk plasmon curves which lie on either side of the light line in the dielectric. Bulk plasmons arise from fluctuations of the free charge density inside a metal which propagate as a longitudinally-polarized charge density wave [65]. The region between the bulk and propagating SPP modes is known as the plasmon bandgap.

From Fig 2.2, we observe that the frequency of SPPs approach a characteristic value of ω_{sp} for large wave vectors, where

$$\omega_{sp} = \frac{\omega_p}{\sqrt{1+\varepsilon_2}}. \tag{2.26}$$

This frequency is known as the surface plasmon frequency, at which the electric field behaves like a static field. In the opposite regime of small wave vectors, the dispersion converges to the light line and the SPPs are also known as Sommerfeld-Zenneck waves [66]. We also observe propagation of bound surface modes for $\omega < \omega_{sp}$ and radiation into the metal occurs for frequencies above the plasma frequency.

However, real metals such as gold or silver suffer from inter-band transitions, which leads to increasing damping requiring a Drude dielectric function that accounts for damping,

$$\varepsilon(\omega) = \varepsilon_\infty - \frac{\omega_p^2}{\omega^2 + i\Gamma\omega}, \tag{2.27}$$

where Γ is the collision frequency, and ε_∞ is the static dielectric constant. The Drude model with damping included was used in our studies, with small adjustments made by fitting the

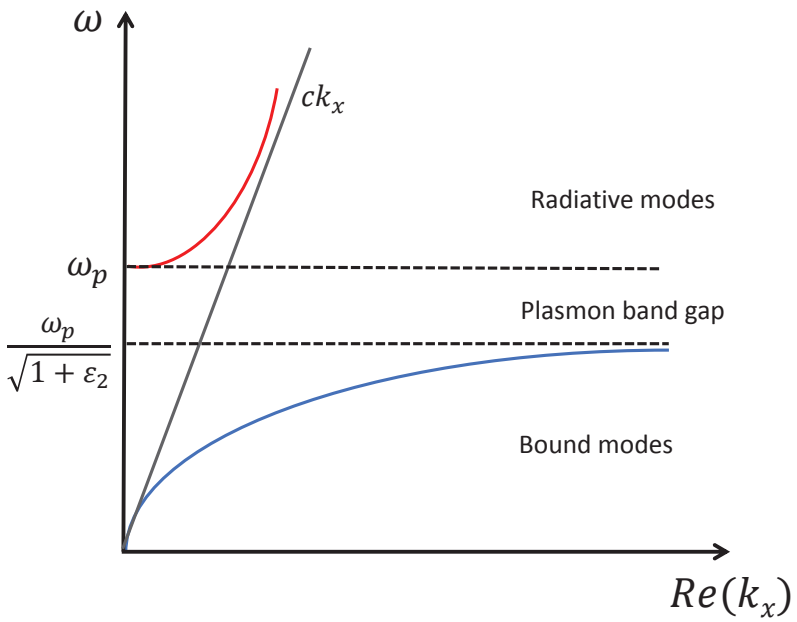

Figure 2.2: Representation of the dispersion curves for bulk plasmon (red line), light in dielectric (black line) and SPP (blue line). The frequencies of the bulk plasmon ω_p and the SPP ω_{sp} are also marked with dashed black lines.

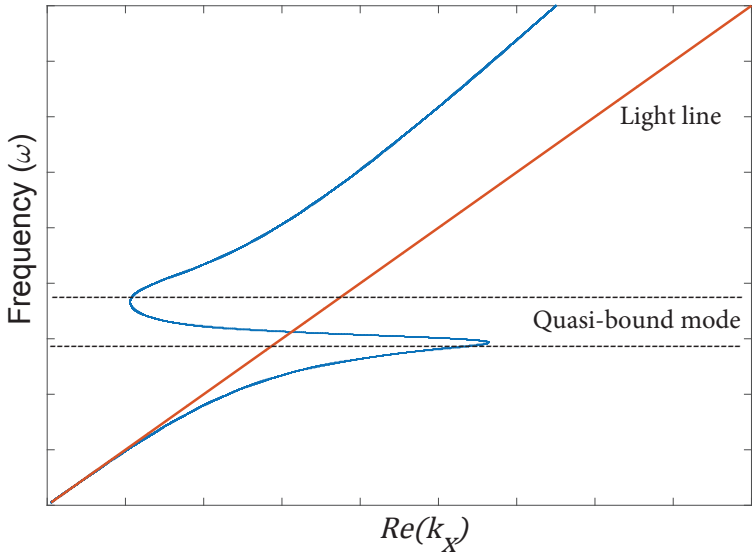

Figure 2.3: Dispersion curve at a gold-air interface using experimental data for ε_{Au} [1].

model to measured permittivity of gold [1, 67]. Fig 2.3 shows the dispersion curve at a gold-air interface, where experimental values of the permittivity of gold are used. Since the metal is no longer modelled as lossless, the wave number of the dispersion curve no longer diverges, but bends backwards filling the region previously called the plasmon bandgap. This region of anomalous dispersion is called a quasi-bound mode [68, 69].

2.1.3 Excitation of SPPs at Planar Interfaces

The dispersion relation defined in Eq. (2.19) is plotted independently for two different dielectrics (ε_2), air and glass(prism). The metal is assumed to be a simple Drude metal with negligible damping.

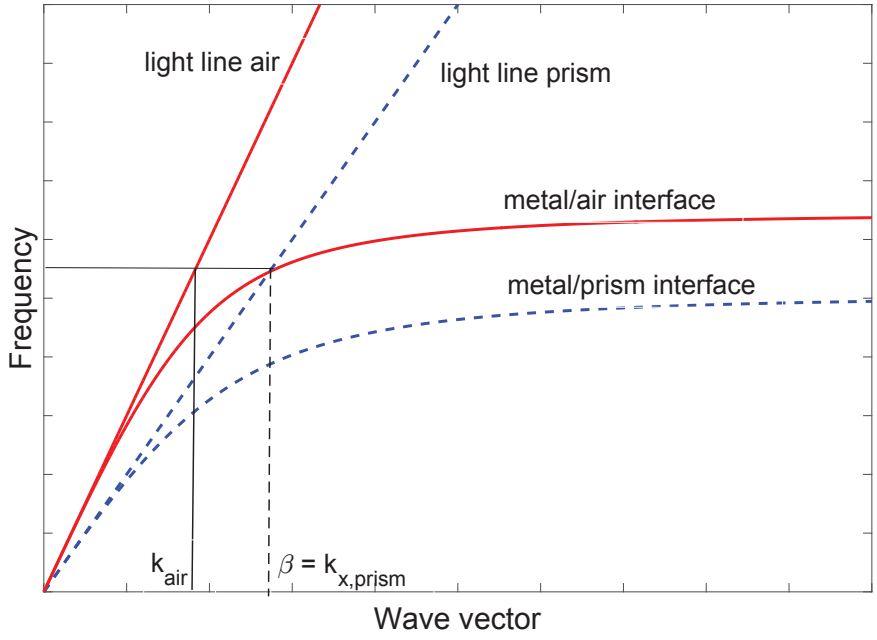

Figure 2.4: Dispersion relation of SPPs at the interface between a Drude metal with negligible damping and air/prism.

Fig 2.4 shows both the SPP dispersion and light line curves for both independent boundaries. For the metal-air boundary, the SPP mode lies on the right side of the light line in air. This means that for a given frequency the wave number in air is always less than the propagation constant of the corresponding SPP mode. Thus SPPs on a flat metal-air interface cannot be directly excited by light in air, due to the wave number mismatch. Special phase-matching techniques are therefore needed to excite SPP modes. Phase-matching can be

achieved by using a three-layer system consisting of a thin metal film sandwiched between two dielectrics of different dielectric constants. This system shown in Fig 2.5 was proposed by Kretschmann [16], and is commonly known as the Kretschmann configuration.

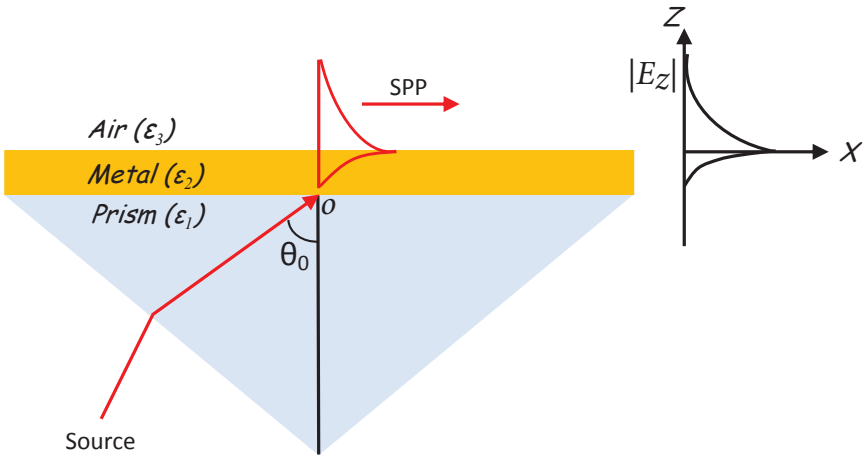

Figure 2.5: Prism coupling using the Kretschmann configuration.

We therefore use the configuration in Fig 2.5 to excite SPPs at the metal-air interface. The incident light with wave vector magnitude k in air, will have a wave vector component $\beta = k_x = k\sqrt{\varepsilon_1} sin\theta_0$ at the interface between the metal and the prism having propagated through the prism. This new wave vector is sufficient to excite SPPs at the interface between the metal and air, due to the higher refractive index of the prism compared to air. Thus we can excite SPP modes with propagation constants β between the light line of air and that of the prism. In this configuration, the incident excitation field has to tunnel through the metal thin film in order to excite SPPs at the metal-air interface. The Kretschmann configuration is used in most SPR applications and is the coupling geometry used for SPP excitation in this research.

Another configuration which is sometimes used is the Otto configuration, where the metal and the prism are separated by a thin layer of air, as illustrated in Fig 2.6. This is preferable for thicker films where the Kretschmann configuration cannot be used and also when contact with the metal surface is undesirable for a specific application . In this configuration, total internal reflection takes place at the prism-air interface, so that photon tunneling occurs through the air gap between the prism and the surface.

Other techniques used for exciting SPPs are; grating coupling, near field excitation, coupling through defects such as nano holes and the focused beam technique. All these

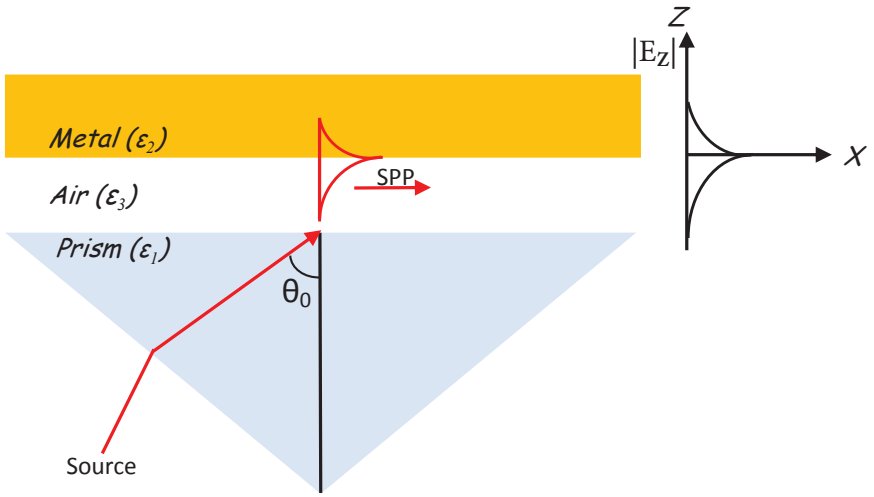

Figure 2.6: Prism coupling using the Otto configuration.

techniques seek to increase the wave vector of the incident light in air to match that of the SP wave.

2.1.4 SPPs at Interface of Thin Metal Films

Our theoretical analysis of SPPs so far has been limited to semi-infinite metal-dielectric interfaces. However, films of finite thicknesses are used in practical SPP-based applications. We expect the multiple reflections within the thin film to affect the SP wave. We use the Kretschmann configuration (Fig 2.5) to analyze the coupling of SPPs in metal films. The conducting film is assumed to have thickness d and the source plane is assumed to be at the origin O. The light source is assumed to be a plane wave such that the incident electric field can be represented as

$$\mathbf{E}_0(x,z,\omega,\theta_0) = \left(\frac{k_{1z}}{k_1}\mathbf{e}_x - \frac{k_x}{k_1}\mathbf{e}_z\right)e^{i(k_x x + k_{1z} z)}, \tag{2.28}$$

where $\mathbf{k}_1 = (k_x, 0, k_{1z})$ and $k_1 = (\omega/c)\sqrt{\varepsilon_1}$, with the components $\mathbf{k}_1$ expressed in terms of the incident angle θ_0 as $k_x = k_1 \sin\theta_0$, and $k_{1z} = k_1 \cos\theta_0$.

Whenever the FW is incident on the metal, it undergoes multiple reflections inside the film and the total reflected FW from the film can be calculated using the Airy summation [70] and is given by

$$\begin{aligned}\mathbf{E}_r(x,z,\omega,\theta_0) =& A(\omega)\Big(-\frac{k_{1z}}{k_1}\mathbf{e}_x - \frac{k_x}{k_1}\mathbf{e}_z\Big) \\ & \times \tilde{r}_{12}(\omega,\theta_0)e^{i(k_x x - k_{1z}z)},\end{aligned} \tag{2.29}$$

where $\tilde{r}_{12}(\omega,\theta_0)$ is the Fresnel reflection coefficient for TM-polarization given by [71]

$$\tilde{r}_{12}(\omega,\theta_0) = \frac{r_{12} + r_{23}e^{i2k_{2z}d}}{1 + r_{12}r_{23}e^{i2k_{2z}d}}, \tag{2.30}$$

with $k_{2z} = \sqrt{k_2^2 - k_x^2}$, $\quad k_2 = (\omega/c)\sqrt{\varepsilon_2}$. Here $r_{\alpha\beta}$ represents a reflection coefficient of the interface between media α and β, $(\alpha,\beta = 1,2,3)$. The total FW field in the glass ($\mathbf{E}_1$) is a superposition of the incident and reflected waves in Eq. (2.28) and Eq. (2.29) respectively and is given by

$$\mathbf{E}_1(x,z,\omega,\theta_0) = \mathbf{E}_0(x,z,\omega,\theta_0) + \mathbf{E}_r(x,z,\omega,\theta_0). \tag{2.31}$$

The normal component of Eq. (2.31) can be written as

$$\mathbf{E}_{1z}(x,z,\omega,\theta_0) = -\frac{k_x}{k_1}e^{ik_x x}\Big[e^{ik_z z} + \tilde{r}_{12}(\omega,\theta_0)e^{-ik_{1z}z}\Big]\mathbf{e}_z, \tag{2.32}$$

while the tangential component is written as,

$$\mathbf{E}_{1x}(x,z,\omega,\theta_0) = \frac{k_{1z}}{k_1}e^{ik_x x}\Big[e^{ik_z z} - \tilde{r}_{12}(\omega,\theta_0)e^{-ik_{1z}z}\Big]\mathbf{e}_x. \tag{2.33}$$

By applying the electromagnetic boundary conditions to both the normal and tangential components of the electric field on both sides of the prism-metal boundary at $z = 0$, we can write down the components of electric field, $E_2^<$ on the lower interface of the metal. The normal component of the field is given by

$$\mathbf{E}_{2z}^<(x,z,\omega,\theta_0) = -\frac{k_x}{k_1}\frac{\varepsilon_1}{\varepsilon_2}e^{ik_x x}\Big[1 + \tilde{r}_{12}(\omega,\theta_0)\Big]\mathbf{e}_z, \tag{2.34}$$

while the tangential component is given by

$$\mathbf{E}_{2x}^<(x,z,\omega,\theta_0) = \frac{k_{1z}}{k_1}e^{ik_x x}\Big[1 - \tilde{r}_{12}(\omega,\theta_0)\Big]\mathbf{e}_x. \tag{2.35}$$

The normal and tangential components of the field in the gold thin film are superpositions of the fields transmitted into the film and that reflected from the upper interface of the thin film. They are given respectively by

$$\begin{aligned}\mathbf{E}_{2z}(x,z,\omega,\theta_0) = &-\frac{k_x}{k_2}e^{ik_x x}\frac{t_{12}}{1+r_{12}r_{23}e^{i2k_{2z}d}} \\ &\times\left[e^{ik_{2z}z}+r_{23}e^{i2k_{2z}d}e^{-ik_{2z}z}\right]\mathbf{e}_z,\end{aligned} \tag{2.36}$$

and

$$\begin{aligned}\mathbf{E}_{2x}(x,z,\omega,\theta_0) = &\frac{k_{2z}}{k_2}e^{ik_x x}\frac{t_{12}}{1+r_{12}r_{23}e^{i2k_{2z}d}} \\ &\times\left[e^{ik_{2z}z}-r_{23}e^{i2k_{2z}d}e^{-ik_{2z}z}\right]\mathbf{e}_x.\end{aligned} \tag{2.37}$$

The components of the electric field at the upper interface of the gold film, $E_2^{>}$ at $z=d$ are calculated similarly to yield

$$\mathbf{E}_{2z}^{>}(x,z,\omega,\theta_0) = -\frac{k_x}{k_2}e^{ik_x x}R_z(\omega,\theta_0)\mathbf{e}_z, \tag{2.38}$$

and

$$\mathbf{E}_{2x}^{>}(x,z,\omega,\theta_0) = -\frac{k_{2z}}{k_2}e^{ik_x x}R_x(\omega,\theta_0)\mathbf{e}_x, \tag{2.39}$$

where

$$\begin{aligned}R_z(\omega,\theta_0) &= \frac{t_{12}(1+r_{23})e^{i2k_z d}}{1+r_{12}r_{23}e^{i2k_{2z}d}}, \\ R_x(\omega,\theta_0) &= \frac{t_{12}(1-r_{23})e^{i2k_z d}}{1+r_{12}r_{23}e^{i2k_{2z}d}}.\end{aligned} \tag{2.40}$$

As mentioned in section 2.1.3, the coupling of light into an SPP wave is characterized by a minimum in the intensity of the light reflected from the metal-dielectric interface. To obtain the dispersion relation for a Kretschmann-based structure, we set the reflectivity given by Eq. (2.30) to zero,

$$r_{12}+r_{23}e^{i2k_{2z}d} = 0. \tag{2.41}$$

where reflection coefficients r_{12} and r_{23} are given by,

$$r_{ij} = \frac{\varepsilon_j k_{iz}-\varepsilon_i k_{jz}}{\varepsilon_j k_{iz}+\varepsilon_i k_{jz}}, \tag{2.42}$$

and the transmission coefficient t_{12} is also given by,

$$t_{ij} = \frac{2\varepsilon_j k_{iz}}{\varepsilon_j k_{iz}+\varepsilon_i k_{jz}}\sqrt{\frac{\varepsilon_i}{\varepsilon_j}}, \tag{2.43}$$

where $i, j = 1, 2, 3$. When the incident light is coupled into an SPP, the normal components of all the wave vectors must be purely imaginary. We can define these wave vectors in media 1 and 3 as

$$k_{1z} = -iq_1 = -i\sqrt{k_x^2 - k_1^2}, \tag{2.44}$$

and

$$k_{3z} = iq_3 = i\sqrt{k_x^2 - k_3^2}, \tag{2.45}$$

with $q_{1,3} > 0$ to ensure the exponential decay of the waves away from the interfaces of the thin film. There exist exponentially growing and decaying waves in the thin film, with its wave vector given by

$$k_{2z} = iq_2 = \pm i\sqrt{k_x^2 - k_2^2}. \tag{2.46}$$

Combining Eqs. (2.41)-(2.46), gives us the desired dispersion equation

$$e^{-2q_2 d} = \left(\frac{\varepsilon_1 q_2 + \varepsilon_2 q_1}{\varepsilon_1 q_2 - \varepsilon_2 q_1}\right)\left(\frac{\varepsilon_3 q_2 + \varepsilon_2 q_3}{\varepsilon_3 q_2 - \varepsilon_2 q_3}\right). \tag{2.47}$$

From Eq. (2.34), Eq. (2.35), Eq. (2.38) and Eq. (2.39), we clearly see that the fields at the metal-dielectric interface in thin films are dependent on the reflection coefficients $\tilde{r}_{12}$, R_z and R_x, which are all functions of the metal film thickness d. The dispersion relation given by Eq. (2.47) is also dependent on the thickness of the conducting film. Thus we can control the SPP field intensity, dispersion, propagation length and energy density by changing the thickness of the film [68].

2.2 SPP Based Sensors

In this section, a general overview of a planar SPR refractive index sensor is presented along with the main performance characteristics of the sensor. A general schematic of such a sensor is shown in Fig 2.7, where ε_3 is the permittivity of the dielectric medium we are interested in sensing.

In an SPR sensor, an SP wave is excited at the interface between a metal film and a dielectric medium (superstrate). Changes in the refractive index of the superstrate affect the coupling condition of the SP waves, which leads to observable changes in one of the characteristics of the optical wave interacting with the SP [72]. By accurately measuring the changes in the given characteristic of the optical wave, we can determine the changes of the refractive index of the dielectric medium. Coupling angle, coupling wavelength,

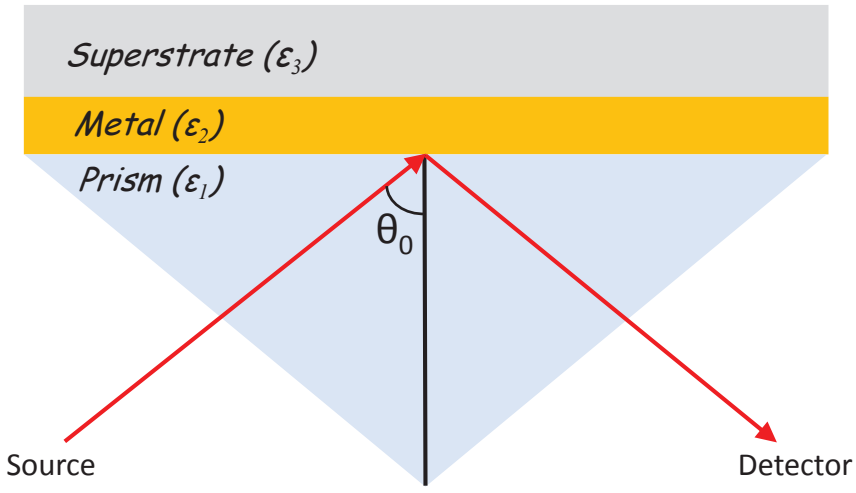

Figure 2.7: Schematics of a planar SPR based sensor.

phase, intensity and polarization are some of the characteristics of the reflected optical wave that change due to changes in the refractive index of the superstrate. Each of these characteristics can used as a sensor output in an SPR sensor. We are going to focus on SPR sensors based on angular and wavelength modulation, since they are the most common modulation approaches used in high performance sensors [73, 74].

In SPR sensors with angular modulation, a monochromatic light wave is used to excite a surface plasmon polariton at the plasmon coupling angle. This is accompanied by a minimum in the intensity of the light wave reflected from the metal-dielectric boundary as illustrated in Fig 2.8 (a). A slight change in the refractive index (Δn) of the superstrate (n_s) would lead to a change in the angle of incidence ($\Delta\theta_0$) at which we observe the reflected light intensity dip from the sensor.

On the other hand, an SPR sensor based on wavelength modulation requires a collimated polychromatic light source. Here, the angle of incidence is kept fixed and the intensity of the light wave reflected from the SPR sensor is dependent on each wavelength component within the polychromatic light source. There is a minimum in the reflected spectrum for a specific wavelength component within the spectrum, where plasmon coupling is maximized as shown in Fig 2.8 (b). Changes in the refractive index of the superstrate would lead to a change in the position of the minimum ($\Delta\lambda_c$) in the reflected spectrum from the SPR sensor.

Our proposed SPR sensor is based on the wavelength modulation of the light wave

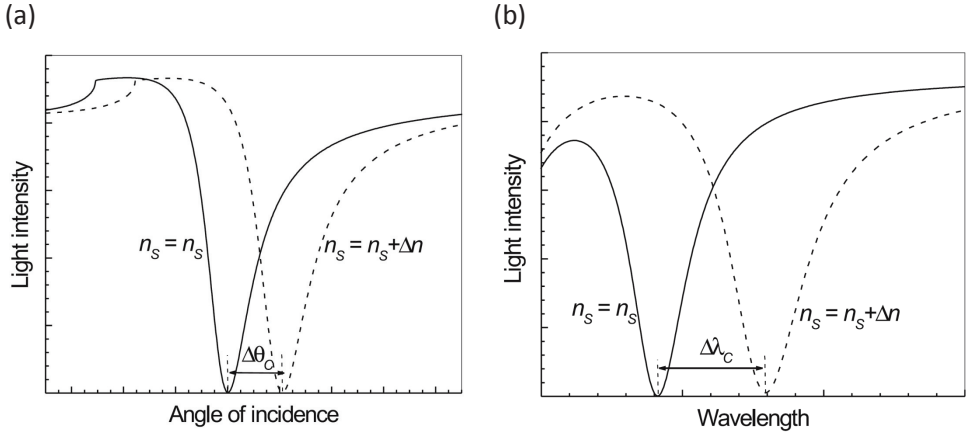

Figure 2.8: Intensity of light wave interacting with a surface plasmon as a function (a) Angle of incidence (b) Wavelength for two different refractive indices of the superstrate [2].

reflected from the sensor. Instead of using the position of the reflected minimum in the spectrum as described above, we use the peak position of the reflected second-order non-linear wave generated at the metal-superstrate interface near plasmon resonance.

The performance characteristics of SPR sensors included in this study are sensitivity and accuracy. The sensitivity is defined as the ratio of the change in the sensor output to the change in the value of the measurand [75]. In the case of the refractive index SPR sensor, the measurand is the change in refractive index of the superstrate, while the sensor output depends on the method of modulation used. Thus we can define the sensitivity of a wavelength modulated refractive index SPR sensor as

$$S(\lambda) = \frac{\Delta\lambda}{\Delta n}, \tag{2.48}$$

where Δn is the change in refractive index of the superstrate (ε_3), and $\Delta\lambda$ is the wavelength shift of SPR peak position of the reflected wave spectrum. The analytical expression for sensitivity with wavelength modulation of a Kretschmann-based refractive index linear SPR sensor is well defined and is given by [76]

$$S(\lambda) = \frac{\varepsilon_2^2(\omega)}{\frac{1}{2}\left|\frac{d\varepsilon_2(\omega)}{d\lambda}\right| n_3^3 + \frac{\varepsilon_2(\omega) n_3}{n_1}\frac{dn_1}{d\lambda}(\varepsilon_2^2(\omega) + n_3^2)}. \tag{2.49}$$

It is manifest From Eq. (2.49) that the sensitivity for a given physical Kretschmann SPR sensor is not constant, but it strongly depends on the wavelength of operation.

When designing SPR sensors, we always aim to optimize the sensitivity. However, the sensitivity enhancement can sometimes be accompanied by spectral broadening. This is not desirable since it limits our detection accuracy. The figure of merit (FOM) offers a convenient parameter to characterize measurement accuracy of the sensor by taking into account both the spectral width and sensitivity of the reflected signal. It is defined as

$$FOM = \frac{S(\lambda)}{FWHM}, \tag{2.50}$$

where FWHM is the full width at half maximum of the reflected spectrum from the SPR sensor. Other important performance indicators for SPR sensors include the limit of detection, dynamic range, reproducibility and linearity.

Chapter 3

Second-Order Surface Nonlinear Optics

In this chapter, we introduce the general concepts of nonlinear optics. We specifically discuss the nonlinear optical effects of SHG, SFG and DFG arising from the second-order nonlinear polarization. We also discuss the second-order susceptibility tensor and, specifically the surface susceptibility tensor in conductors. We then conclude the chapter by presenting a theoretical description of polychromatic sources and the induced nonlinear polarization.

3.1 Introduction to Nonlinear Optics

In the classical electromagnetic theory, the laws of electricity and magnetism are described by Maxwell's equations. In free space, just the electric (**E**) and magnetic (**H**) field vectors are sufficient to describe electromagnetic fields, while the electric displacement (**D**) and magnetic induction (**B**) are all required for a full description of the propagation of electromagnetic radiation in any medium. The complete Maxwell's equations are given by

$$\begin{aligned} \nabla \times \mathbf{E} + \frac{\partial \mathbf{B}}{\partial t} &= 0, \\ \nabla \times \mathbf{H} - \frac{\partial \mathbf{D}}{\partial t} &= \mathbf{J}, \\ \nabla \cdot \mathbf{D} &= \rho, \\ \nabla \cdot \mathbf{B} &= 0, \end{aligned} \tag{3.1}$$

where **J** is the electric current density and ρ is the electric charge density. Whenever an external electric field is applied to matter, it induces dipole moments in atoms or molecules of the matter, resulting in a nonzero average dipole moment per unit volume known as the polarization (**P**). The electric displacement field **D** is related to the electric field **E** through the polarization field **P** in a medium by

$$\mathbf{D} = \varepsilon_0 \mathbf{E} + \mathbf{P}, \tag{3.2}$$

where ε_0 is the permittivity of free space.

When the applied electric field strength is sufficiently low, the polarization vector is linearly related to the incident electric field and given by

$$\mathbf{P} = \varepsilon_0 \chi^{(1)} \mathbf{E}, \tag{3.3}$$

where $\chi^{(1)}$, which is a second rank tensor, is a linear electric susceptibility and it characterizes linear media. However, if the incident electric field is sufficiently large, this approximation of the polarization breaks down and the induced polarization can be expressed as a power series,

$$\begin{aligned} \mathbf{P} &= \mathbf{P}_L + \mathbf{P}_{NL} \\ \mathbf{P} &= \varepsilon_0(\chi^{(1)}\mathbf{E} + \chi^{(2)}\mathbf{E}^2 + \chi^{(3)}\mathbf{E}^3 + ...), \end{aligned} \tag{3.4}$$

where $\mathbf{P}_L = \varepsilon_0 \chi^{(1)} \mathbf{E}$ and $\mathbf{P}_{NL} = \varepsilon_0(\chi^{(2)}\mathbf{E}^2 + \chi^{(3)}\mathbf{E}^3 + ...)$. Here $\mathbf{P}_L$ and $\mathbf{P}_{NL}$ represent the linear and nonlinear contributions to the total polarization, respectively. $\chi^{(2)}$ and $\chi^{(3)}$ represent the second- and third-order nonlinear susceptibility tensors, respectively and they characterize a material response to the incident electromagnetic field.

To study propagation of electromagnetic waves through a nonlinear medium, let us consider a non-magnetic and source free medium ($\mathbf{J} = 0$ and $\rho = 0$). Maxwell's equations (Eq. (3.1)) can be reduced by eliminating $\mathbf{H}$ to obtain the nonlinear wave equation

$$\nabla \times (\nabla \times \mathbf{E}) = -\varepsilon \varepsilon_0 \mu_0 \frac{\partial^2 \mathbf{E}}{\partial t^2} - \mu_0 \frac{\partial^2 \mathbf{P_{NL}}}{\partial t^2}, \tag{3.5}$$

where ε is a relative permittivity of material medium. Further examination of Eq. (3.5) shows that the nonlinear polarization $\mathbf{P}_{NL}$ behaves like a source term in the inhomogeneous wave equation.

3.2 Second-Order Nonlinear Processes

In this section, we briefly discuss the fundamental nonlinear optical processes that result from the second-order nonlinear polarization. Assuming an isotropic medium for simplicity, and without loss of generality, we have ignored the electric field polarization throughout this section.

3.2.1 Second-Harmonic Generation

Let us consider an optical field of amplitude $\mathcal{E}$ at a frequency ω such that

$$E(t) = \mathcal{E}e^{-i\omega t} + c.c. \tag{3.6}$$

When such a field propagates in a medium with a non-vanishing second-order susceptibility, the second-order polarization can be expressed as

$$P^{(2)}(t) = \varepsilon_0 \chi^{(2)} E^2(t). \tag{3.7}$$

Substituting from Eq. (3.6) into Eq. (3.7), we obtain

$$P^{(2)}(t) = 2\varepsilon_0 \chi^{(2)} \mathcal{E}\mathcal{E}^* + (\varepsilon_0 \chi^{(2)} \mathcal{E}^2 e^{-2i\omega t} + c.c). \tag{3.8}$$

Eq. (3.8) shows that the nonlinear polarization contains a component that radiates light at double (2ω) the frequency of the incident light. This component, which is represented in the second term of Eq. (3.8), describes the optical process of SHG. The nonlinear polarization also has a component at zero frequency as illustrated by the first term in Eq. (3.8). This component is known as optical rectification and it represents the generation of a static electric field.

SHG can be described as a coherent absorption of two photons of the same frequency to generate a photon with double the frequency or half the wavelength of the incident wave. This is schematically illustrated in Fig. 3.1.

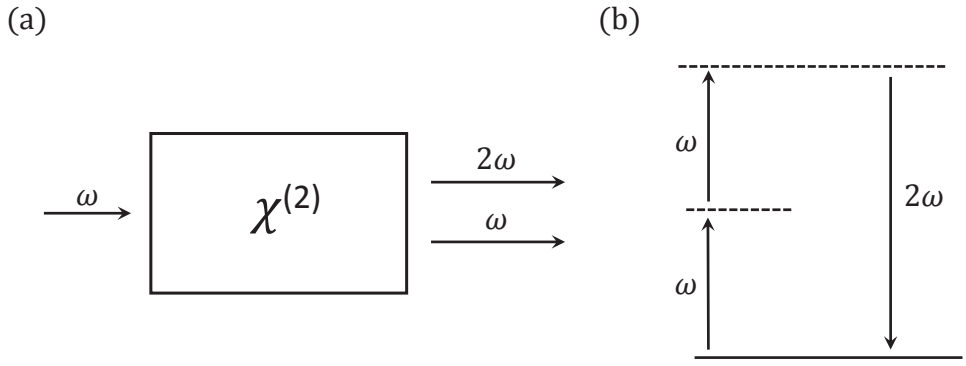

Figure 3.1: (a) Geometry of SHG (b) Energy-level diagram describing SHG [3].

The theoretical formulation of SHG can be broken down into two steps. In the first step, the incident electric field at frequency ω excites a nonlinear polarization at double

the frequency as shown in Eq. (3.8). In the second step, this induced nonlinear polarization propagates in accord with the nonlinear wave equation and emits an optical field at frequency 2ω.

3.2.2 Sum- and Difference-Frequency Generation

Next, we consider an optical field with two distinct frequency components ω_1 and ω_2 propagating in a medium characterized by a second-order nonlinear susceptibility. Such an optical field can be represented as

$$E(t) = \mathcal{E}_1 e^{-i\omega_1 t} + \mathcal{E}_2 e^{-i\omega_2 t} + c.c. \tag{3.9}$$

Substituting this field in Eq. (3.7) yields

$$\begin{aligned} P^{(2)}(t) = \varepsilon_0 \chi^{(2)} [&\mathcal{E}_1^2 e^{-2i\omega_1 t} + \mathcal{E}_2^2 e^{-2i\omega_2 t} + 2\mathcal{E}_1 \mathcal{E}_2 e^{(-i(\omega_1+\omega_2)t)} \\ &+ 2\mathcal{E}_1 \mathcal{E}^*{}_2 e^{(-i(\omega_1-\omega_2)t)} + c.c] + 2\varepsilon_0 \chi^{(2)} [\mathcal{E}_1 \mathcal{E}_1^* + \mathcal{E}_2 \mathcal{E}_2^*]. \end{aligned} \tag{3.10}$$

The nonlinear polarization given in Eq. (3.10) contains new frequency components resulting from different second-order nonlinear optical processes. $2\omega_1, 2\omega_2$ represents the process of second-harmonic generation from the medium, $\omega_1 + \omega_2$ represents the process of sum-frequency generation and $\omega_1 - \omega_2$ represents the process of difference-frequency generation. The last term in the nonlinear polarization expression is the optical rectification term. From Eq. (3.10), we can also extract the complex amplitudes of the SFG and DFG nonlinear polarizations.

The complex amplitude of SFG is given by

$$P_{SFG}(\omega_1 + \omega_2) = 2\varepsilon_0 \chi^{(2)} \mathcal{E}_1 \mathcal{E}_2. \tag{3.11}$$

In the SFG process, the incident photons ω_1 and ω_2 are coherently absorbed to create a new photon at frequency $\omega_3 = \omega_1 + \omega_2$. This is represented schematically in Fig 3.2.

Finally, the process of DFG is described by a complex nonlinear polarization amplitude in the form

$$P_{DFG}(\omega_1 - \omega_2) = 2\varepsilon_0 \chi^{(2)} \mathcal{E}_1 \mathcal{E}_2^*. \tag{3.12}$$

A very important difference between the DFG process compared to the SHG and SFG process is illustrated in Fig 3.3. In the DFG process, for every photon that is created at the

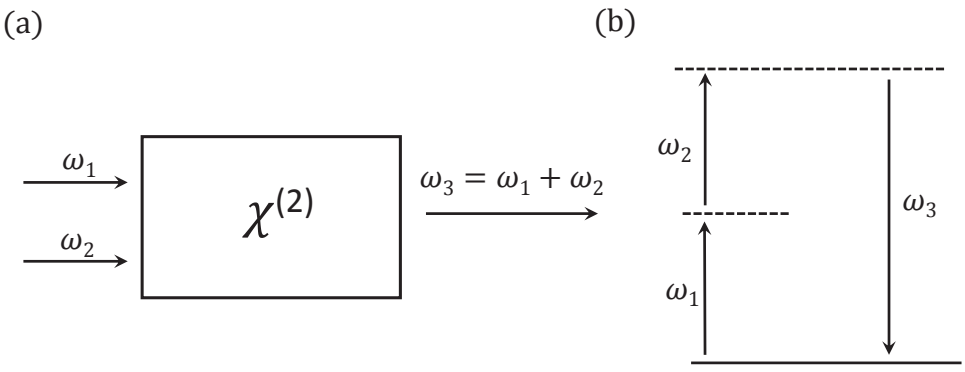

Figure 3.2: (a) Geometry of SFG (b) Energy-level diagram describing SFG [3].

difference frequency $\omega_3 = \omega_1 - \omega_2$, a photon at the higher frequency ω_1 must be destroyed and a photon at the lower frequency ω_2 must be created. Thus we have a situation where the lower frequency input field is being amplified and this is referred to as optical parametric amplification.

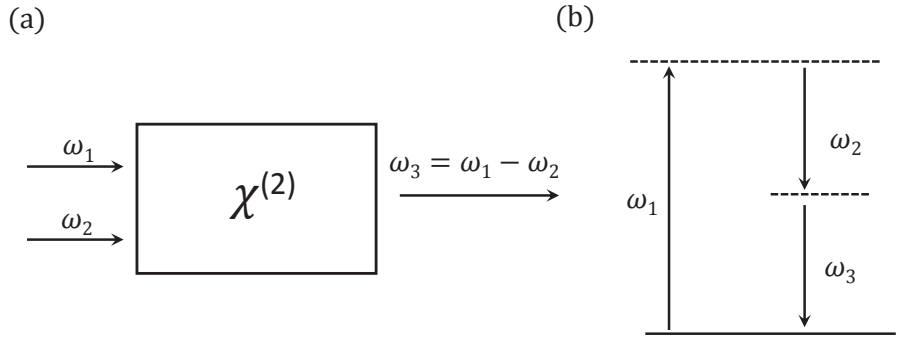

Figure 3.3: (a) Geometry of DFG (b) Energy-level diagram describing DFG [3].

3.3 Nonlinear Second-Order Surface Susceptibility

In this section we briefly discuss some of the properties of the general second-order susceptibility, a microscopic model of the surface second-order susceptibility and conclude with a brief discussion of the nonlinear polarization arising from a polychromatic incident light source.

Let us consider the interaction of three waves of frequencies ω_1, ω_2 and $\omega_3 = \omega_1 + \omega_2$ in a general second-order process. The nonlinear polarization from these interactions,

which can be expressed via the third-rank susceptibility tensor [3],

$$P_i(\omega_n+\omega_m)=\varepsilon_0\sum_{jk}\sum_{(nm)}\chi^{(2)}_{ijk}\mathcal{E}_j(\omega_n)\mathcal{E}_k(\omega_m), \tag{3.13}$$

where $n,m=1,2,3$ and i,j and k can independently take on the values of the Cartesian directions x,y and z, with both positive and negative frequencies allowed. We therefore require as much as 324 different numbers to fully define the complex second-order nonlinear susceptibility. However, because the reality of the physical fields and intrinsic permutation symmetry of $\chi^{(2)}$, we end up with 81 independent parameters. The number of independent parameters can be further reduced in a lossless medium, where all elements of $\chi^{(2)}$ are real and also where Kleinman's symmetry is valid. Any spatial symmetry in a nonlinear material can lead to a further reduction of this number.

One type of spatial symmetry of interest found in some crystals is centrosymmetry. Centrosymmetric crystals have a centre of symmetry, which is a point relative to which the crystal structure displays inversion symmetry. It has been demonstrated using symmetry arguments that the second-order nonlinear susceptibility vanishes under electric dipole approximation in bulk centrosymmetric crystals [77, 78]. Most face-centered cubic (FCC) metals have a centrosymmetric bulk crystal structure including gold [79], which is used in the studies in this dissertation. Thus bulk second-order nonlinear optical processes such as SHG, SFG and DFG are forbidden in such materials.

However, the inversion symmetry is broken at the surface of centrosymmetric crystals due to excitement of surface dipoles. These surface dipoles are responsible for second-order effects, characterized by a surface susceptibility $\chi^{(2)}_{S,ijk}$ which is also a third rank tensor. The bulk second-order effects from centrosymmetric crystals are not strictly zero, as $\chi^{(2)}$ can arise from electric-quadrupole and magnetic-dipole contributions [80, 81]. However, it has been shown experimentally that for most free-electron metals the surface contribution to the second-order nonlinearity completely dominates the bulk contribution [82]. Since gold, whose properties can be described by the free electron model, is the metal of choice in our studies, we have neglected all bulk contributions to the second-order processes investigated.

The i^{th} component ($i=x,y$ or x) of the second-order surface polarization field is given by

$$P^S_i(\omega_3)=\varepsilon_0\sum_{jk}\chi^{(2)}_{S,ijk}E_j(\omega_1)E_k(\omega_2), \tag{3.14}$$

where $\omega_3 = \omega_1 \pm \omega_2$.

In Cartesian coordinates, $\chi^{(2)}_{S,ijk}$ has 27 tensor elements, many of which may vanish or depend on others due to the structural symmetry of the surface. For an isotropic surface, with the z-direction normal to the surface, $\chi^{(2)}_{S,ijk}$ has only four independent nonvanishing elements: $\chi^{(2)}_{S,xxz} = \chi^{(2)}_{S,yyz}, \chi^{(2)}_{S,xzx} = \chi^{(2)}_{S,yzy}, \chi^{(2)}_{S,zxx} = \chi^{(2)}_{S,zyy}$ and $\chi^{(2)}_{S,zzz}$ [81]. These nonvanishing components are usually deduced by carrying out second-order measurements (SHG, SFG and DFG) on the sample using different combinations of input and output beam polarizations.

Despite the best efforts of researchers to estimate the different components of $\chi^{(2)}_{S,ijk}$, there is still a significant lack of experimental data available for the surface susceptibility of metals for different frequencies. Over the years, impressive catalogues of experimental data on the linear optical properties of most metals over wide frequency ranges have been put together [83,84]. Very robust models such as the Drude-Lorentz model describing these optical properties have also been developed. To take advantage of this data, researchers have been working on simple models to calculate $\chi^{(2)}_{S,ijk}$ components of conductors in terms of their linear optical properties such as permittivity.

The first theoretical model for nonlinear optics in metals analyzed the second-order response of conduction electrons using a Boltzmann-equation approach [85], but this model could not explain the experimental results obtained for metals such as Ag, Cu, Au and Au-Ag alloys [86, 87]. The first estimation of the surface second-order susceptibility was phenomenologically presented in 1971 by Rudnick and Stern [88]. They introduced two phenomenological parameters a and b which characterized the second-harmonic response from a metal surface. This phenomenological analysis was extended by Sipe et al. [89] where they studied the possibility of separating surface and bulk contributions using symmetry arguments, but they did not attempt the actual calculations of the susceptibility.

The hydrodynamic (HD) model has been used to estimate different components of the second-order susceptibility. In this model, a conductor is assumed to consist of a semi-infinite isotropic electron gas with an equilibrium density profile that interpolates smoothly between its vacuum and bulk asymptotic values. Initial calculations of the surface nonlinear response using this model was done by Corvi and Schaich [90, 91] and subsequently extended to microscopic calculations and estimation of $\chi^{(2)}_S$ components for simple and noble metals [92–96]. We present a simple one-dimensional model for calculating the $\chi^{(2)}_{S,zzz}$

component of the SFG surface susceptibility of a metal in section 3.3.1. This can be easily extended to calculate the other non-vanishing components of $\chi_S^{(2)}$.

3.3.1 Hydrodynamic Model

The treatment of the hydrodynamic model presented in this section is based on the model developed by Maytorena et al. [95–97]. For simplicity, we present a simple 1-D derivation by assuming a linearly polarized propagating electric field, and this can be easily expanded to a 3-D treatment. Let us consider a metal modeled as a semi-infinite electron gas of charge $-e$, mass m, relaxation time τ, density $n(z,t)$ and velocity field $u(z,t)\mathbf{e}_z$ in the presence of an electric field $E(z,t)\mathbf{e}_z$ where the $z-$direction is normal to the metal surface. The continuity and Euler's hydrodynamic equation for such a system are given by [96]

$$\frac{\partial n}{\partial t}+\frac{\partial (nu)}{\partial z}=0, \tag{3.15}$$

and

$$mn\frac{\partial u}{\partial t}+\frac{mnu}{\tau}+mnu\frac{\partial u}{\partial z}=-enE-\frac{\partial p(n)}{\partial z}, \tag{3.16}$$

respectively. The consecutive terms in Eq. (3.16) correspond to the inertia forces, dissipation through friction, convective momentum flow, electric force and a pressure gradient. The pressure p is calculated from the density dependence of the average energy of a fermion within a noninteracting homogeneous Fermi gas,

$$U/N=(9/10)\gamma n^{2/3}, \tag{3.17}$$

where $\gamma=(3\pi^2)^{2/3}\hbar^2/(3m)$. Assuming local equilibrium, the pressure is given by

$$p(n)=n^2\frac{\partial (U/N)}{\partial n}=\frac{3}{5}\gamma n^{5/3}(z,t), \tag{3.18}$$

as in the Thomas-Fermi theory [90, 98].

The system is perturbed with a homogeneous external electric flux density,

$$\mathbf{D}=(D_1e^{-i\omega_1 t}+D_2e^{-i\omega_2 t})\mathbf{e}_z+c.c, \tag{3.19}$$

that oscillates at the two frequencies ω_1 and ω_2, with electric displacement amplitudes D_1 and D_2, respectively. All time-dependent quantities f are expressed as a superposition of

monochromatic fields with frequencies ω_1, ω_2, $2\omega_1$, $2\omega_2$, and $\omega_1 \pm \omega_2$ to obtain

$$\begin{aligned} f(z,t) =& f_0(z) + f(z,\omega_1)e^{-i\omega_1 t} + f(z,\omega_2)e^{-i\omega_2 t} + f(z,2\omega_1)e^{-i2\omega_1 t} + f(z,2\omega_2)e^{-i2\omega_2 t} \\ &+ f(z,\omega_1+\omega_2)e^{-i(\omega_1+\omega_2)t} + f(z,\omega_1-\omega_2)e^{-i(\omega_1-\omega_2)t} + ... + c.c., \end{aligned} \tag{3.20}$$

where f stands for either n, u or E, and c.c denotes the complex conjugate of the previous terms.

Substituting from Eq. (3.20) into Eq. (3.16), we generate a series of equations for the f variables that oscillate at the same frequency.

To the zeroth-order, Eq. (3.16) yields,

$$-en_0(z)E_0(z) = \frac{\partial p_0(z)}{\partial z} = m\beta_0^2(z)\frac{\partial n_0(z)}{\partial z}, \tag{3.21}$$

where $\beta_0^2(z) = \frac{\gamma}{m}n_0^{2/3}(z)$. $E_0(z)$ plays the role of the effective field which confines the electron gas to a semispace, acting against the pressure term $\frac{3}{5}\gamma m^{5/3}(z)$ leading to the equilibrium density profile $n_0(z)$.

Expanding Eqs. (3.15) and (3.16) to the first-order, and substituting Eq. (3.21), we obtain a differential equation for the first-order polarizations P_i $(i = 1,2)$,

$$\frac{\gamma}{m}n_0(z)\frac{\partial[n_0^{-1/3}\frac{\partial P_i}{\partial z}]}{\partial z} + \beta_0^2(z)q_i^2(z)P_i = S_i(z), \tag{3.22}$$

with the source term

$$S_i(z) = -\omega_p^2(z)D, \tag{3.23}$$

where $\omega_p^2(z) = \omega_b^2 n_0(z)/n_b$ is the local plasma frequency, $\omega_b^2 = n_b e^2/(\varepsilon_0 m_{eff})$ is the bulk plasmon frequency, $\Omega_i^2 = \omega_i(\omega_i + i/\tau)$ and

$$q_i^2(z) = \frac{\Omega_i^2 - \omega_p^2(z)}{\beta_0^2(z)} \tag{3.24}$$

is a local plasmon wave number at the fundamental frequency. In the derivation of Eq. (3.22), we employed the relation between the electric current density J and polarization P, namely

$$J = \varepsilon_0\frac{\partial P}{\partial t}, \tag{3.25}$$

and the self-consistent field E in term of the polarization field P,

$$\varepsilon_0 E_i(z) = D_i - P_i(z). \tag{3.26}$$

Using the similar procedure, the equations for the SFG polarization P_3 are derived at the frequency $\omega_3 = \omega_1 + \omega_2$,

$$\frac{\gamma}{m} n_0(z) \frac{\partial [n_0^{-1/3} \frac{\partial P_3(z)}{z}]}{\partial z} + [\Omega_3^2 - \omega_p^2(z)] P_3(z) = S_3(z), \tag{3.27}$$

with the source term expressed as

$$\begin{aligned} S_3(z) =& \frac{\gamma}{3me} n_0 \frac{\partial [n_0^{-4/3} (\frac{\partial P_1}{\partial z})(\frac{\partial P_2}{\partial z})]}{\partial z} + \frac{\omega_1 \omega_2}{e n_0} \frac{\partial (P_1 P_2)}{\partial z} \\ &+ \frac{(\omega_1 + \omega_2 + i/\tau)}{e n_0} \left(\omega_2 P_2 \frac{\partial P_1}{\partial z} + \omega_1 P_1 \frac{\partial P_2}{\partial z} \right) - \frac{2\omega_1 \omega_2}{e n_0^2} P_1 P_2 \frac{\partial n_0}{\partial z}. \end{aligned} \tag{3.28}$$

The source $S_3(z)$ arises from the spatial derivatives of the equilibrium density n_0 and from the product of the linear polarization at the fundamental frequencies. The differential equations (3.22) and (3.27) are solved analytically in the bulk region where n_0 is independent of z. The linear polarization solution is expressed as,

$$P_i(z) = P_{ib} + A_i e^{i q_i z}, \quad i = 1, 2, \tag{3.29}$$

and the second-order solution expressed as,

$$\begin{aligned} P_3(z) =& \frac{A_3 e^{i q_3 z}}{\sqrt{4\pi\varepsilon_0}} + \frac{i}{e n_b \beta_b^2 \sqrt{4\pi\varepsilon_0}} \left[\frac{\mu_1 q_1 + \mu_2 q_2}{q_3^2 - (q_1 + q_2)^2} A_1 A_2 e^{i(q_1 + q_2) z} \right. \\ &\left. - \left(\frac{\nu_1 q_1 P_{2b}}{4\pi (q_3^2 - q_1^2)} A_1 e^{i q_1 z} + \frac{\nu_2 q_2 P_{1b}}{4\pi (q_3^2 - q_2^2)} A_2 e^{i q_2 z} \right) \right], \end{aligned} \tag{3.30}$$

and it can be integrated numerically near the surface, where $n_0(z)$ varies from zero in vacuum to its bulk value n_b. Here, $\beta_b^2 = (\gamma/m) n_b^{2/3}$, $\nu_i = -(\omega_3 - \omega_i)(\omega_i + \omega_3 + i/\tau)$, $\mu_i = \frac{1}{3}[2(\omega_3 - \omega_i)(\omega_3 - \omega_i + i/\tau) + 6\omega_1\omega_2 + \omega_b^2]$, $P_{ib} = (\varepsilon_i - 1) D_i / \varepsilon_i$ is the bulk polarization linearly induced by D_i in a local medium with a Drude dielectric response $\varepsilon_i \equiv \varepsilon(\omega_i) = 1 - \omega_b^2/\Omega_i^2$, and $q_i^2 = (\Omega_i^2 - \omega_b^2)/\beta_b^2$. The coefficients A_1,A_2 and A_3 are determined by matching the bulk and surface solutions at the boundary using additional boundary conditions derived from the polarization differential equations. The linear boundary conditions are the continuity of both P_i and $n_0^{-1/3} \frac{\partial P_i}{\partial z}$. The second-order additional boundary conditions for the sum-frequency field are the continuity of P_3 and $\mathcal{F}$ is determined by the equation

$$\mathcal{F} = (n_0^{-1/3} \frac{\partial P_3}{\partial z}) - \frac{1}{3 e n_0^{2/3}} (n_0^{-1/3} \frac{\partial P_1}{\partial z})(n_0^{-1/3} \frac{\partial P_2}{\partial z}) - \frac{m \omega_1 \omega_2}{e \gamma n_0^2} P_1 P_2. \tag{3.31}$$

After solving Eq. (3.27) to obtain $P_3(z)$ for a given profile $n_0(z)$, the surface nonlinear sum-frequency polarization can be characterized as

$$P_{3z}^S = \int dz P_3(z), \tag{3.32}$$

from which the surface susceptibility component can be deduced as,

$$\chi^2_{S,zzz}(\omega_1,\omega_2) = \varepsilon_0\varepsilon_1\varepsilon_2 P_3(z)/(D_1 D_2). \tag{3.33}$$

The latter can be rewritten in terms of a dimensionless parameter $a(\omega_1,\omega_2)$ as,

$$\chi^2_{S,zzz}(\omega_1,\omega_2) = \frac{a(\omega_1,\omega_2)\sqrt{4\pi\varepsilon_0}}{32\pi^2 n_b e}\frac{(\varepsilon_1-1)}{\varepsilon_1}\frac{(\varepsilon_2-1)}{\varepsilon_2}. \tag{3.34}$$

It has been shown that the dimensionless parameter $a(\omega_1,\omega_2)$ is essentially frequency-independent whenever the two pump frequencies ω_1 and ω_2 lie well below the bulk plasma frequency ω_b for both the SFG and DFG processes [95, 99]. The incident frequencies used in our studies lie well below their bulk frequency of the metal used. We can conveniently extend this derivation to cover DFG susceptibility components by noting that the DFG ($\omega_3 = \omega_1 - \omega_2$) process results can be obtained from the SFG process by the simple replacement $\omega_2 \to -\omega_2$. The only other non-vanishing components of the SFG and DFG surface nonlinear polarization of metals are $\chi^s_{xxz}(\omega_1,\omega_2)$ and $\chi^s_{xzx}(\omega_1,\omega_2)$, expressed as

$$\chi^2_{S,xxz}(\omega_1,\omega_2) = \frac{-\omega_1 b(\omega_1,\omega_2)\sqrt{4\pi\varepsilon_0}(\varepsilon_1-1)(\varepsilon_2-1)}{16\pi^2 n_b e\varepsilon_2\omega_3}, \tag{3.35}$$

and

$$\chi^2_{S,xzx}(\omega_1,\omega_2) = \frac{-\omega_2 b(\omega_2,\omega_1)\sqrt{4\pi\varepsilon_0}(\varepsilon_1-1)(\varepsilon_2-1)}{16\pi^2 n_b e\varepsilon_1\omega_3}, \tag{3.36}$$

in terms of the dimensionless parameters $b(\omega_1,\omega_2)$ and $b(\omega_2,\omega_1)$, which are given by [95]

$$b(\omega_1,\omega_2) = b(\omega_2,\omega_1) = -1. \tag{3.37}$$

The other components of the surface susceptibility are null due to the rotational and in-plane symmetry of the flat surface [99].

3.3.2 Nonlinear Polarization of Polychromatic Sources

Lasers generate light coherently and the high temporal coherence of the process allows them to emit light in a very narrow wavelength spectrum. It is therefore a good approximation to model the spectrum as monochromatic. We use a plane wave approximation to

model such a source, which is a good approximation to the light waves generated by most conventional lasers. A monochromatic plane wave, linearly polarized in the z-direction and propagating in the x-direction with the amplitude A_0 can be represented mathematically as

$$\mathbf{E}(x,t) = \mathbf{e}_z A_0 e^{i(kx-\omega t)}. \tag{3.38}$$

Recent developments in ultrashort laser pulses and ultrafast optics [59] have led to sources with finite bandwidths. Therefore a more realistic representation of such a source will be a polychromatic plane wave model [58, 100, 101]. The electric field of a fully spatially coherent, polychromatic source, linearly polarized in the z-direction and propagating in the x-direction with the spectral amplitude $A(\omega)$ is given by

$$\mathbf{E}(x,\omega) = \mathbf{e}_z A(\omega) e^{i(kx-\omega t)}, \tag{3.39}$$

with the energy spectrum of the polychromatic source defined as

$$S(\omega) \propto |\mathbf{E}(x,\omega)|^2 = |A(\omega)|^2. \tag{3.40}$$

In our treatment of the surface nonlinear polarization so far, we have assumed two independent incident frequencies ω_1 and ω_2, which is the case when we have monochromatic sources. However, we are using a single polychromatic incident source, whose bandwidth consists of frequencies ω_i with a spectral amplitude $A(\omega_i)$ interacting nonlinearly with each other. Thus the general i^{th} component of the sum-frequency polarization field is given by [3]

$$P_i(\mathbf{r},\omega_3) = \varepsilon_0 \sum_{jk} \int_{-\infty}^{\infty} \frac{d\omega_1}{2\pi} \chi^{(2)}_{S,ijk}(-\omega_3;\omega_1,\omega_2) E_j(\mathbf{r},\omega_1) E_k(\mathbf{r},\omega_2), \tag{3.41}$$

and the difference-frequency polarization given by

$$P_i(\mathbf{r},\omega_3) = \varepsilon_0 \sum_{jk} \int_{-\infty}^{\infty} \frac{d\omega_1}{2\pi} \chi^{(2)}_{S,ijk}(-\omega_3;\omega_1,-\omega_2) E_j(\mathbf{r},\omega_1) E^*_k(\mathbf{r},\omega_2). \tag{3.42}$$

Here $(i,j,k = x,y,z)$, ω_1 and ω_2 are the pump frequencies within the incident fundamental pulse bandwidth; $\omega_3 = \omega_1 \pm \omega_2$ represents the generated sum $(+)$ and difference $(-)$ frequencies and the asterisk $(*)$ denotes a complex conjugate. $\chi^{(2)}_{S,ijk}(-\omega_3;\omega_1,\pm\omega_2)$ is the nonlinear surface susceptibility tensor of the SFG and DFG processes respectively.

Chapter 4

Giant Spectral Transformations in Plasmon Enhanced Difference-Frequency Generation with Polychromatic Light

Franklin Che, Sergey A Ponomarenko, and Michael Cada

Published in: Journal of Optics, November 15, 2016, Vol. 18. No. 12, 125503[1]
URL: http://iopscience.iop.org/2040-8986/18/12/125503

4.1 Abstract

We theoretically study the generation of mid-infrared light through difference-frequency excitation using a single dual-wavelength coherent femtosecond laser source. The difference-frequency wave is generated from the surface of a thin gold film in the Kretschmann coupling geometry due to the surface nonlinearity of the film. We show a clear enhancement of the difference-frequency wave around the surface plasmon polariton coupling angle of the incident fundamental wave. We also show an enormous shift and modification of the difference-frequency spectrum near surface plasmon resonance. We discuss the discovered spectral change dependence on the source pulse duration and incidence angle of the fundamental wave. Our findings have an enormous potential for use in difference-frequency surface sensing and spectroscopy applications.

4.2 Introduction

Although the study of nonlinear frequency conversion in metals goes back to the beginning of nonlinear optics [80, 85, 86, 88, 102–104], there has been renewed interest in this field recently. This new interest is due to the recent growth in the field of plasmonics, which studies the localization and enhancement of electromagnetic fields through the collective

[1] Chosen as Journal of Optics "Paper of the Week", November 2016.

oscillation of conduction electrons in metals. The combination of nonlinearity and plasmonic effects has opened up a whole new area of fundamental research where the generation, modification and enhancement of harmonic frequencies can be studied under a variety of conditions and circumstances [19, 21–24, 105].

Nonlinear studies of surface plasmon excitations in metals are focused primarily on quadratic nonlinearities such as second-harmonic generation (SHG), sum-frequency generation (SFG) and difference-frequency generation (DFG). This is due to the simplicity of these processes and the ability to discriminate the bulk response from the surface response using the inversion symmetry of most metals [24, 27, 106]. These quadratic plasmonic nonlinear processes have led to applications in sensing, spectroscopy and the development of new coherent light sources [28, 37–39, 45, 107]. Most nonlinear plasmonic applications such as infrared-visible nonlinear spectroscopy [108] are based on quasi-monochromatic light sources, where two distinct monochromatic sources are needed for both SFG [54] and DFG [55] spectroscopy. DFG, in particular has also been shown to be the most widely used method to generate mid-infrared (MIR) ultra short pulses [56, 57, 109–111], which is a very useful source for sensing many important organic and inorganic molecules. This is because these molecules have strong absorption peaks within this spectral range [112] and the fact that the DFG process is very sensitive to changes in the surfaces being studied at the molecular level [53, 113].

We propose using a highly collimated polychromatic source to generate a difference-frequency wave (DFW), in the mid-infrared through reflection from a thin metal film arranged in the Kretschmann configuration close to the surface plasmon coupling angle. The generation of MIR sources using DFG usually involves frequency mixing of two monochromatic laser sources [56, 57, 109–111]. We are however using a single polychromatic source which eliminates the need for multiple sources and also has the added advantage of generating spectral signatures and enhancing the DFW close to the plasmon resonance angle. The spectral signatures of a surface sum-frequency wave reflected from a thin gold film using polychromatic light have been previously reported [60], with significant spectral shifts in the spectrum shown close to plasmon resonance. We report more pronounced shifts and enhancement in the difference-frequency spectrum close to plasmon resonance.

4.3 Theory

We use the Kretschmann configuration to illuminate the gold thin film as shown in Fig. 4.1. The gold film is deposited on a glass substrate ($\varepsilon_1 = 2.25$) and has a thickness d and a relative permittivity $\varepsilon_2(\omega)$. The permittivity of the dielectric above the thin film is ε_3 and the source plane is assumed to be at the origin.

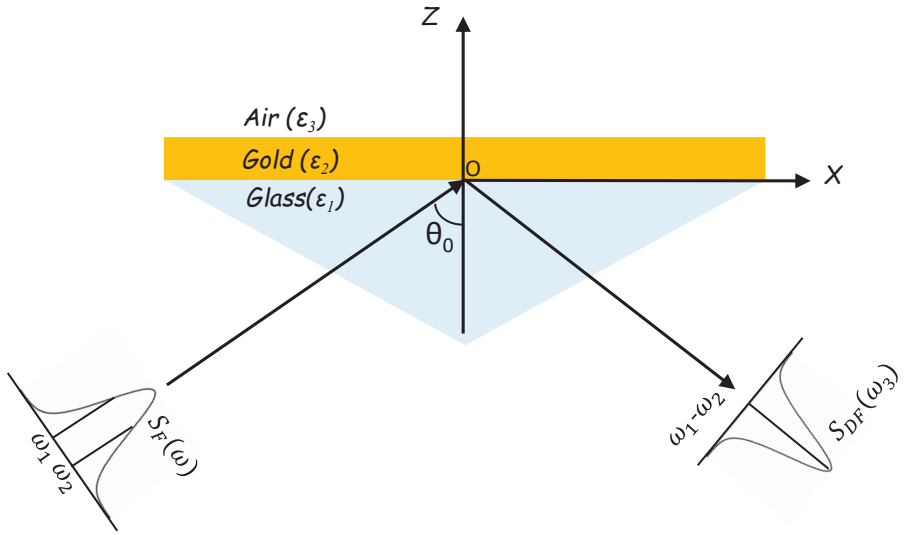

Figure 4.1: Illustration of the Kretschmann configuration.

The light source is assumed to generate a highly collimated and fully spatially coherent plane wave [58, 100, 101]. The incident fundamental wave (FW) with a spectral amplitude $A(\omega)$ is represented by

$$\mathbf{E}_0(x,z,\omega,\theta_0) = A(\omega)\left(\frac{k_{1z}}{k_1}\mathbf{e}_x - \frac{k_x}{k_1}\mathbf{e}_z\right)e^{i(k_x x + k_{1z} z)}, \tag{4.1}$$

where $\mathbf{k}_1 = (k_x, 0, k_{1z})$ and $k_1 = (\omega/c)\sqrt{\varepsilon_1}$, with $\mathbf{k}_1$ expressed in terms of the incident angle θ_0 as $k_x = k_1 \sin\theta_0$ and $k_{1z} = k_1 \cos\theta_0$. The energy spectrum of the incident pulse can be written as [114]

$$S_0(\omega) \propto \left|\mathbf{E}_0(x,z,\omega,\theta_0)\right|^2. \tag{4.2}$$

Whenever the FW is incident on the metal, it undergoes multiple reflections in the thin film and the total reflected FW from the film can be calculated using the Airy summation [70] and is given by

$$\begin{aligned}\mathbf{E}_r(x,z,\omega,\theta_0) =& A(\omega)\Big(-\frac{k_{1z}}{k_1}\mathbf{e_x}-\frac{k_x}{k_1}\mathbf{e_z}\Big)\\ &\times \tilde{r}_{12}(\omega,\theta_0)e^{i(k_x x-k_{1z}z)},\end{aligned} \tag{4.3}$$

where $\tilde{r}_{12}(\omega,\theta_0)$ is the Fresnel reflection coefficient for p-polarization given by [71]

$$\tilde{r}_{12}(\omega,\theta_0)=\frac{r_{12}+r_{23}e^{i2k_{2z}d}}{1+r_{12}r_{23}e^{i2k_{2z}d}}, \tag{4.4}$$

with $k_{2z}=\sqrt{k_2^2-k_x^2}$, $k_2=(\omega/c)\sqrt{\varepsilon_2}$ and $r_{\alpha\beta}$ represents the reflection coefficient of the interface between media α and β, $(\alpha,\beta=1,2,3)$. From Eq. (4.3), the reflected energy spectrum can be written as

$$S_r(\omega,\theta_0)\propto\Big|\mathbf{E}_r(x,z,\omega,\theta_0)\Big|^2. \tag{4.5}$$

The incident wave excites surface polarizations at both the lower and upper interfaces of the gold film. The general i^{th}component of the difference-frequency polarization field is given by [3]

$$\begin{aligned}P_i(\mathbf{r},\omega_3) =& \varepsilon_0\sum_{jk}\int_{-\infty}^{\infty}\frac{d\omega_1}{2\pi}\chi^{(2)}_{S,ijk}(\omega_3;\omega_1,\omega_2)\\ &\times E_j(\mathbf{r},\omega_1)E_k^*(\mathbf{r},\omega_2),\end{aligned} \tag{4.6}$$

where $(i,j,k=x,y,z)$, ω_1 and ω_2 are the pump frequencies within the incident fundamental pulse bandwidth; $\omega_3=\omega_1-\omega_2$ represents the generated difference frequency and the asterisk $(*)$ denotes the complex conjugate. $\chi^{(2)}_{S,ijk}(\omega_3;\omega_1,\omega_2)$ is the nonlinear surface susceptibility tensor of the DFG process. For p-polarized light, the relevant nontrivial contributions to the surface DFG susceptibility are $\chi^{(2)}_{S,zzz}(\omega_3;\omega_1,\omega_2)$, $\chi^{(2)}_{S,xxz}(\omega_3;\omega_1,\omega_2)$ and $\chi^{(2)}_{S,xzx}(\omega_3;\omega_1,\omega_2)$ [115].

We use Eq. (4.6) to evaluate the polarization at the lower ($\mathbf{P}^{<}_{x,z}$) and upper ($\mathbf{P}^{>}_{x,z}$) interfaces of the thin film as we show in A. These lower and upper interface polarizations act as source currents at the difference frequency, and the resulting DFW is given by

$$E_i(\mathbf{r},\omega)=\frac{(\omega/c)^2}{\varepsilon_0}\sum_{jk}\int d\mathbf{r}'G_{ij}(\mathbf{r},\mathbf{r}',\omega)P_j(\mathbf{r}',\omega). \tag{4.7}$$

$G_{ij}(\mathbf{r},\mathbf{r}')$ is the dyadic Green's function given by [27]

$$G_{ij}(\mathbf{r},\mathbf{r}') = \left[\delta_{ij} + \frac{1}{k^2}\nabla_i\nabla_j\right] G_0(\mathbf{r},\mathbf{r}',\omega), \tag{4.8}$$

where G_0 is the scalar Green's function and can be expanded using Weyl's identity [58] to obtain

$$\begin{aligned} G_0(\mathbf{r},\mathbf{r}',\omega) &= \frac{e^{ik|\mathbf{r}-\mathbf{r}'|}}{4\pi|\mathbf{r}-\mathbf{r}'|} \\ &= \frac{i}{8\pi^2}\int_{-\infty}^{\infty}\frac{dk_x}{k_z}e^{ik_x(x-x')+ik_z|z-z'|}, \end{aligned} \tag{4.9}$$

where k_x and k_z represent the longitudinal and transverse components of the propagation vector.

The contribution to the DFW radiated into the lower half-space from the nonlinear polarization at the lower metal interface is obtained by substituting $P^{<}_{x,z}$ into Eq. (4.7), yielding

$$\begin{aligned} \mathbf{E}^{<}_{x,bottom}(x,z,\omega_3,\theta_0) =& \frac{i\omega_3}{4\pi\sqrt{\varepsilon_0\varepsilon_1}}(P^{<}_{0x}\cos\theta_0 - P^{<}_{0z}\sin\theta_0) \\ &\times e^{i(k_x(\omega_3)x - k_{1z}(\omega_3)z)}\mathbf{e}_x, \end{aligned} \tag{4.10}$$

where all quantities are evaluated at the difference frequency ω_3, with
$\mathbf{k}_1(\omega_3) = (k_x(\omega_3), 0, k_{1z}(\omega_3))$ and $\mathbf{k}_2(\omega_3) = (k_x(\omega_3), 0, k_{2z}(\omega_3))$.

$P^{<}_{x,z}$ contributes further to the DFW when the field above(Eq. (4.10)) is partially transmitted through the metal film and reflected from the top metal boundary back into the lower half-space as

$$\begin{aligned} \mathbf{E}^{<}_{x,top}(x,z,\omega_3,\theta_0) =& \frac{i\omega_3}{4\pi\sqrt{\varepsilon_0\varepsilon_1}}(P^{<}_{0x}\cos\theta_0 - P^{<}_{0z}\sin\theta_0) \\ &\times e^{i(k_x(\omega_3)x - k_{1z}(\omega_3)z)}\frac{r_{23}t_{12}e^{i2k_{2z}(\omega_3)d}}{1 + r_{12}r_{23}e^{i2k_{2z,}(\omega_3)d}}\mathbf{e}_x. \end{aligned} \tag{4.11}$$

$t_{\alpha\beta}$ is the transmission coefficient of the interface between media α and β, $(\alpha,\beta = 1,2,3)$. The corresponding z-component of the radiated DFW due to the polarization at the bottom interface of the film is given by

$$\begin{aligned} \mathbf{E}^{<}_{z,bottom}(x,z,\omega_3,\theta_0) =& \frac{i\omega_3}{4\pi\sqrt{\varepsilon_0\varepsilon_1}}(P^{<}_{0z}\sin\theta_0\tan\theta_0 - P^{<}_{0x}\sin\theta_0) \\ &\times e^{i(k_x(\omega_3)x - k_{1z}(\omega_3)z)}\mathbf{e}_z, \end{aligned} \tag{4.12}$$

and after undergoing reflection from the upper interface, it becomes

$$\mathbf{E}^{<}_{z,top}(x,z,\omega_3,\theta_0) = \frac{i\omega_3}{4\pi\sqrt{\varepsilon_0\varepsilon_1}}(P^{<}_{0z}\sin\theta_0\tan\theta_0 - P^{<}_{0x}\sin\theta_0) \times e^{i(k_x(\omega_3)x - k_{1z}(\omega_3)z)}\frac{r_{23}t_{12}e^{i2k_{2z}(\omega_3)d}}{1+r_{12}r_{23}e^{i2k_{2z,}(\omega_3)d}}\mathbf{e}_z. \tag{4.13}$$

The contribution to the difference-frequency field from the polarization $P^{>}_{x,z}$ at the upper metal interface which is radiated into the lower half-space is given by

$$\mathbf{E}^{>}_{x,top}(x,z,\omega_3,\theta_0) = \frac{i\omega_3}{4\pi\sqrt{\varepsilon_0\varepsilon_2(\omega_3)}}(P^{>}_{0x}\cos\theta_0 - P^{>}_{0z}\sin\theta_0) \times e^{i(k_x(\omega_3)x - k_{1z}(\omega_3)z)}\frac{t_{12}e^{i2k_{2z}(\omega_3)d}}{1+r_{12}r_{23}e^{i2k_{2z,}(\omega_3)d}}\mathbf{e}_x, \tag{4.14}$$

and

$$\mathbf{E}^{>}_{z,top}(x,z,\omega_3,\theta_0) = \frac{i\omega_3}{4\pi\sqrt{\varepsilon_0\varepsilon_2(\omega_3)}} \times (P^{>}_{0z}\sin\theta_0\tan\theta_0 - P^{>}_{0x}\sin\theta_0) \times e^{i(k_x(\omega_3)x - k_{1z}(\omega_3)z)}\frac{t_{12}e^{i2k_{2z}(\omega_3)d}}{1+r_{12}r_{23}e^{i2k_{2z}(\omega_3)d}}\mathbf{e}_z, \tag{4.15}$$

where all quantities are evaluated at the difference frequency ω_3.

From Eq. (4.10)-Eq. (4.15), the components of the DFW can be written as

$$\mathbf{E}_x(x,z,\omega_3,\theta_0) = \mathbf{E}^{<}_{x,bottom}(x,z,\omega_3,\theta_0) + \mathbf{E}^{<}_{x,top}(x,z,\omega_3,\theta_0) + \mathbf{E}^{>}_{x,top}(x,z,\omega_3,\theta_0), \tag{4.16}$$

and

$$\mathbf{E}_z(x,z,\omega_3,\theta_0) = \mathbf{E}^{<}_{z,bottom}(x,z,\omega_3,\theta_0) + \mathbf{E}^{<}_{z,top}(x,z,\omega_3,\theta_0) + \mathbf{E}^{>}_{z,top}(x,z,\omega_3,\theta_0). \tag{4.17}$$

The energy spectrum of the DFW can then be conveniently written as

$$\mathbf{S}(\omega_3,\theta_0) \propto \left| E_x(x,z,\omega_3,\theta_0)\mathbf{e}_x + E_z(x,z,\omega_3,\theta_0)\mathbf{e}_z \right|^2. \tag{4.18}$$

4.4 Results

We model a dual-wavelength self-mode-locked Ti:sapphire laser [116], with a pulse duration (t_p) of 50 fs and peaks at $\lambda = 853$ nm ($\omega = 2.208\times10^{15}\ rads/s$) and $\lambda = 767$

nm ($\omega = 2.456 \times 10^{15}\ rads/s$) with the normalized spectral amplitude $A(\omega)$ shown in Fig. 4.2(a). The pulse duration defines the bandwidth of the input Gaussian pulse ($\Delta\omega \approx \frac{0.44}{t_p}$). When this FW is incident on the 50 nm gold thin film, the reflected fundamental wave is evaluated using Eq. (4.5), with the dielectric permittivity of the gold film evaluated by interpolating the experimental values of Johnson and Christy [1]. This reflected field is shown in Fig. 4.2(b).

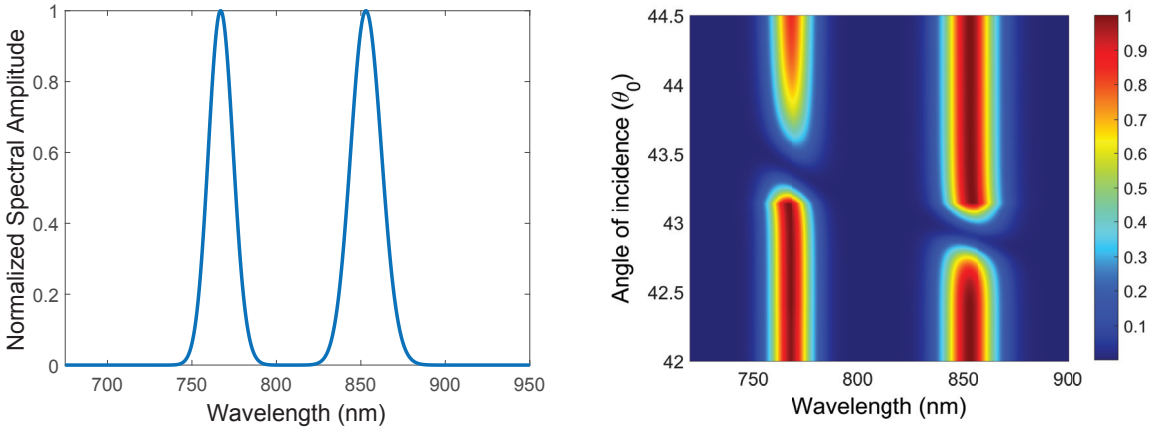

(a) (b)

Figure 4.2: Far-field spectra of (a) incident fundamental wave and (b) the reflected fundamental spectrum from metal film. Incident pulse duration is $t_p = 50fs$.

The holes in the reflected FW spectrum are due to the coupling of the incident wave to surface plasmon polaritons (SPP). The SPP coupling angle for $\varepsilon_3 = 1$(air) is given by [27, 60]

$$\theta_c(\omega) = \arcsin\left[\sqrt{\frac{\varepsilon_2(\omega)}{\varepsilon_1(\varepsilon_2(\omega)+1)}}\right]. \tag{4.19}$$

For $\lambda = 767$ nm and $\lambda = 853$ nm, the corresponding SPP coupling angles, calculated from Eq. (4.19), are 43.3^o and 42.8^o respectively, which coincides well with the plasmon resonance angles in Fig. 4.2(b).

To evaluate the DFW, we use the hydrodynamic model of the difference-frequency surface susceptibility developed in [95]. The nonvanishing susceptibility components are given by

$$\chi^{(2)}_{S,zzz}(\omega_3;\omega_1,\omega_2) = -\frac{a(\omega_1,\omega_2)[\varepsilon_2(\omega_1)-1][\varepsilon_2^*(\omega_2)-1]}{64\pi^2\varepsilon_2(\omega_1)\varepsilon_2^*(\omega_2)n_B e},$$
$$\chi^{(2)}_{S,xzx}(\omega_3;\omega_1,\omega_2) = -\frac{2b(\omega_1,\omega_2)[\varepsilon_2(\omega_1)-1][\varepsilon_2^*(\omega_2)-1]\omega_2}{64\pi^2\omega_3\varepsilon_2(\omega_1)n_B e}, \quad (4.20)$$
$$\chi^{(2)}_{S,xxz}(\omega_3;\omega_1,\omega_2) = -\frac{2b(\omega_1,\omega_2)[\varepsilon_2(\omega_1)-1][\varepsilon_2^*(\omega_2)-1]\omega_1}{64\pi^2\omega_3\varepsilon_2^*(\omega_2)n_B e},$$

where n_B is the equilibrium free-electron density in the bulk. The dimensionless parameters $a(\omega_1,\omega_2)$ and $b(\omega_1,\omega_2)$ are frequency independent when ω_1 and ω_2 are well below the plasma frequency ω_p, which is true in our case ($\frac{\omega_{1,2}}{\omega_p} \approx 0.15$). We use $b(\omega_1,\omega_2) = -1$ and $a(\omega_1,\omega_2) = -12.9$ [115]. To evaluate the DFW we use Eq.(4.18).

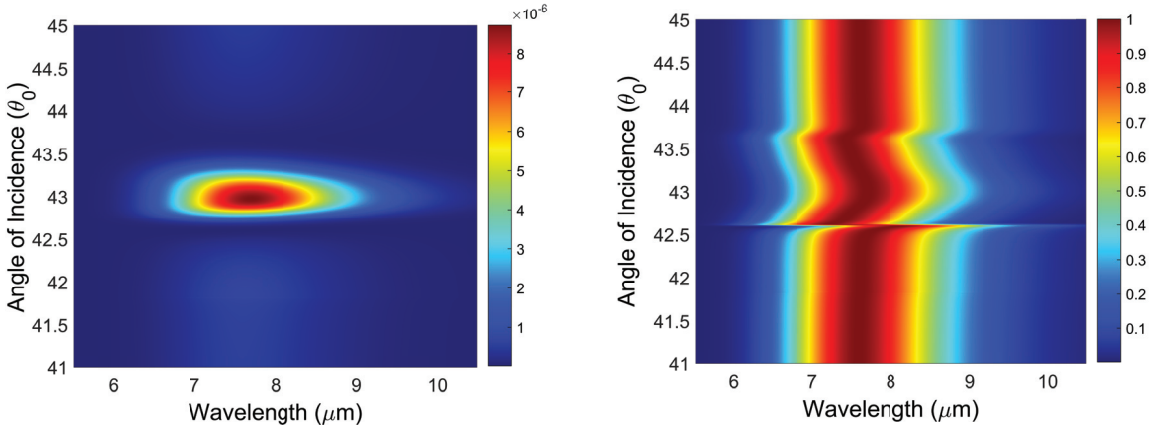

(a) (b)

Figure 4.3: Reflected far-field spectra of (a) DFW (b) Normalized DFW. Incident pulse duration is $t_p = 50fs$.

Fig. 4.3(a) shows the reflected DFW energy spectrum for a 50 fs FW. The DFW peak is centered around 7.70 μm, which corresponds to the frequency difference (ω_3) of the peaks in our fundamental wave, with $\omega_3 = \omega_1 - \omega_2$, where $\omega_1 = 2.456 \times 10^{15}$ $rads/s$, and $\omega_2 = 2.208 \times 10^{15}$ $rads/s$. Fig. 4.3(a) also shows an enhancement of the DFW around the plasmon resonance angles of both peaks in the FW, which is between 42.6^o and 43.5^o, with a maximum enhancement of 14 times the off-resonance spectral amplitude. The enhancement of the DFW is clearly due to the coupling of the FW to surface plasmon polaritons, which has also been reported before in the Kretschmann configuration for SHG [24] and SFG [60].

We can better highlight the spectral effects of DFG in our system by normalizing the DFW spectrum to the corresponding maximum for each angle of incidence [60] as shown in

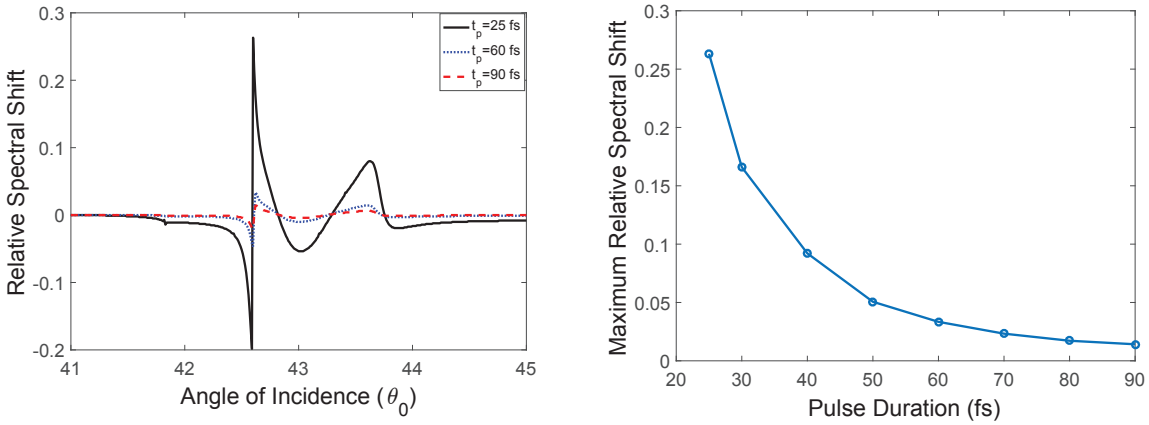

(a) (b)

Figure 4.4: (a) Dependence of relative spectral shifts on pulse duration and angle of incidence (b) Maximum spectral shift as a function of pulse duration.

Fig. 4.3(b). We observe significant shifts in our spectrum between the plasmon resonance angles of 42.6^o and 43.5^o. This shift is more pronounced at the lower edge of the plasmon resonance angular range around 42.6^o. To explore the dependence of these spectral shifts on the pulse duration or angle of incidence, we determine the so-called relative spectral shift $(\frac{\Delta\lambda}{\lambda_0})$ [60], where $\lambda_0 = 7.70\ \mu m$. This dependence is shown in Fig. 4.4(a), where we notice a clear increase in the spectral shift with decreasing pulse duration. Fig. 4.4(b)illustrates this dependency better, showing the maximum spectral shift for pulse durations ranging from 25 fs to 90 fs. A fundamental wave with a short pulse duration has a large bandwidth. This means a wider range of frequencies are coupled into surface plasmons and with each frequency having a slightly different plasmonic and nonlinear response, the total effect on the DFW spectrum is more pronounced.

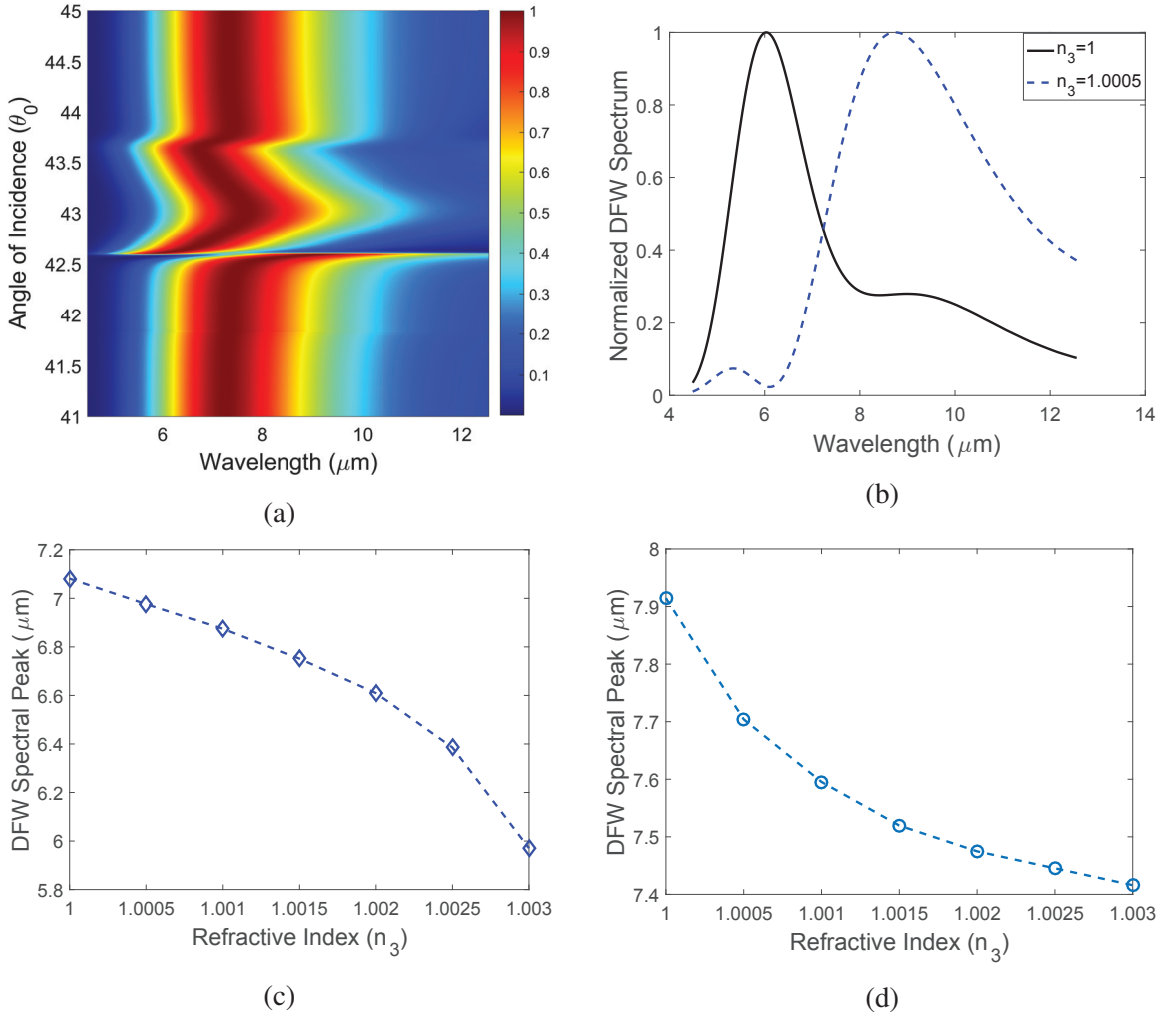

Figure 4.5: (a) Normalized far-field spectra of DFW with a source pulse duration of $t_p = 25fs$ (b) Normalized DFW spectral shift close to plasmon resonance at $\theta_0 = 42.6^o$ for $\Delta n_3 = 5 \times 10^{-4}$ (c) DFW peak dependence on refractive index n_3 at $\theta_0 = 42.8^o$ (d) DFW peak dependence on refractive index n_3 at $\theta_0 = 42.5^o$.

To further examine the spectrum of the DFW, we display the normalized DFW spectra for a $25fs$ FW as shown in Fig. 4.5(a), with the maximum spectral shift seen around $\theta_0 = 42.6^o$. Fig. 4.5(b) shows a colossal spectral shift for a small change in the refractive index of the dielectric material (n_3) with $\Delta n_3 = 5 \times 10^{-4}$, at the angle of incidence corresponding to the maximum shift in Fig. 4.5(a). We also observe significant spectral shifts varying n_3 above and below the maximum angle as shown in Fig. 4.5(c) and Fig. 4.5(d), respectively. Linear and nonlinear spectral shifts close to resonance are both based on the frequency dependence of the plasmonic response of metal thin films, which have frequency-dependent permittivities and nonlinear susceptibilities. The DFW spectral shifts are more pronounced

compared to those engendered by a linear 7.70 μm femtosecond pulse coupled into surface plasmon polaritons in the Kretschmann configuration because of the nonlinear interaction of the plasmon-enhanced FW which generates the DFW. Such sensitivity to small changes in refractive index could be very useful for surface sensing applications.

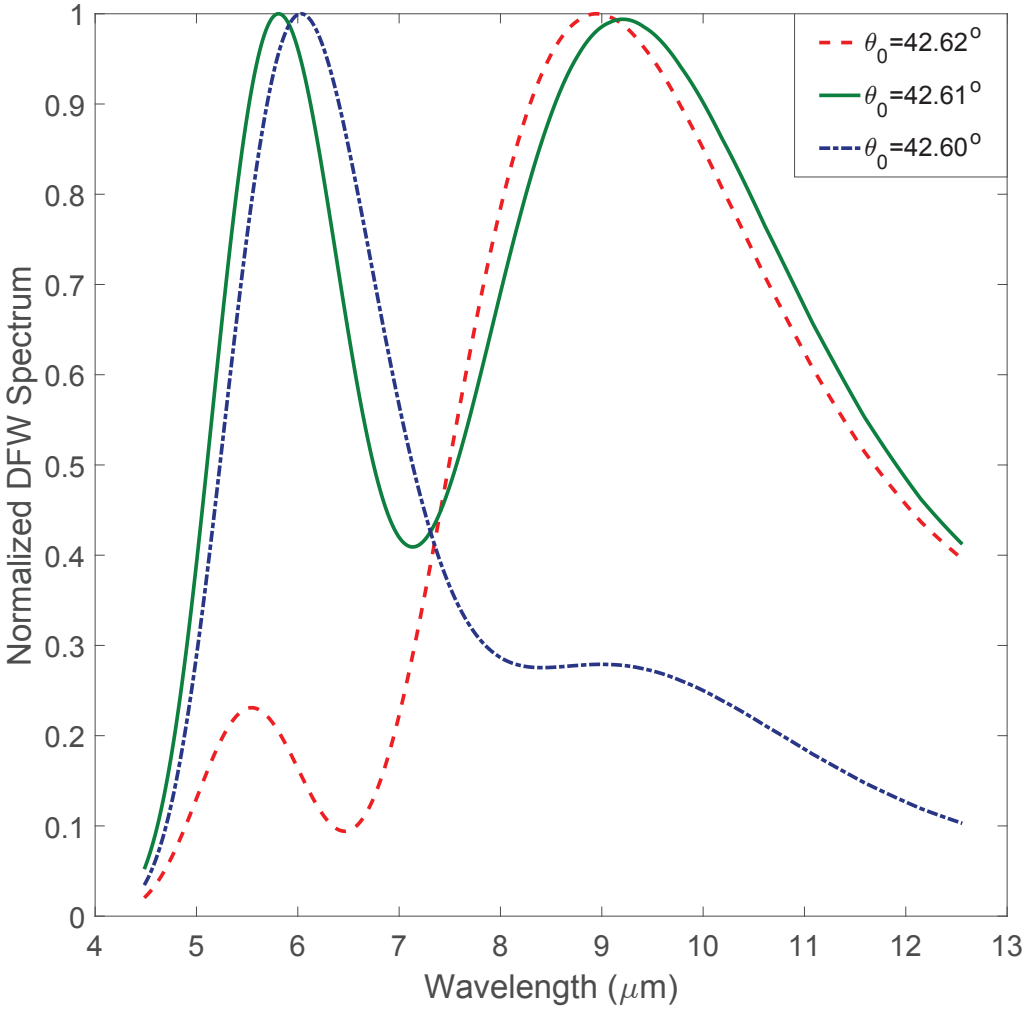

Figure 4.6: Normalized far-field DFW energy spectrum close to resonance showing changes in the spectral shape, $n_3 = 1$ and $t_p = 25 fs$.

Besides the spectral shifts, we also observe changes in the shape of the DFW spectrum close to resonance. We can clearly observe the evolution of the shape of the DFW when we vary the angle of incidence slightly from $\theta_0 = 42.60^o$ to $\theta_0 = 42.62^o$ in Fig. 4.6. Such sensitivity of the spectral shape on small angular variations can also be leveraged for sensing applications.

4.5 Conclusions

We have theoretically investigated the generation of a mid-infrared DFW from a thin gold film in the Kretschmann configuration. We used a single dual wavelength femtosecond laser as our source and gaps were observed in the spectrum of the reflected fundamental wave, which corresponded to the plasmon resonance angles of the individual peaks. The DFW peak amplitude frequency corresponded to the difference between the peak frequencies in our FW, and was clearly enhanced around the plasmon resonance angle of the fundamental wave. We have also shown very large spectral shifts in the DFW close to the surface plasmon resonance angles and also highlighted their dependence on both the pulse duration of the fundamental wave, the angle of incidence and changes in the refractive index of dielectric above the metal film. Lastly, changes in the DFW spectral shape close to resonance were also demonstrated. All these features make our system attractive for use as a MIR source and a sensitive surface sensor.

Chapter 5

High Sensitivity Integrated Visible to Mid-Infrared Nonlinear Plasmonic Sensor

Franklin Che, Sergey A Ponomarenko, Michael Cada and Nghia Nguyen-Huu

Published in: IEEE Photonics Journal, August 15, 2017, Vol. 9. No. 4, 125503

URL: http://ieeexplore.ieee.org/document/7941976/

5.1 Abstract

We propose a Kretschmann-based nonlinear plasmonic sensor with a gold thin film deposited on a glass prism. Visible and mid-infrared signals are generated in this configuration through the nonlinear processes of sum- and difference-frequency generation respectively. The calculated maximum sensitivity and figure of merit of our sum-frequency based sensor are an order of magnitude higher than that of a traditional Kretschmann-based sensor in the visible range. Our difference-frequency based sensor has a maximum sensitivity of 1.0×10^6 nm/RIU in air at 4.29 μm which is three orders of magnitude higher than that of existing devices in the mid-infrared range, with its maximum figure of merit almost two orders of magnitude higher than the alternatives. By comparison, the calculated sensitivity for operation in water for both sum- and difference frequency is about half that in air. We thus demonstrate significant gains in the sensitivity of the well known Kretschmann-based plasmonic sensor over a wide wavelength range, without modifying the physical sensor, but by exploiting and simply taping the nonlinear optical properties of the system.

5.2 Introduction

In the past decade or so we have witnessed rapid development in the field of plasmonics which exploits collective oscillations of conduction electrons in metals [64, 117]. These oscillations are also known as surface plasmon resonance (SPR), with the position and intensity of the SPR strongly affected by the type of conductor and dielectric properties

of the surrounding environment [64, 118]. This has led to the development of a variety of sensors with applications to biochemical and environmental sensing [119–123].

The most common SPR sensor configuration is based on the Kretschmann coupling geometry, whereby a metal thin film is deposited on a glass prism [16] . Changes in the refractive index of the dielectric on the metal film can be matched to either angular or spectral changes in the reflected linear fundamental wave (FW) from the sensor. Despite its simplicity, the Kretschmann-based sensor has limited sensitivity [124], which has led to a move towards other plasmonic sensors such as local surface plasmon (LSP) [125], grating-coupled [126], optical fibre [127] and composite [128] sensors that offer greater sensitivity.

Most of the plasmonic sensors mentioned above work within the framework of linear plasmonics, where there is no frequency mixing within the incident light source spectrum bandwidth. On the other hand, most of the research carried out in the field of nonlinear plasmonics, is geared towards the fundamental understanding of generation, modification and enhancement of harmonic frequencies [26, 129–133]. However, there has been some progress made in the development of nonlinear plasmonic sensors based on the processes of second (SHG) [134, 135] and third harmonic generation [136], with most of these sensors based on LSP resonance of nanoparticles.

We have recently demonstrated [61, 137] plasmon-enhanced spectral changes in reflected sum-frequency generation (SFG) and difference-frequency generation (DFG) using the simple Kretschmann configuration. In the current study, we propose a robust, simple and highly sensitive nonlinear surface plasmon sensor operating at visible and mid-infrared (MIR) wavelengths based on the Kretschmann geometry. We demonstrate ultra high wavelength sensitivities for the proposed sensor compared to that of traditional Kretschmann plasmonic sensors [124, 138], especially at mid-infrared wavelengths, where many metals experience huge losses [139]. We also estimate the signal strength and figure of merit of the proposed sensor.

5.3 Kretschmann Coupling Geometry and Theoretical background

We use the so-called Kretschmann configuration shown in Fig. 5.1 for our proposed sensor. Our sensor is dynamic in the sense that we use the same physical sensor over a wide wavelength range as opposed to the traditional Kretschmann sensor which operates only

at optical frequencies. The conducting film is deposited on a glass prism with permittivity $\varepsilon_1 = 2.25$ and thickness d. We are using gold as the thin film of choice in this investigation due to its inertness and compatibility with biological samples. Other metals can be used for our sensor as well, depending on the sample of interest. Silver in particular has been shown to have a strong plasmonic response at visible frequencies, with very sharp resonance peaks and could be used if inertness and stability are not important for a sample under examination [124].

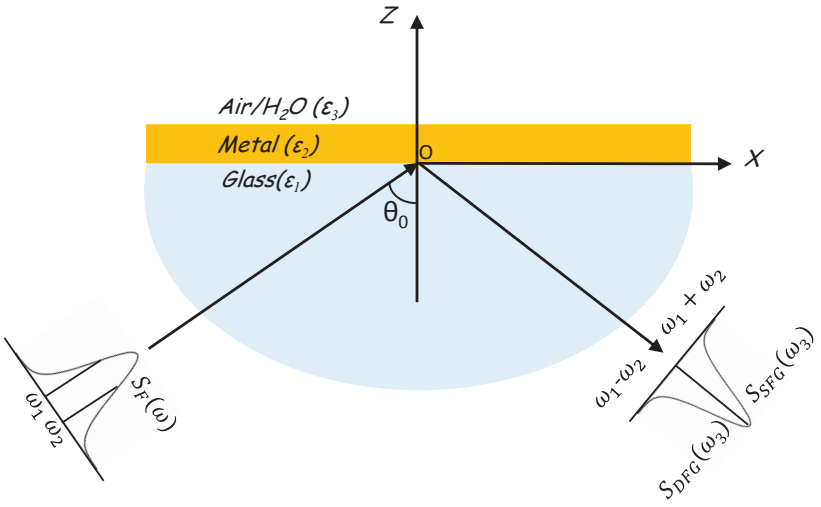

Figure 5.1: Irradiation configuration.

With the physical structure of the sensor fully defined, we then proceed to briefly outline the theory of the linear and nonlinear interaction of light incident on a metal film in this geometry. The light source is assumed to generate a highly collimated and fully spatially coherent plane wave [58, 100, 140]. The incident FW with a spectral amplitude $A(\omega)$ is represented by

$$\mathbf{E}_0(x,z,\omega,\theta_0) = A(\omega)\left(\frac{k_{1z}}{k_1}\mathbf{e}_x - \frac{k_x}{k_1}\mathbf{e}_z\right)e^{i(k_x x + k_{1z} z)}, \tag{5.1}$$

where $\mathbf{k}_1 = (k_x, 0, k_{1z})$ and $k_1 = (\omega/c)\sqrt{\varepsilon_1}$, with $\mathbf{k}_1$ expressed in terms of the incident angle θ_0 as $k_x = k_1 \sin\theta_0$ and $k_{1z} = k_1 \cos\theta_0$.

Whenever the FW is incident on the metal, it undergoes multiple reflections within the thin film. The cumulative reflected FW from the film can be calculated using the Airy summation technique [70] and is given by

$$\begin{aligned}\mathbf{E}_r(x,z,\omega,\theta_0) =& A(\omega)\Big(-\frac{k_{1z}}{k_1}\mathbf{e_x}-\frac{k_x}{k_1}\mathbf{e_z}\Big)\\ &\times \tilde{r}_{12}(\omega,\theta_0)e^{i(k_x x-k_{1z}z)},\end{aligned} \tag{5.2}$$

where $\tilde{r}_{12}(\omega,\theta_0)$ is the Fresnel reflection coefficient for p-polarization given by [71]

$$\tilde{r}_{12}(\omega,\theta_0)=\frac{r_{12}+r_{23}e^{i2k_{2z}d}}{1+r_{12}r_{23}e^{i2k_{2z}d}}, \tag{5.3}$$

with $k_{2z}=\sqrt{k_2^2-k_x^2}$, $k_2=(\omega/c)\sqrt{\varepsilon_2}$; $r_{\alpha\beta}$ represents the reflection coefficient of the interface between media α and β, $(\alpha,\beta=1,2,3)$.

The energy spectrum of the incident $S_0(\omega,\theta_0)$ and reflected $S_r(\omega,\theta_0)$ waves can be written as [114]

$$S_{0,r}(\omega,\theta_0)\propto\Big|\mathbf{E}_{0,r}(\omega,\theta_0)\Big|^2. \tag{5.4}$$

The incident wave excites surface polarizations at both the lower and upper interfaces of the gold film. We use the undepleted pump approximation implying that the power of the incident FW is assumed to be constant. Thus the general i^{th}component of the sum-frequency polarization field is given by [3]

$$\begin{aligned}P_i(\mathbf{r},\omega_3) =& \varepsilon_0\sum_{jk}\int_{-\infty}^{\infty}\frac{d\omega_1}{2\pi}\chi^{(2)}_{S,ijk}(-\omega_3;\omega_1,\omega_2)\\ &\times E_j(\mathbf{r},\omega_1)E_k(\mathbf{r},\omega_2),\end{aligned} \tag{5.5}$$

and the difference-frequency polarization given by

$$\begin{aligned}P_i(\mathbf{r},\omega_3) =& \varepsilon_0\sum_{jk}\int_{-\infty}^{\infty}\frac{d\omega_1}{2\pi}\chi^{(2)}_{S,ijk}(\omega_3;\omega_1,\omega_2)\\ &\times E_j(\mathbf{r},\omega_1)E^*_k(\mathbf{r},\omega_2).\end{aligned} \tag{5.6}$$

Here $(i,j,k=x,y,z)$, ω_1 and ω_2 are the pump frequencies within the incident fundamental pulse bandwidth; $\omega_3=\omega_1\pm\omega_2$ represents the generated sum $(+)$ and difference $(-)$ frequencies and the asterisk $(*)$ denotes a complex conjugate. $\chi^{(2)}_{S,ijk}(\mp\omega_3;\omega_1,\omega_2)$ is the nonlinear surface susceptibility tensor of the SFG and DFG processes respectively.

We use Eq. (5.1),(5.5) and (5.6) to evaluate the nonlinear polarization at the lower and upper interfaces of the film. These lower and upper interface polarizations act as source

currents at the nonlinear frequency, and the resulting sum- or difference-frequency field is given by

$$E_i(\mathbf{r},\omega) = \frac{(\omega/c)^2}{\varepsilon_0}\sum_{jk}\int d\mathbf{r}' G_{ij}(\mathbf{r},\mathbf{r}',\omega)P_j(\mathbf{r}',\omega). \tag{5.7}$$

Here $G_{ij}(\mathbf{r},\mathbf{r}')$ is a dyadic Green's function [27]. The reflected sum-and difference-frequency signal spectra can then be determined from their definitions, Eq. (5.4). We have presented just a general outline of the theoretical formulation with the complete treatment and technical details found in [61,137]. It should be noted that all quantities in Eq. (5.7) are evaluated at either the sum or difference frequency ω_3.

The proposed plasmonic sensor performance is evaluated by its sensitivity, $S(\lambda)$ and figure of merit (FOM). For our sensor, $S(\lambda)$ measures the dependence of the reflected nonlinear resonance peak position on changes in the refractive index of the dielectric environment (ε_3), while the FOM determines the measurement accuracy of the sensor by taking into account the spectral width of the reflected signal. Ideally, we want a sensor with high values of both sensitivity and FOM. The wavelength sensitivity of a plasmonic sensor is defined as [141]

$$S(\lambda) = \frac{\Delta\lambda}{\Delta n}, \tag{5.8}$$

where n is the refractive index of the dielectric sample (ε_3), and λ is the peak wavelength of the reflected wave. By changing the dielectric constant of medium 3, we calculate the resultant shifts in the peak position of the nonlinear reflected spectrum and use this to determine the spectral sensitivity. The FOM is defined as [142]

$$FOM = \frac{S(\lambda)}{FWHM}, \tag{5.9}$$

where FWHM is the full width at half maximum of the reflectance dip (linear sensor) or peak (nonlinear sensor) spectrum. The signal to noise ratio (SNR) is sometimes used to evaluate the performance of a SPR sensor and is defined by [143]

$$SNR = \frac{\Delta\lambda}{FWHM}. \tag{5.10}$$

The FOM provides the same qualitative information as the SNR and thus we will limit our discussions to just the FOM in this paper. We aim to achieve high SNR or FOM values by optimizing the sensitivity of our system. Besides the sensitivity and FOM, other

possible factors that affect the performance of a SPR biosensor include; noise from the optical system and readout electronics, mechanical stability of the sensor, resolution and the limit of detection [144] of the sensor which can be evaluated when the physical sensor is tested.

5.4 SFG-Based Sensor

For operation at visible wavelengths, we use the nonlinear process of SFG, where the incident FW is a femtosecond Gaussian laser pulse in the near infrared range. Most metals have a strong plasmonic response at frequencies in this range [145]. Spectral modulations in the reflected linear field for ultrashort pulses in the Kretschmann configuration have been reported at these frequencies [146, 147]. The plasmon-enhanced spectral modulation of the incident light when it couples into surface plasmon polaritons subsequently generates more spectral signatures in the reflected nonlinear light through nonlinear polarization.

As a demonstration, we use a $10fs$ laser pulse with a peak wavelength of 1178 *nm* shown in Fig. 5.2(a) which is incident on a 50 *nm* thick gold film chosen for optimum resonance [148], to generate a sum-frequency field at 588.6 *nm*. Fig. 5.2(b), shows the reflected FW, with the hole in the spectrum representing the coupling of light into surface plasmon polaritons. The angle of incidence for which light couples into surface plasmon polaritons is given by [27]

$$\theta_c(\omega) = \arcsin\left[\sqrt{\frac{\varepsilon_2(\omega)\varepsilon_3(\omega)}{\varepsilon_1(\varepsilon_2(\omega)+\varepsilon_3(\omega))}}\right]. \tag{5.11}$$

The calculated plasmon coupling angle at the centre wavelength using Eq. (5.11) is $\theta = 42.30^o$, which corresponds well to the hole location in Fig. 5.2(b). The reflected sum-frequency field is shown in Fig. 5.2(c), with the maximum intensity corresponding to the surface plasmon coupling angle of the FW. Finally Fig. 5.2(d) shows the SFG spectrum normalized for each angle of incidence, to clearly show the position of SFG spectral peak close to SPR. The normalization is done by dividing the spectrum for each angle of incidence by the peak spectral value for that given angle.

A close look at Fig. 5.2(d) shows shifts in the normalized SFG spectral peak position between incidence angles of 42.2^o and 42.4^o, which corresponds to plasmon coupling range of the FW, confirmed by the minimum in the reflected FW in Fig. 5.2(b). We calculate

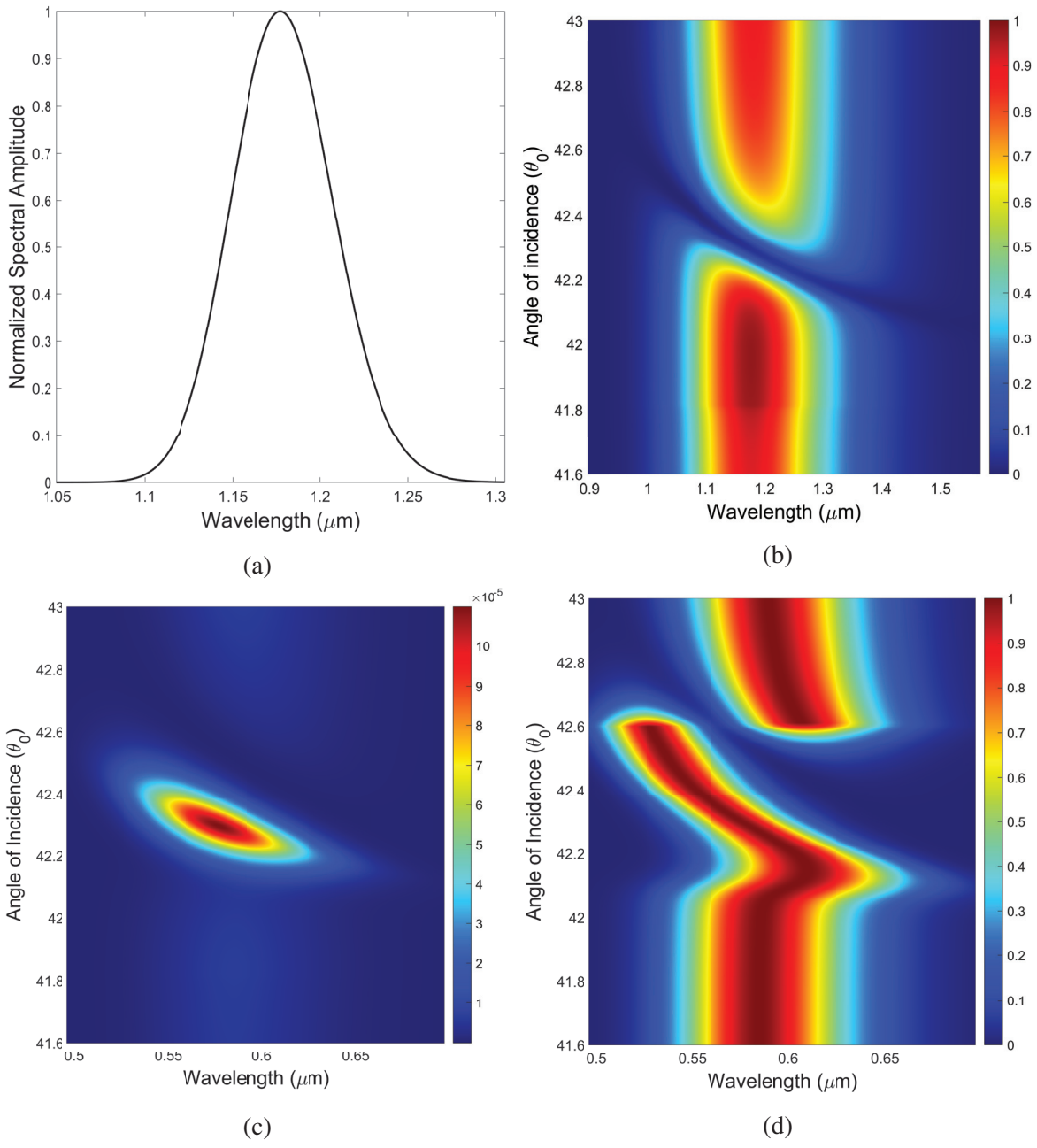

Figure 5.2: Far-field spectra of (a) incident FW (b) reflected fundamental spectrum from gold film (c) reflected SFG (d) normalized SFG spectrum. Incident pulse duration is $t_p = 10fs$.

the sensitivity for two incident angles within this range for $\varepsilon_3 = 1$ (air). We chose $\theta = 42.35^o$, where there is a linear blue shift in the spectrum and $\theta = 42.66^o$, where we have a switch in the SFG spectrum which is qualitatively similar to that observed in the Fraunhofer diffraction of light from a circular aperture [149].

Fig. 5.3(a) and Fig. 5.3(b) show the shifts in the SFG spectrum with changes in the refractive index n_3(air) at $\theta = 42.35^o$ and $\theta = 42.66^o$ respectively. We use Eq. (5.8) and Eq. (5.9) together with the plots to calculate the sensitivity and the FOM. The proposed sensor can also be used for biological and chemical sensing in solution and therefore the knowledge of its sensitivity in water is desired. We use the wavelength dependent permittivity of water from [83] in our calculations.

The shifts in the SFG spectrum as a result of changing the refractive index of the sample n_3(water) at $\theta = 63.60^o$ (linear shift) and $\theta = 64.04^o$ (spectral switch) are shown in Fig. 5.3(c) and Fig. 5.3(d) respectively. These spectral plots are used to calculate the sensitivity and FOM of the sensor for water solution samples. A comparison of the sensitivity and FOM of both linear and SFG Kretschmann-based sensor modalities in both air and water is presented in Table 5.1. It should be noted that the measurement range in the linear shift region is not limited to $\Delta n = 0.003 n_3$ and can be extended to $\Delta n = 0.01 n_3$, which is comparable to the sensing range of most linear plasmonic sensors [150]. The narrow measurement range in the region where we have a spectral switch in our sensor could be very useful in sensing samples that undergo very small refractive index changes.

Table 5.1: Comparison of sensitivity and FOM values of linear and SFG Kretschmann based sensor modalities in air and water.

	Linear (588 nm)	SFG (588 nm)
$S_{air}(\lambda)(nm/RIU)$	2600	14000-35000
$S_{water}(\lambda)(nm/RIU)$	1000	6400-28000
$FOM_{air}((RIU^{-1})$	22	467-583
$FOM_{water}(RIU^{-1})$	16	107-222

We can infer from Table 5.1 that both the sensitivity and FOM increase by an order of magnitude in either air or water when we employ an SFG-based versus linear sensor modality. Finally, we observe a decrease in both the sensitivity and FOM of both linear and

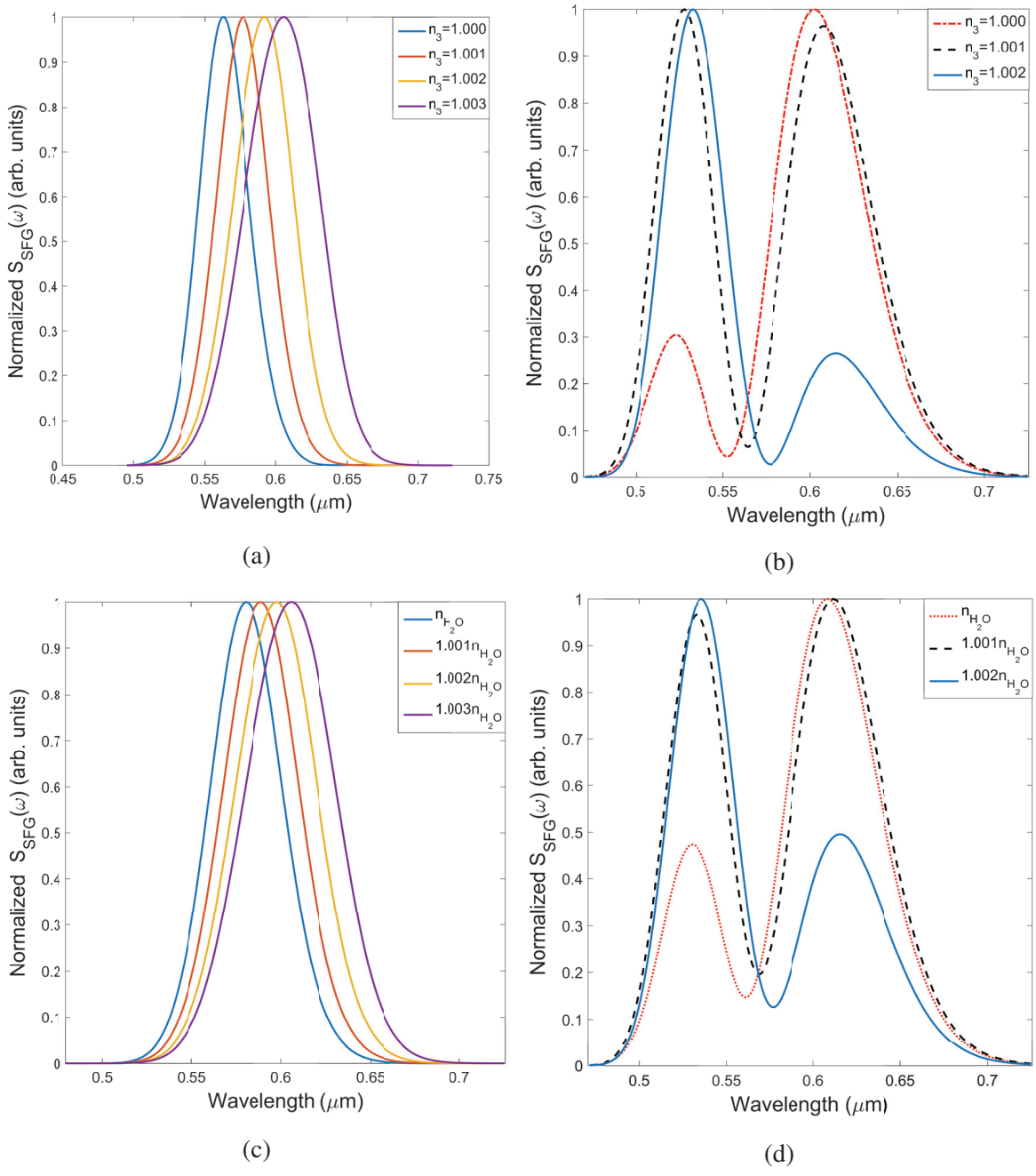

Figure 5.3: Reflected far-field SFG spectrum at (a) $\theta = 42.35^o$ in air ($S(\lambda) = 14000$ nm/RIU, $FOM = 222$ RIU^{-1}) (b) $\theta = 42.66^o$ in air ($S(\lambda) = 35000$ nm/RIU, $FOM = 583$ RIU^{-1}) (c) $\theta = 63.60^o$ in water ($S(\lambda) = 6400$ nm/RIU, $FOM = 107$ RIU^{-1}) (d) $\theta = 64.04^o$ in water ($S(\lambda) = 28000$ nm/RIU, $FOM = 467$ RIU^{-1}). The incident pulse duration is $t_p = 10fs$.

nonlinear sensors in water compared to their operation in air. The analytical expression for sensitivity with wavelength modulation of a Kretschmann-based plasmonic sensor is given by [76]

$$S(\lambda) = \frac{\varepsilon_2^2(\omega)}{\frac{1}{2}\cdot\left|\frac{d\varepsilon_2(\omega)}{d\lambda}\right|\cdot n_3^3 + \frac{\varepsilon_2(\omega)n_3}{n_p}\cdot\frac{dn_1}{d\lambda}\cdot(\varepsilon_2^2(\omega)+n_3^2)}. \tag{5.12}$$

Eq. (5.12) shows that the sensitivity of a linear Kretschmann-based plasmonic sensor decreases with increase refractive index of the sensing medium. Since the operation of our nonlinear plasmonic sensor is fundamentally based on the principle of the linear Kretschmann sensor through the nonlinear interaction of plasmon-enhanced fundamental waves, we also expect the sensitivity of our nonlinear sensor to decrease with increasing refractive index of the sensing medium. The FOM is defined in terms of the sensitivity and we expect a decrease in sensitivity to be matched with a decrease in the FOM.

5.5 DFG-Based Sensor

The mid-infrared range is very useful for sensing organic and inorganic molecules [112]. To generate nonlinear signal at this range, we use a dual-wavelength Gaussian pulse and the nonlinear process of DFG. Laser sources with dual wavelengths have been used experimentally to generate sum-frequency waves (SFW) and difference-frequency waves (DFW) in bulk crystals [151–155], which demonstrates the potential use of such sources to generate new frequencies in plasmonic materials.

We use a dual-wavelength pulse with peaks at 660 nm ($\omega = 2.854\times10^{15}\ rads/s$) and 780 nm ($\omega = 2.415\times10^{15}\ rads/s$), each with a pulse duration of $20fs$. The FW and reflected linear spectrum from the sensor are depicted in Fig. 5.4(a) and Fig. 5.4(b), respectively. The reflected linear spectrum has holes corresponding to the surface plasmon coupling angle for each peak wavelength. Using Eq. (5.1), we obtain $\theta_{spp} = 43.86^o$ and $\theta_{spp} = 42.97^o$ for the peaks at 660 nm and 780 nm, respectively, which agrees well with the minimum angle positions in Fig. 5.4(b). The difference-frequency spectrum is shown in Fig. 5.4(c), with the peak frequency $\omega = 4.39\times10^{14}\ rads/s(4.29\ \mu m)$ corresponding to the difference between the frequency peaks in the FW. The normalized reflected difference-frequency spectrum is shown in Fig. 5.4(d).

Similarly to the SFG sensor, we use the normalized difference-frequency spectra (Fig. 5.4(d)) to estimate the angular region where the sensor is spectrally sensitive. For

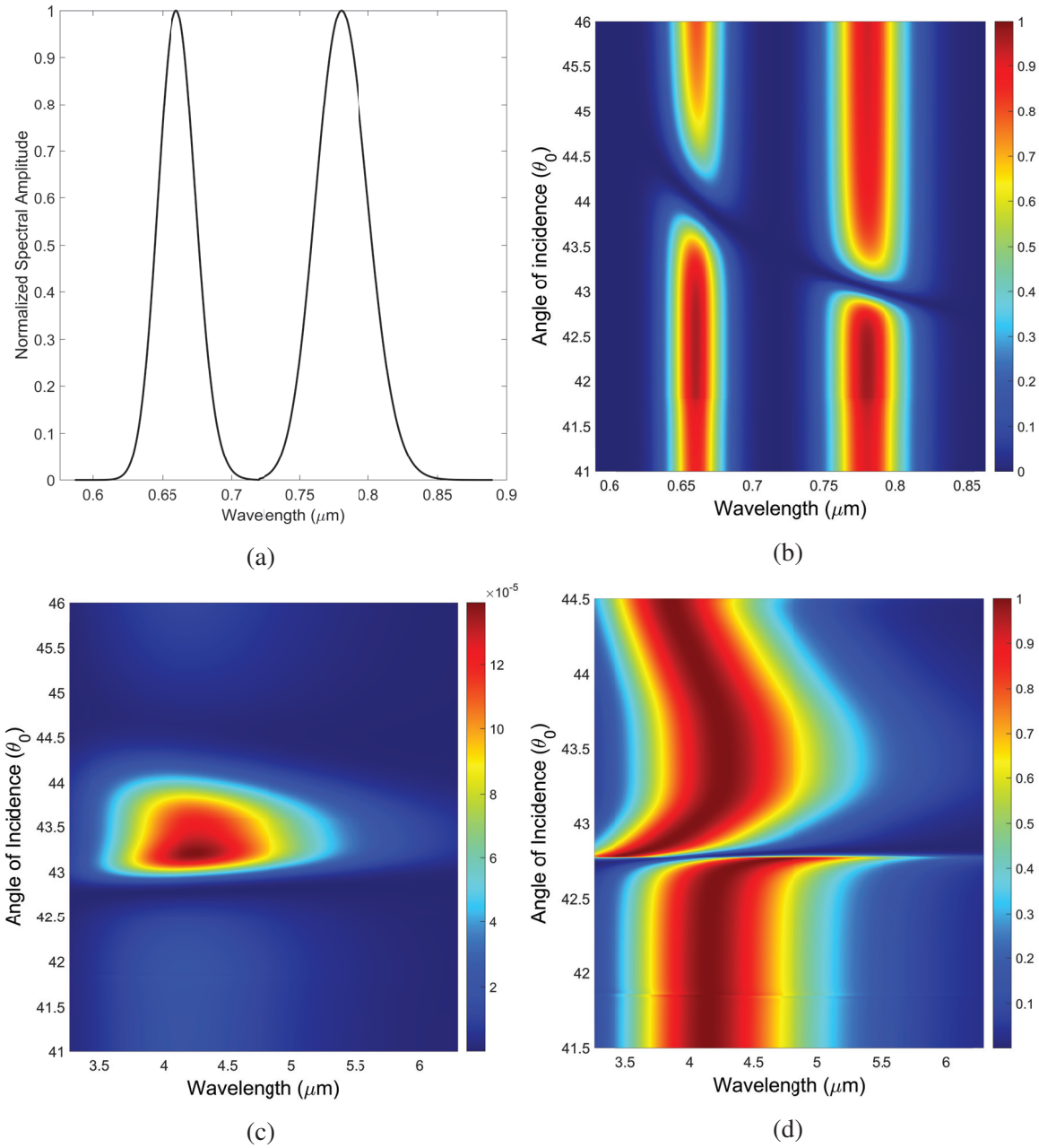

Figure 5.4: Far-field spectra of (a) incident FW (b) the reflected fundamental spectrum from gold film (c) reflected DFW (d) normalized DFW. The incident pulse duration is $t_p = 20fs$.

angles in the range $\theta_0 = 42.7^o - 42.9^o$, we have a giant spectral switch in the spectrum. For $\theta_0 = 42.9^o - 43.39^o$, we observe a red shift in the spectrum and finally a blue shift in the spectrum for $\theta_0 = 43.40^o - 43.59^o$. We proceed to calculate the sensitivity and FOM of our sensor in each of these regions using a representative angle of incidence for both air and water.

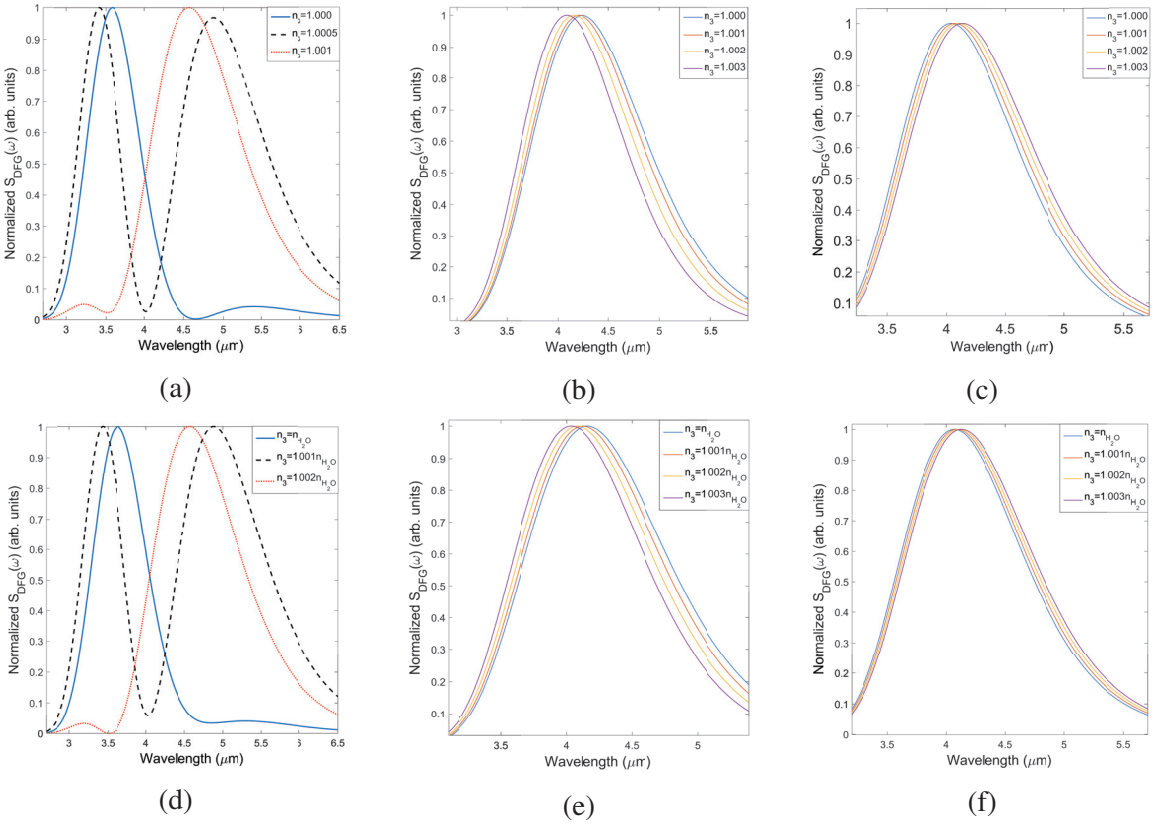

Figure 5.5: DFG spectral peak dependence on refractive index n_3 at (a) $\theta_0 = 42.8^o$ in air ($S(\lambda) = 1 \times 10^6$ nm/RIU, $FOM = 765$ RIU^{-1}) (b) $\theta_0 = 43.20^o$ in air ($S(\lambda) = 5 \times 10^4$ nm/RIU, $FOM = 40$ RIU^{-1}) (c) $\theta_0 = 44.00^o$ in air ($S(\lambda) = 3.2 \times 10^4$ nm/RIU, $FOM = 27$ RIU^{-1}) (d) $\theta_0 = 65.81^o$ in water ($S(\lambda) = 3.6 \times 10^5$ nm/RIU, $FOM = 300$ RIU^{-1}) (e) $\theta_0 = 66.90^o$ in water ($S(\lambda) = 3 \times 10^4$ nm/RIU, $FOM = 23$ RIU^{-1}) (f) $\theta_0 = 71.00^o$ in water($S(\lambda) = 2 \times 10^4$ nm/RIU, FOM = 16 RIU^{-1}). The incident pulse duration is $t_p = 20fs$.

Fig. 5.5 shows the dependence of spectral shifts at the peak DFG wavelength on refractive index change (n_3) in both air and water for different representative angles in the plasmon resonance range of the FW. We use these spectral shift plots to calculate the sensitivity and FOM based on Eq. (5.8) and Eq. (5.9). The Kretschmann-based sensor cannot be used in the MIR as a linear sensor due to the large metal losses at these frequencies. Since

we cannot compare the performance of our DFG sensor to a linear Kretschmann-based sensor in this range, we have used the sensitivity and FOM values of a recently proposed high sensitivity linear MIR sensor based on metallic nanostructures [156] for comparison. A comparison of the sensitivity and FOM of both linear and nonlinear sensor modalities is presented in Table 5.2.

Table 5.2: Comparison of sensitivity and FOM values of a linear MIR sensor and a DFG Kretschmann based sensor in air and water.

	Linear MIR sensor [156]	DFG (4.29 μm)
$S_{air}(\lambda)(nm/RIU)$	8000	$3.2 \times 10^4 - 1.0 \times 10^6$
$S_{water}(\lambda)(nm/RIU)$	950	$2.0 \times 10^4 - 3.6 \times 10^5$
$FOM_{air}((RIU^{-1})$	10.26	27-765
$FOM_{water}(RIU^{-1})$	1.76	16-300

The sensitivity of our DFG Kretschmann-based sensor in both air and water is three orders of magnitude higher than that presented in Nguyen-Huu et al [156]. As a result of the high sensitivity values of the DFG sensor, the FOM is almost two orders of magnitude higher than those of the linear sensor. As was the case with the SFG nonlinear sensor, the values of the sensitivity and FOM in water are about half those measured in air.

Nonlinear signals are very difficult to detect due to very small magnitudes of metal nonlinear susceptibilities. It is therefore imperative that we estimate the optical power of the reflected SFG/DFG field to make sure they can be easily detected in order to take advantage of the very high sensitivity values of our sensor. To do this, we assume an incident pulse in both cases has an input power of 100 mW, which is quite reasonable for most femtosecond laser sources. The attenuation from optical elements such as collimators, dichroic mirrors, polarizers, microscope objectives etc., which, incidentally, were all used in a recent study of reflected SHG from conducting thin films [63], was estimated to be 40%. Therefore the power of the source just before incidence on the sample is around 60 mW. From Fig. 5.2(c) and Fig. 5.4(c), we observe the power of the reflected nonlinear field to be approximately 10^{-6} times the incident power, thereby leaving us with 60 nW of power immediately after reflection from the sample. Since the reflected fields have to go through optical elements before detection, and assuming a combined attenuation of 40%,

this results in a detectable signal of 36 nW. This estimate gives us a reasonable signal power level, which commercial spectrometers such as the Ocean optics USB4000, can easily detect. Finally, nonlinear optical measurements from [63] for an incident optical power of 38 mW generated reflected nonlinear signals with a high SNR, which bodes well for our proposed sensor.

Our results also indicate that both the sensitivity and FOM strongly depend on the angle of incidence of the FW. Thus accurate control of the incidence angle is very important for the realization of this sensor. Such control can be achieved by using a goniometer, such as the WT-120 High Precision Motorized goniometer from PI GmbH, which has a resolution of 0.0001^o. With such precision, we can accurately control our incident angle.

5.6 Conclusion

We have proposed the geometry and calculated the sensitivity and FOM of a Kretschmann-based nonlinear plasmonic sensor, operating at both visible and MIR wavelengths through the SFG and DFG nonlinear processes. We demonstrated at specific angles of incidence close to surface plasmon resonance of the FW very high sensitivity values of 1×10^6 nm/RIU and 3.5×10^4 nm/RIU for the DFG and SFG processes respectively in air. Our maximum sensitivity value is three orders of magnitude higher than the wavelength sensitivity of a traditional linear Kretschmann-based sensor. The maximum FOM values of 583 RIU^{-1} and 765 RIU^{-1} for reflected SFG and DFG are an order of magnitude higher than the values typical of a traditional Kretschmann sensor. The maximum sensitivity value for measurements in water, which is highly relevant for biosensing applications, was also three orders of magnitude higher than that of a traditional Kretschmann sensor, making the proposed sensor especially suitable for biological or chemical sensing. Besides the large values of the calculated sensitivity, the proposed sensor gives us the unique ability to operate a Kretschmann-based plasmonic sensor in the MIR, which is otherwise impossible to do in the linear regime. An estimation of the nonlinear signal power from the sensor showed that the nonlinear signal could be easily detected with commercially available spectrometers. We have used a well known geometry, which is very easy to fabricate, and effectively transformed it into an extremely sensitive, versatile surface plasmon sensor using its nonlinear optical properties alone.

Chapter 6

Relative SHG Measurements of Metal Thin Films: Gold, silver, aluminum, cobalt, chromium, germanium, nickel, antimony, titanium, titanium nitride, tungsten, zinc, silicon and indium tin oxide

Franklin Che, Serge Grabtchak, William Whelan, Sergey A Ponomarenko and Michael Cada

Published in: Results in Physics, January 10, 2017, Vol. 7, 593

URL: http://www.sciencedirect.com/science/article/pii/S2211379716301140

6.1 Abstract

We have experimentally measured the surface second-harmonic generation (SHG) of sputtered gold, silver, aluminum, zinc, tungsten, copper, titanium, cobalt, nickel, chromium, germanium, antimony, titanium nitride, silicon and indium tin oxide thin films. The second-harmonic response was measured in reflection using a 150 fs p-polarized laser pulse at 1561 nm. We present a clear comparison of the SHG intensity of these films relative to each other. Our measured relative intensities compare favorably with the relative intensities of metals with published data. We also report for the first time to our knowledge the surface SHG intensity of tungsten and antimony relative to that of well known metallic thin films such as gold and silver.

6.2 Introduction

Surface SHG is a very useful technique for generating second order nonlinearities in systems with inversion symmetry [157, 158]. From the early experimental observation of surface SHG in metals in the 60's and 70's [80, 85, 86, 88, 102, 103] to the present day [159–163], a lot of experimental data has been generated for the surface SHG and susceptibility components of many metals. There is a lot of published experimental data on the surface SHG of metallic films such as Au, Ag and Al [164–166]. However, most of these studies typically cover narrow frequency ranges, illumination angles and film thicknesses.

Published experimental data on SHG in other metallic thin films is even more scarce. Unlike the ready availability of experimental data on the linear optical properties of metal thin films [83, 84], SHG data for these same materials is hard to come by and therefore very much cherished. Thus any new addition to the experimental data of SHG for different thin films, using different sources and illumination configurations is very useful especially for researchers who need some kind of starting reference for studying a given thin film.

In our study, we set out to investigate the reflected SHG from a variety of metal and semiconductor thin films and to develop a simple yet useful relative calibration system for these films. We examined the SHG intensity of Au, Ag, Al, Co, Cr, Ge, Ni, Sb, Ti, TiN, W, Zn, Si and ITO. For an incidence angle of 23.6^o and a wavelength of 1561 nm, we were able to calibrate the surface SHG response of these thin films relative to each other and to well studied films such as Au and Ag.

6.3 Experimental Setup

We irradiate the thin films used in our study using the configuration shown in Fig. 6.1, where θ_0 is the incident angle. The conducting films are deposited on a glass substrate. All the thin films were grown through magnetron sputtering, with the thickness of the films monitored during growth. The films were grown to thicknesses of either 50 nm or 100 nm.

We used a linearly polarized fiber laser source, with a central wavelength of 1561 nm, a pulse width of 150 fs. The average incident power range at the sample plane, after propagating through the system optics was 8 mW - 70 mW. The incident laser beam was collimated using a broadband collimator, passed through a linear polarizer and rotated to generate p-polarized light. This p-polarized light was focused on the thin film sample using a 0.4 N.A reflective microscope objective at an angle of incidence of 23.6^o. The angle of incidence is not very critical in these studies, since surface plasmon coupling is not involved. The reflected linear and second-harmonic beams were collected and collimated by the same microscope objective. They were separated by a dichroic mirror, with the second-harmonic wave aligned for p-polarization and detected with a spectrometer. The incident light intensity at the source plane was measured regularly and the variation was less than 4 %.

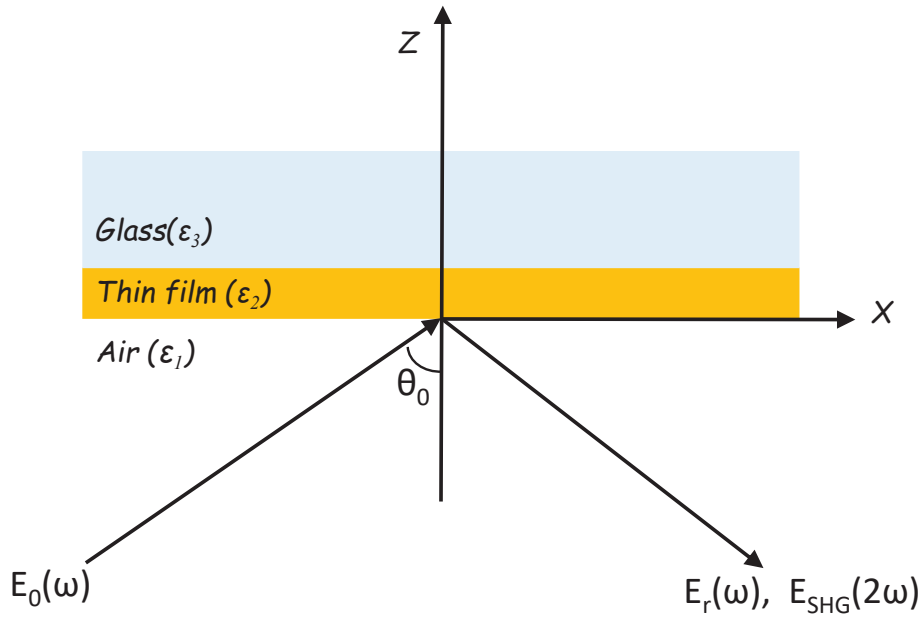

Figure 6.1: Irradiation configuration.

6.4 Results

Fig. 6.2 shows both the incident wave spectrum and the SHG spectrum for a 50 nm thick Au film when irradiated with a 38 mW, 150 fs laser centered at 1561 nm. We use the same source for the rest of our measurements and vary the intensity from 8 mW to 70 mW.

Fig. 6.3 shows both the measured second-harmonic intensity of p-polarized light for 100 nm thick conducting thin films. We observe that the second-harmonic intensity profiles split roughly into four groups. Group A consists of Au, Ag, Al and W and this group has the highest second-harmonic nonlinear response of our system. This group of metals has also being well studied. We can see from [165] that they all have comparable SHG signals for p-polarized light. Group B consists of Cu, Ti, Co and Ni with the signals 30% weaker than those of group A. Group C consists of Cr, Ge, Zn, Sb and TiN, which have 15% weaker SHG intensity compared to group B. Finally, group D films consisting of Si and ITO which are both semiconductors have the weakest measured intensity with their SHG intensity being an order of magnitude lower than that of group A.

Some of the materials in Fig. 6.3 were grown to just 50 nm in order to examine any dependence of thickness on the second-harmonic response of the films. The results are shown in Fig. 6.4. We do not observe any significant difference between the second order response of the 100 nm films compared to the 50 nm films. This is consistent with the

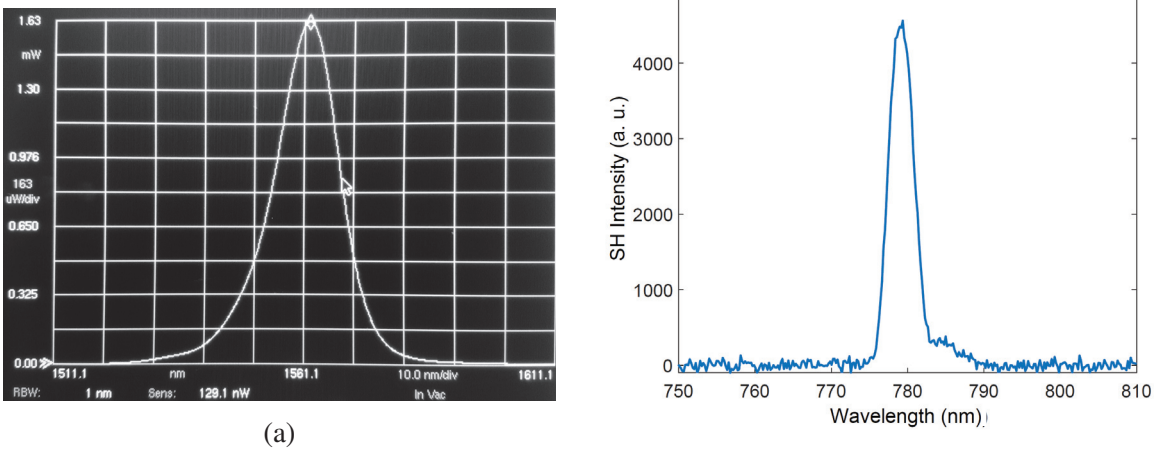

(a) (b)

Figure 6.2: (a) Incident fundamental spectrum at 1561 nm (b) SHG spectra of a 50 nm thick Au film.

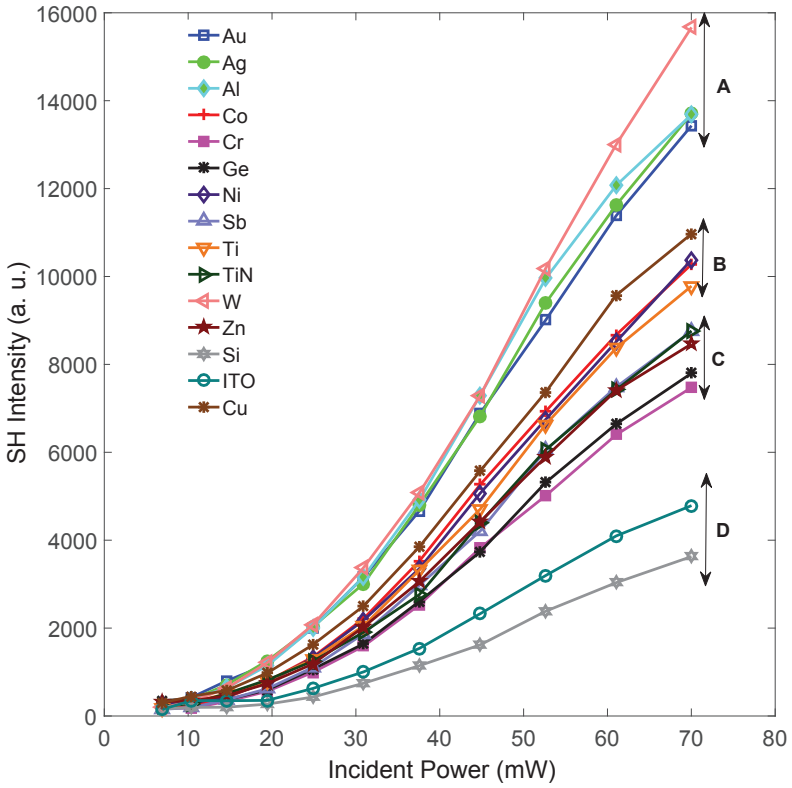

Figure 6.3: Measured SHG intensity for 100 nm thick films.

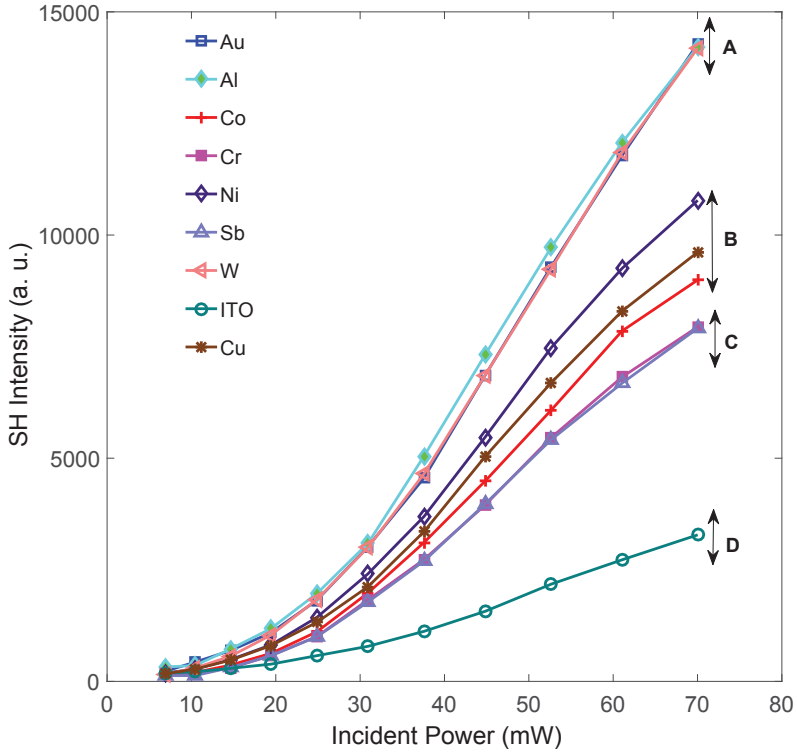

Figure 6.4: Measured SHG intensity for 50 nm thick films.

results in [167], where little variation in SHG intensity is observed in films with thickness ranging between 50 nm - 100 nm.

A power dependence test of the reflected second harmonic wave is shown in Fig. 6.5 for sample thin films from the different groups identified. Linear regression is then applied to the log-log plots revealing a second-order dependence of the SHG intensity to the incident power.

6.5 Conclusions

We have characterized the relative SHG intensity of various metal and semiconductor thin films using a 1561 nm p-polarized incident source. In cases where published experimental data for SHG was available, we found that our relative SHG intensities matched the relative intensities from the published data. In the case of W and Sb thin films where little or no experimental data is available for surface SHG, we can draw useful conclusions on the strength of their surface second-harmonic nonlinearities. We can see clearly from Fig. 6.3 that W has a comparable second-harmonic response to Au and Ag and the response of

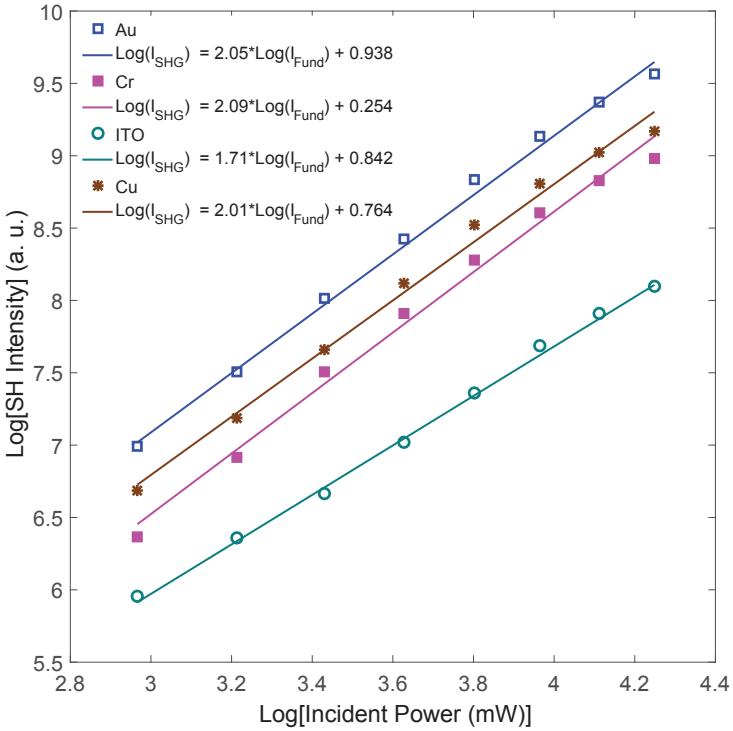

Figure 6.5: Log-log plot of the SHG intensity of Au, Cr, Cu and ITO. The lines represent the linear regression data fit.

antimony is closer to that of Cr, Zn and Ge. This experimental data serves as a first point of reference for the surface SHG response of thin films whose experimental data is not readily available.

Chapter 7

Conclusion

This chapter summarizes the results from this study and discusses possible directions for future research on this subject.

7.1 Conclusion

In this thesis, the main goal was to explore the nonlinear optical effects of generating second-order electromagnetic fields from a conducting thin film close to surface plasmon resonance using a single polychromatic incident light source. Classical electromagnetic field theory was used to study the coupling of light into surface plasmons and the nonlinear interaction of light in a conducting film.

Suitable and realistic polychromatic incident sources were formulated for these studies. We also used well-known models to describe the linear and nonlinear optical properties of the conductors such as the permittivity and second-order surface susceptibility components. Both analytical and numerical methods were used to calculate fields resulting from plasmon-enhanced nonlinear interactions.

The main findings of our studies on nonlinear interaction of polychromatic light sources in conducting films is broken down into four sections. In each section, we provide a general description of the main results.

Generation of SFG and DFG Waves using a single polychromatic source. We theoretically demonstrated for the first time, to the best of our knowledge, the generation of plasmon enhanced sum- and difference-frequency waves from the surface of a metal using a polychromatic source in the Kretschmann illumination configuration. We used ultra-short femtosecond Gaussian and dual-wavelength Gaussian pulses to generate sum- and difference-frequency waves, respectively. Nonlinear waves in the visible and MIR range were generated with a very strong enhancement of the nonlinear waves close to SPR of the incident light source.

Spectral Changes in the reflected nonlinear spectrum generated using a polychromatic source.
Besides the generation of sum-and difference-frequency waves in reflection from a metal surface, we also demonstrated changes in the nonlinear wave spectrum close to surface plasmon resonance of the fundamental wave. We showed spectral shifts and switches in both the sum- and difference-frequency spectra. We also demonstrated a strong correlation between these spectral effects and properties of the incident FW such as the pulse duration, with stronger effects observed for shorter pulses. Finally, we demonstrated a strong dependence of the reflected nonlinear spectral peak position on the material properties of the dielectric material surrounding the metal film.

High sensitivity refractive index sensor based on the Kretschmann configuration.
In this study, we proposed and investigated a simple, robust and high sensitivity refractive index sensor, based on the second-order nonlinear processes of sum- and difference-frequency generation. The calculated sensor performance parameters showed very high sensitivity and FOM values with the ability to operate over a wide wavelength range. We demonstrated a spectral sensitivity at mid-infrared wavelengths, that was two orders of magnitude higher than current values available in the literature.

Relative strengths of SHG waves reflected from conducting thin films.
Finally, we successfully estimated relative strengths of SHG waves, reflected from a large variety of conducting thin films using an infrared femto-second laser source. The films were sputtered on a glass substrate and illuminated directly from the top, with the SHG light measured in reflection. Conducting films of thickness 50nm and 100 nm were used in this study, with SHG fields from tungsten and antimony shown to be comparable to that of silver and gold. The information gathered from this study can be used to determine the suitability of conducting thin film material for our proposed nonlinear plasmonic sensor.

7.2 Future Work

In our studies, we demonstrated the immense potential of our proposed nonlinear plasmonic sensor. Its simplicity and very high sensitivity stands out and makes it a excellent candidate for a possible commercial plasmonic biosensor. However, there is still some work to be done before its viability can be fully demonstrated. A first step would be an experiment to measure the wavelength sensitivity, something we could not do due to time constraints and

other limitations in our laboratory.

Lastly, our current design is far from optimum and we can improve on the sensitivity through a number of independent investigations such as the use of different metals, varying metal thickness, using a multilayered structure with different materials and utilizing metallic nanostructures.

Bibliography

[1] P. B. Johnson and R. W. Christy. Optical constants of the noble metals. *Phys. Rev. B*, 6(12):4370–4379, 1972.

[2] J. Homola. *Surface Plasmon Resonance Based Sensors*. Springer Series on Chemical Sensors and Biosensors. Springer Berlin Heidelberg, 2006.

[3] R. W. Boyd. *Nonlinear Optics, II ed*. Academic, Boston, 2003.

[4] T. H. Maiman. Stimulated optical radiation in ruby. *Nature*, 187:493–494, 1960.

[5] Y. R. Shen. Surface nonlinear optics: a historical perspective. *IEEE Journal of Selected Topics in Quantum Electronics*, 6(6):1375–1379, 2000.

[6] P. A. Franken, A. E. Hill, C. W. Peters, and G. Weinreich. Generation of optical harmonics. *Physical Review Letters*, 7(4):118, 1961.

[7] R. A. Soref and H. W. Moos. Optical second-harmonic generation in znscds and cdscdse alloys. *Journal of Applied Physics*, 35(7):2152–2158, 1964.

[8] R. C. Miller. Optical second harmonic generation in piezoelectric crystals. *Applied Physics Letters*, 5(1):17–19, 1964.

[9] R. W. Terhune, P. D. Maker, and C. M. Savage. Optical harmonic generation in calcite. *Physical Review Letters*, 8(10):404, 1962.

[10] J. A. Giordmaine. Mixing of light beams in crystals. *Physical Review Letters*, 8(1):19, 1962.

[11] N. Bloembergen and P. S. Pershan. Light waves at the boundary of nonlinear media. *Physical Review*, 128(2):606, 1962.

[12] J. Ducuing and N. Bloembergen. Observation of reflected light harmonics at the boundary of piezoelectric crystals. *Physical Review Letters*, 10(11):474, 1963.

[13] F. Brown, R. E. Parks, and A. M. Sleeper. Nonlinear optical reflection from a metallic boundary. *Physical Review Letters*, 14(25):1029, 1965.

[14] R. H. Ritchie. Plasma losses by fast electrons in thin films. *Physical Review*, 106(5):874, 1957.

[15] A. Otto. Excitation of nonradiative surface plasma waves in silver by the method of frustrated total reflection. *Zeitschrift für Physik*, 216(4):398–410, 1968.

[16] E. Kretschmann and H. Raether. Notizen: radiative decay of non radiative surface plasmons excited by light. *Zeitschrift für Naturforschung A*, 23(12):2135–2136, 1968.

[17] J. Zenneck. Propagation of plane em waves along a plane conducting surface. *Ann. Phys.(Leipzig)*, 23(1):907, 1907.

[18] A. Sommerfeld. Propagation of waves in wireless telegraphy. *Ann. Phys*, 28(3):665–736, 1909.

[19] H. J. Simon, D. E. Mitchell, and J. G. Watson. Optical second-harmonic generation with surface plasmons in silver films. *Phys. Rev. Lett.*, 33:1531–1534, 1974.

[20] M. Fleischmann, P. J. Hendra, and A. J. McQuillan. Raman spectra of pyridine adsorbed at a silver electrode. *Chemical Physics Letters*, 26(2):163–166, 1974.

[21] C. K. Chen, A. R. B. de Castro, and Y. R. Shen. Surface-enhanced second-harmonic generation. *Phys. Rev. Lett.*, 46(2):145–148, 1981.

[22] A. Bouhelier, M. Beversluis, A. Hartschuh, and L. Novotny. Near-field second-harmonic generation induced by local field enhancement. *Phys. Rev. Lett.*, 90:013903, 2003.

[23] A. Nahata, R. A. Linke, T. Ishi, and K. Ohashi. Enhanced nonlinear optical conversion from a periodically nanostructured metal film. *Opt. Lett.*, 28(6):423–425, 2003.

[24] S. Palomba and L. Novotny. Nonlinear excitation of surface plasmon polaritons by four-wave mixing. *Phys. Rev. Lett.*, 101(5):056802, 2008.

[25] N. A. Papadogiannis, P. A. Loukakos, and S. D. Moustaizis. Observation of the inversion of second and third harmonic generation efficiencies on a gold surface in the femtosecond regime. *Optics communications*, 166(1):133–139, 1999.

[26] M. Lippitz, M. A. van Dijk, and M. Orrit. Third-harmonic generation from single gold nanoparticles. *Nano letters*, 5(4):799–802, 2005.

[27] L. Novotny and B. Hecht. *Principles of Nano-Optics*. Cambridge University, 2006.

[28] Q. Li, C. W. Kuo, Z. Yang, P. Chen, and K. C. Chou. Surface-enhanced ir-invisible sum frequency generation vibrational spectroscopy. *Phys. Chem.*, 11:3436–3442, 2009.

[29] Y. Uchiho, M. Shimojo, K. Furuya, and K. Kajikawa. Optical response of gold-nanoparticle-amplified surface plasmon resonance spectroscopy. *The Journal of Physical Chemistry C*, 114(11):4816–4824, 2010.

[30] K. B. Eisenthal. Liquid interfaces probed by second-harmonic and sum-frequency spectroscopy. *Chemical Reviews*, 96(4):1343–1360, 1996.

[31] C. S. Tian and Y. R. Shen. Recent progress on sum-frequency spectroscopy. *Surface Science Reports*, 69(2):105–131, 2014.

[32] H. Linnenbank, Y. Grynko, J. Förstner, and S. Linden. Second harmonic generation spectroscopy on hybrid plasmonic/dielectric nanoantennas. *Light: Science and Applications*, 5(1):e16013, 2016.

[33] A. Hohenau, J. R. Krenn, F. J. Garcia-Vidal, S. G. Rodrigo, L. Martin-Moreno, J. Beermann, and S. I. Bozhevolnyi. Spectroscopy and nonlinear microscopy of gold nanoparticle arrays on gold films. *Physical Review B*, 75(8):085104, 2007.

[34] K. Tilbury and P. J. Campagnola. Applications of second-harmonic generation imaging microscopy in ovarian and breast cancer. *Perspectives in medicinal chemistry*, 7:21, 2015.

[35] J. H. Jang, J. Jacob, G. Santos, T. R. Lee, and S. Baldelli. Image contrast in sum frequency generation microscopy based on monolayer order and coverage. *The Journal of Physical Chemistry C*, 117(29):15192–15202, 2013.

[36] Y. Han, V. Raghunathan, R. Feng, H. Maekawa, C. Chung, Y. Feng, E. O. Potma, and N. H. Ge. Mapping molecular orientation with phase sensitive vibrationally resonant sum-frequency generation microscopy. *The Journal of Physical Chemistry B*, 117(20):6149–6156, 2013.

[37] J. N. Anker, W. P. Hall, O. Lyandres, N. C. Shah, J. Zhao, and R. P. Van Duyne. Biosensing with plasmonic nanosensors. *Nat. Mater.*, 7:442–453, 2008.

[38] K. M. Mayer and J. H. Hafner. Localized surface plasmon resonance sensors. *Chem. Rev.*, 111(6):3828–3857, 2011.

[39] J. Butet, I. Russier-Antoine, C. Jonin, N. Lascoux, E. Benichou, and P. Brevet. Sensing with multipolar second harmonic generation from spherical metallic nanoparticles. *Nano Lett.*, 12(3):1697–1701, 2012.

[40] P. C. Ray. Size and shape dependent second order nonlinear optical properties of nanomaterials and their application in biological and chemical sensing. *Chemical reviews*, 110(9):5332–5365, 2010.

[41] J. Butet, P. F. Brevet, and O. J. F. Martin. Optical second harmonic generation in plasmonic nanostructures: From fundamental principles to advanced applications. *ACS nano*, 9(11):10545–10562, 2015.

[42] P. Y. Chen, C. Argyropoulos, and A. Alù. Enhanced nonlinearities using plasmonic nanoantennas. *Nanophotonics*, 1(3-4):221–233, 2012.

[43] S. B. Hasan, F. Lederer, and C. Rockstuhl. Nonlinear plasmonic antennas. *Materials Today*, 17(10):478–485, 2014.

[44] M. M. Fejer. Nonlinear optical frequency conversion. *Physics today*, 47(5):25–33, 1994.

[45] Y. Ge, J. Cao, Z. Shen, Y. Zheng, X. Chen, and W. Wan. Terahertz wave generation by plasmonic-enhanced difference-frequency generation. *J. Opt. Soc. Amer. B*, 31(7):1533–1538, 2014.

[46] M. A. Belkin, F. Capasso, A. Belyanin, D. L. Sivco, A. Y. Cho, D. C. Oakley, C. J. Vineis, and G. W. Turner. Terahertz quantum-cascade-laser source based on intracavity difference-frequency generation. *Nature Photonics*, 1(5):288–292, 2007.

[47] K. Fradkin, A. Arie, A. Skliar, and G. Rosenman. Tunable midinfrared source by difference frequency generation in bulk periodically poled ktiopo 4. *Applied physics letters*, 74(7):914–916, 1999.

[48] J. Wang, J. Sun, J. R. Kurz, and M. M. Fejer. Tunable wavelength conversion of ps-pulses exploiting cascaded sum-and difference frequency generation in a ppln-fiber ring laser. *IEEE photonics technology letters*, 18(20):2093–2095, 2006.

[49] E. Mimoun, L. De Sarlo, J. J. Zondy, J. Dalibard, and F. Gerbier. Sum-frequency generation of 589 nm light with near-unit efficiency. *Optics express*, 16(23):18684–18691, 2008.

[50] H. W. K. Tom, C. M. Mate, X. D. Zhu, J. E. Crowell, T. F. Heinz, G. A. Somorjai, and Y. R. Shen. Surface studies by optical second-harmonic generation: The adsorption of o 2, co, and sodium on the rh (111) surface. *Physical Review Letters*, 52(5):348, 1984.

[51] I. Arfaoui, V. Bermudez, G. Bottari, C. De Nadai, J. P. Jalkanen, F. Kajzar, D. A. Leigh, M. Lubomska, S. M. Mendoza, and J. Niziol. Surface enhanced second harmonic generation from macrocycle, catenane, and rotaxane thin films: Experiments and theory. *The Journal of Physical Chemistry B*, 110(15):7648–7652, 2006.

[52] R. Jin, J. E. Jureller, H. Y. Kim, and N. F. Scherer. Correlating second harmonic optical responses of single ag nanoparticles with morphology. *Journal of the American Chemical Society*, 127(36):12482–12483, 2005.

[53] M. Kauranen and A. V. Zayats. Nonlinear plasmonics. *Nat. Photon.*, 6:737–748, 2012.

[54] P. Guyot-Sionnest and A. Tadjeddine. Spectroscopic investigations of adsorbates at the metal electrolyte interface using sum frequency generation. *Chem. Phys. Lett.*, 172(5):341–345, 1990.

[55] A. Le Rille, A. Tadjeddine, W. Q. Zheng, and A. Peremans. Vibrational spectroscopy of a au(hkl)-electrolyte interface by in situ visible-infrared difference frequency generation. *Chem. Phys. Lett.*, 271(1-3):95–100, 1997.

[56] U. Emmerichs, H. J. Bakker, and H. Kurz. Generation of high-repetition rate femtosecond pulses tunable in the mid-infrared. *Opt. Commun.*, 111(5-6):497–501, 1994.

[57] S. Ehret and H. Schneider. Generation of subpicosecond infrared pulses tunable between 5.2 μm and 18 μm at a repetition rate of 76 mhz. *Appl. Phys. B*, 66:27–30, 1998.

[58] L. Mandel and E. Wolf. *Nonlinear Optics*. Wiley, 1973.

[59] J. C. Diels and W. Rudolph. *Ultrashort laser pulse phenomena*. Academic press, 2006.

[60] L. Wang, F. Che, S. A. Ponomarenko, and Z. Chen. Plasmon-enhanced spectral changes in surface sum-frequency generation with polychromatic light. *Opt. Express*, 21(12):14159–14168, 2013.

[61] F. Che, S. A. Ponomarenko, and M. Cada. Giant spectral transformations in plasmon-enhanced difference-frequency generation with polychromatic light. *Journal of Optics*, 18(12):125503, 2016.

[62] F. Che, S. A. Ponomarenko, M. Cada, and N. Nguyen-Huu. High sensitivity integrated visible to mid-infrared nonlinear plasmonic sensor. *IEEE Photonics Journal*, 9(4):1–11, 2017.

[63] F. Che, S. Grabtchak, W. M. Whelan, S. A. Ponomarenko, and M. Cada. Relative shg measurements of metal thin films: Gold, silver, aluminum, cobalt, chromium, germanium, nickel, antimony, titanium, titanium nitride, tungsten, zinc, silicon and indium tin oxide. *Results in Physics*, 7:593–595, 2017.

[64] S. A. Maier. *Plasmonics: Fundamentals and Applications*. Springer, 2007.

[65] E. Le Ru and P. Etchegoin. *Principles of Surface-Enhanced Raman Spectroscopy: and related plasmonic effects*. Elsevier, 2008.

[66] B. E. Sernelius. *Surface modes in physics*. John Wiley & Sons, 2011.

[67] E. D. Palik. *Handbook of optical constants of solids*, volume 3. Academic press, 1998.

[68] J. A. Dionne, L. A. Sweatlock, H. A. Atwater, and A. Polman. Planar metal plasmon waveguides: frequency-dependent dispersion, propagation, localization, and loss beyond the free electron model. *Physical Review B*, 72(7):075405, 2005.

[69] H. T. M. C. M. Baltar, K. Drozdowicz-Tomsia, and E. M. Goldys. Propagating surface plasmons and dispersion relations for nanoscale multilayer metallic-dielectric films. In Ki Young Kim, editor, *Plasmonics - Principles and Applications*, chapter 10. InTech, Rijeka, 2012.

[70] P. Yeh. *Optical Waves in Layered Media*. Series in Pure and Applied Optics. Wiley, 1998.

[71] W. C. Chew. *Waves and Fields in Inhomogeneous Media, II ed*. Institute of Electrical and Electronics Engineers, New York, 1995.

[72] J. Homola. Present and future of surface plasmon resonance biosensors. *Analytical and bioanalytical chemistry*, 377(3):528–539, 2003.

[73] G. G. Nenninger, M. Piliarik, and J. Homola. Data analysis for optical sensors based on spectroscopy of surface plasmons. *Measurement Science and Technology*, 13(12):2038, 2002.

[74] R. Karlsson and A. Fält. Experimental design for kinetic analysis of protein-protein interactions with surface plasmon resonance biosensors. *Journal of immunological methods*, 200(1-2):121–133, 1997.

[75] F. S. Ligler and C. R. Taitt. *Optical Biosensors: Today and Tomorrow*. Elsevier Science, 2011.

[76] A. Shalabney and I. Abdulhalim. Sensitivity-enhancement methods for surface plasmon sensors. *Laser & Photonics Reviews*, 5(4):571–606, 2011.

[77] K. D. Sattler. *Handbook of nanophysics: nanoelectronics and nanophotonics*. CRC Press, 2010.

[78] Y. R. Shen. The principles of nonlinear optics. *New York, Wiley-Interscience, 1984, 575 p.*, 1984.

[79] K. Wandelt and S. Thurgate. *Solid-Liquid Interfaces: Macroscopic Phenomena–Microscopic Understanding*, volume 85. Springer Science & Business Media, 2002.

[80] N. Bloembergen, R. K. Chang, S. S. Jha, and C. H. Lee. Optical second-harmonic generation in reflection from media with inversion symmetry. *Phys. Rev.*, 174(3):813–822, 1968.

[81] M. B. Raschke and Y. R. Shen. Nonlinear optical spectroscopy of solid interfaces. *Current opinion in solid state and materials science*, 8(5):343–352, 2004.

[82] H. M. Van Driel. Second-harmonic generation from metal surfaces: Beyond jellium. *Applied Physics A Solids and Surfaces*, 59(5):545–552, 1994.

[83] M. R. Querry, D. M. Wieliczka, and D. J. Segelstein. Water (h2o). In E. D. Palik, editor, *Handbook of Optical Constants of Solids*, pages 1059 – 1077. Academic Press, Burlington, 1997.

[84] S. Adachi. *The Handbook on Optical Constants of Metals: In Tables and Figures*. World Scientific, 2012.

[85] S. Jha. Nonlinear optical reflection from a metal surface. *Phys. Rev. Lett.*, 15(9):412–414, 1965.

[86] H. Sonnenberg and H. Heffner. Experimental study of optical second-harmonic generation in silver. *J. Opt. Soc. Am.*, 58(2):209–212, 1968.

[87] N. Bloembergen, R. K. Chang, and C. H. Lee. Second-harmonic generation of light in reflection from media with inversion symmetry. *Physical Review Letters*, 16(22):986, 1966.

[88] J. Rudnick and E. A. Stern. Second-harmonic radiation from metal surfaces. *Phys. Rev. B*, 4(12):4274–4290, 1971.

[89] J. E. Sipe, D. J. Moss, and H. M. Van Driel. Phenomenological theory of optical second-and third-harmonic generation from cubic centrosymmetric crystals. *Physical Review B*, 35(3):1129, 1987.

[90] M. Corvi and W. L. Schaich. Hydrodynamic-model calculation of second-harmonic generation at a metal surface. *Physical Review B*, 33(6):3688, 1986.

[91] W. L. Schaich and A. Liebsch. Nonretarded hydrodynamic-model calculation of second-harmonic generation at a metal surface. *Physical Review B*, 37(11):6187, 1988.

[92] M. Weber and A. Liebsch. Density-functional approach to second-harmonic generation at metal surfaces. *Physical Review B*, 35(14):7411, 1987.

[93] A. Liebsch and W. L. Schaich. Second-harmonic generation at simple metal surfaces. *Physical Review B*, 40(8):5401, 1989.

[94] W. L. Mochán and B. S. Mendoza. Second harmonic generation at crystal surfaces. *Journal of Physics: Condensed Matter*, 5(33A):A183, 1993.

[95] J. A. Maytorena, B. S. Mendoza, and W. L. Mochan. Theory of surface sum frequency generation spectroscopy. *Phys. Rev. B*, 57(4):2569–2579, 1998.

[96] J. A. Maytorena, W. L. Mochán, and B. S. Mendoza. Hydrodynamic model for sum and difference frequency generation at metal surfaces. *Physical Review B*, 57(4):2580, 1998.

[97] J. A. Maytorena, W. L. Mochán, and B. S. Mendoza. Hydrodynamic model for second-harmonic generation at conductor surfaces with continuous profiles. *Physical Review B*, 51(4):2556, 1995.

[98] J. E. Sipe, V. C. Y. So, M. Fukui, and G. I. Stegeman. Analysis of second-harmonic generation at metal surfaces. *Physical Review B*, 21(10):4389, 1980.

[99] A. V. Petukhov. Sum-frequency generation on isotropic surfaces: General phenomenology and microscopic theory for jellium surfaces. *Physical Review B*, 52(23):16901, 1995.

[100] S. A. Ponomarenko, H. Roychowdhury, and E. Wolf. Physical significance of complete spatial coherence of optical fields. *Phys. Lett. A*, 345(1-3):10–12, 2005.

[101] S. A. Ponomarenko and E. Wolf. Universal structure of field correlations within a fluctuating medium. *Phys. Rev. E*, 65:016602, 2001.

[102] N. Bloembergen. Wave propagation in nonlinear electromagnetic media. *Proc. IEEE*, 51:124–131, 1963.

[103] F. Brown, R. E. Parks, and A. M. Sleeper. Nonlinear optical reflection from a metallic boundary. *Phys. Rev. Lett.*, 14(25):1029–1031, 1965.

[104] J. C. Quail and H. J. Simon. Second-harmonic generation from silver and aluminum films in total internal reflection. *Phys. Rev. B*, 31(8):4900–4905, 1985.

[105] R. Reinisch and M. Neviere. Electromagnetic theory of diffraction in nonlinear optics and surface-enhanced nonlinear optical effects. *Phys. Rev. B*, 28(4):1870–1885, 1983.

[106] P. N. Prasad. *Nanophotonics*. Wiley, 2004.

[107] L. M. Liz-Marzan. Tailoring surface plasmons through the morphology and assembly of metal nanoparticles. *Langmuir*, 22:32–41, 2006.

[108] A. G. Lambert and P. B. Davies. Implementing the theory of sum frequency generation vibrational spectroscopy: A tutorial review. *Appl. Spectrosc. Rev.*, 40(2):103–145, 2005.

[109] M. R. X. de Barros, R. S. Miranda, T. M. Jedju, and P. C. Becker. High-repetition-rate femtosecond mid-infrared pulse generation. *Opt. Lett.*, 20(5):480–482, 1995.

[110] A. Lohner, P. Kruck, and W. W. Ruhle. Generation of 200 femtosecond pulses tunable between 2.5 and 5.5 μm. *Appl. Phys. B*, 59(2):211–213, 1994.

[111] J. D. Kafka, M. L. Watts, J. W. Pieterse, and R. L. Herbst. Mid-infrared pulse generation using a sub-picosecond opo. *Appl. Phys. B*, 60(5):449–452, 1995.

[112] C. Fischer and M. W. Sigrist. Mid-ir difference frequency generation. *Top. Appl. Phys.*, 89:99–143, 2003.

[113] V. S. Smentkowski. *Surface Analysis and Techniques in Biology*. Springer, 2014.

[114] S. A. Ponomarenko, G. P. Agrawal, and E. Wolf. Energy spectrum of a nonstationary ensemble of pulses. *Opt. Lett.*, 29(4):394–396, 2004.

[115] W. L. Mochan, J. A. Maytorena, and B. S. Mendoza. Visible infrared difference frequency generation at cn covered au. *Phys. Status Solidi A*, 170(2):357–363, 1998.

[116] J. M. Evans, D. E. Spence, D. Burns, and W. Sibbett. Dual-wavelength self-mode-locked ti:sapphire laser. *Opt. Lett.*, 18(13):1074–1076, 1993.

[117] H. Raether. *Surface plasmons on smooth surfaces*. Springer, 1988.

[118] W. L. Barnes, A. Dereux, and T. W. Ebbesen. Surface plasmon subwavelength optics. *Nature*, 424(6950):824–830, 2003.

[119] J. Homola. Surface plasmon resonance sensors for detection of chemical and biological species. *Chemical reviews*, 108(2):462–493, 2008.

[120] K. M. Mayer, S. Lee, H. Liao, B. C. Rostro, A. Fuentes, P. T. Scully, C. L. Nehl, and J. H. Hafner. A label-free immunoassay based upon localized surface plasmon resonance of gold nanorods. *ACS nano*, 2(4):687–692, 2008.

[121] S. Lee, K. M. Mayer, and J. H. Hafner. Improved localized surface plasmon resonance immunoassay with gold bipyramid substrates. *Analytical chemistry*, 81(11):4450–4455, 2009.

[122] C. S. Cheng, Y. Q. Chen, and C. J. Lu. Organic vapour sensing using localized surface plasmon resonance spectrum of metallic nanoparticles self assemble monolayer. *Talanta*, 73(2):358–365, 2007.

[123] K. J. Chen and C. J. Lu. A vapor sensor array using multiple localized surface plasmon resonance bands in a single uv–vis spectrum. *Talanta*, 81(4):1670–1675, 2010.

[124] S. Roh, T. Chung, and B. Lee. Overview of the characteristics of micro-and nanostructured surface plasmon resonance sensors. *Sensors*, 11(2):1565–1588, 2011.

[125] B. Špačková, P. Wrobel, M. Bocková, and J. Homola. Optical biosensors based on plasmonic nanostructures: A review. *Proceedings of the IEEE*, 104(12):2380–2408, 2016.

[126] M. Sun, T. Sun, Y. Liu, L. Zhu, F. Liu, Y. Huang, and C. Chang-Hasnain. Integrated plasmonic refractive index sensor based on grating/metal film resonant structure. In *SPIE OPTO*, pages 97570Q–97570Q. International Society for Optics and Photonics, 2016.

[127] A. González-Cano, M. Navarrete, Ó. Esteban, and N. Díaz-Herrera. Plasmonic sensors based on doubly-deposited tapered optical fibers. *Sensors*, 14(3):4791–4805, 2014.

[128] J. Burgmeier, A. Feizpour, W. Schade, and B. M. Reinhard. Plasmonic nanoshell functionalized etched fiber bragg gratings for highly sensitive refractive index measurements. *Optics letters*, 40(4):546–549, 2015.

[129] S. Palomba, H. Harutyunyan, J. Renger, R. Quidant, N. F. van Hulst, and L. Novotny. Nonlinear plasmonics at planar metal surfaces. *Philosophical Transactions of the Royal Society of London A: Mathematical, Physical and Engineering Sciences*, 369(1950):3497–3509, 2011.

[130] T. Utikal, T. Zentgraf, T. Paul, C. Rockstuhl, F. Lederer, M. Lippitz, and H. Giessen. Towards the origin of the nonlinear response in hybrid plasmonic systems. *Physical review letters*, 106(13):133901, 2011.

[131] H. Harutyunyan, G. Volpe, R. Quidant, and L. Novotny. Enhancing the nonlinear optical response using multifrequency gold-nanowire antennas. *Physical review letters*, 108(21):217403, 2012.

[132] M. Kauranen and A. V. Zayats. Nonlinear plasmonics. *Nature Photonics*, 6(11):737–748, 2012.

[133] M. F. Ciappina, S. S. Aćimović, T. Shaaran, J. Biegert, R. Quidant, and M. Lewenstein. Enhancement of high harmonic generation by confining electron motion in plasmonic nanostrutures. *Optics express*, 20(24):26261–26274, 2012.

[134] A. K. Singh, D. Senapati, S. Wang, J. Griffin, A. Neely, P. Candice, K. M. Naylor, B. Varisli, J. R. Kalluri, and P. C. Ray. Gold nanorod based selective identification of escherichia coli bacteria using two-photon rayleigh scattering spectroscopy. *ACS Nano*, 3(7):1906–1912, 2009.

[135] A. Neely, C. Perry, B. Varisli, A. K. Singh, T. Arbneshi, D. Senapati, J. R. Kalluri, and P. C. Ray. Ultrasensitive and highly selective detection of alzheimers disease biomarker using two-photon rayleigh scattering properties of gold nanoparticle. *ACS Nano*, 3(9):2834–2840, 2009.

[136] M. Mesch, B. Metzger, M. Hentschel, and H. Giessen. Nonlinear plasmonic sensing. *Nano Letters*, 16(5):3155–3159, 2016.

[137] L. Wang, F. Che, S. A. Ponomarenko, and Z. D. Chen. Plasmon-enhanced spectral changes in surface sum-frequency generation with polychromatic light. *Optics express*, 21(12):14159–14168, 2013.

[138] B. H. Ong, X. Yuan, S. C. Tjin, J. Zhang, and H. M. Ng. Optimised film thickness for maximum evanescent field enhancement of a bimetallic film surface plasmon resonance biosensor. *Sensors and Actuators B: Chemical*, 114(2):1028–1034, 2006.

[139] Q. H. Phan, N. Nguyen-Huu, and Y. L. Lo. Optimized double-layered grating structures for chem/biosensing in midinfrared range. *IEEE Sensors Journal*, 14(9):2938–2946, 2014.

[140] S. A. Ponomarenko and E. Wolf. The spectral degree of coherence of fully spatially coherent electromagnetic beams. *Optics communications*, 227(1):73–74, 2003.

[141] J. Homola, I. Koudela, and S. S. Yee. Surface plasmon resonance sensors based on diffraction gratings and prism couplers: sensitivity comparison. *Sensors and Actuators B: Chemical*, 54(1):16–24, 1999.

[142] Z. Chen, X. Zhao, C. Lin, S. Chen, L. Yin, and Y. Ding. Figure of merit enhancement of surface plasmon resonance sensors using absentee layer. *Applied Optics*, 55(25):6832–6835, 2016.

[143] N. Cennamo, D. Massarotti, L. Conte, and L. Zeni. Low cost sensors based on spr in a plastic optical fiber for biosensor implementation. *Sensors*, 11(12):11752–11760, 2011.

[144] J. Homola. Electromagnetic theory of surface plasmons. In *Surface plasmon resonance based sensors*, pages 3–44. Springer, 2006.

[145] Y. Zhong, S. D. Malagari, T. Hamilton, and D. Wasserman. Review of mid-infrared plasmonic materials. *Journal of Nanophotonics*, 9(1):093791–093791, 2015.

[146] J. R. Sambles, G. W. Bradbery, and F. Yang. Optical excitation of surface plasmons: an introduction. *Contemporary physics*, 32(3):173–183, 1991.

[147] X. Huang, P. Zhu, X. Liu, Y. Leng, X. Lu, and H. Wang. Spectral modulation of ultra-broadband femtosecond laser pulses based on surface plasmon resonance. *Optics Communications*, 283(11):2373–2377, 2010.

[148] H. R. Gwon and S. H. Lee. Spectral and angular responses of surface plasmon resonance based on the kretschmann prism configuration. *Materials transactions*, 51(6):1150–1155, 2010.

[149] S. A. Ponomarenko and E. Wolf. Spectral anomalies in a fraunhofer diffraction pattern. *Optics letters*, 27(14):1211–1213, 2002.

[150] F. Bahrami, M. Maisonneuve, M. Meunier, J. S. Aitchison, and M. Mojahedi. An improved refractive index sensor based on genetic optimization of plasmon waveguide resonance. *Optics express*, 21(18):20863–20872, 2013.

[151] A. Majkić, M. Zgonik, A. Petelin, M. Jazbinšek, B. Ruiz, C. Medrano, and P. Günter. Terahertz source at 9.4 thz based on a dual-wavelength infrared laser and quasi-phase matching in organic crystals oh1. *Applied Physics Letters*, 105(14):141115, 2014.

[152] P. Zhao, S. Ragam, Y. J. Ding, and I. B. Zotova. Compact and portable terahertz source by mixing two frequencies generated simultaneously by a single solid-state laser. *Optics letters*, 35(23):3979–3981, 2010.

[153] K. Zhong, J. Mei, M. Wang, P. Liu, D. Xu, Y. Wang, W. Shi, J. Yao, B. Teng, and Y. Xiao. Compact high-repetition-rate monochromatic terahertz source based on difference frequency generation from a dual-wavelength nd: Yag laser and dast crystal. *Journal of Infrared, Millimeter, and Terahertz Waves*, 38(1):87–95, 2017.

[154] Y. T. Chang, H. L. Chang, K. W. Su, and Y. F. Chen. High-efficiency q-switched dual-wavelength emission at 1176 and 559 nm with intracavity raman and sum-frequency generation. *Optics express*, 17(14):11892–11897, 2009.

[155] P. Zhao. Compact terahertz sources based on difference frequency generation. 2012.

[156] N. Nguyen-Huu, M. Cada, Y. Ma, F. Che, J. Pistora, K. Yasumoto, J. Lin, and H. Maeda. Mid-infrared fano resonance in heavily doped silicon and metallic nanostructures due to coupling of wood–rayleigh anomaly and surface plasmons. *Journal of Physics D: Applied Physics*, 50(20):205105, 2017.

[157] L. Mandel and E. Wolf. *Optical Coherence and Quantum Optics*. Cambridge University, 1995.

[158] K. H. Bennemann. *Nonlinear Optics in Metals*. Oxford Science Publications, Oxford, 2003.

[159] K. A. O'Donnell and R. Torre. Characterization of the second-harmonic response of a silver-air interface. *New J. Phys*, 7(1):154, 2005.

[160] F. X. Wang, F. J. Rodrguez, W. M. Albers, and M. Kauranen. Enhancement of bulk-type multipolar second-harmonic generation arising from surface morphology of metals. *New J. Phys*, 12(6):063009, 2010.

[161] M. Scalora, M. A. Vincenti, D. De Ceglia, V. Roppo, M. Centini, N. Akozbek, and M. J. Bloemer. Second-and third-harmonic generation in metal-based structures. *Phys. Rev. A*, 82(4):043828, 2010.

[162] F. X. Wang, F. J. Rodriguez, W. M. Albers, R. Ahorinta, J. E. Sipe, and M. Kauranen. Surface and bulk contributions to the second-order nonlinear optical response of a gold film. *Phys. Rev. B*, 80(23):233402, 2009.

[163] A. Capretti, E. F. Pecora, C. Forestiere, L. D. Negro, and G. Miano. Size-dependent second-harmonic generation from gold nanoparticles. *Phys. Rev. B*, 89(12):125414, 2014.

[164] R. M. Corn and D. A. Higgins. Optical second harmonic generation as a probe of surface chemistry. *Chem. Rev.*, 94(1):107–125, 1994.

[165] D. Krause, C. W. Teplin, and C. T. Rogers. Optical surface second harmonic measurements of isotropic thin-film metals: Gold, silver,copper, aluminum, and tantalum. *J. Appl. Phys.*, 96(7):3626, 2004.

[166] P. Guyot-Sionnest and A. Tadjeddine. Study of ag(111) and au(111) electrodes by optical second-harmonic generation. *Chem. Rev.*, 92(1):734–738, 1990.

[167] C. S. Chang and J. T. Lue. Optical second harmonic generation from thin silver films. *Surface Science*, 393(1-3):231–239, 1997.

Appendix A

Polarization Calculations

The total FW in the glass is a superposition of the incident and reflected waves in Eq. (4.1) and Eq. (4.3). This is given by

$$\mathbf{E}_1(x,z,\omega,\theta_0) = \mathbf{E}_0(x,z,\omega,\theta_0) + \mathbf{E}_r(x,z,\omega,\theta_0). \tag{A.1}$$

The normal component of Eq. (A.1) can be written as

$$\mathbf{E}_{1z}(x,z,\omega,\theta_0) = -\frac{k_x}{k_1}A(\omega)e^{ik_x x}\Big[e^{ik_z z} + \tilde{r}_{12}(\omega,\theta_0)e^{-ik_{1z}z}\Big]\mathbf{e}_z, \tag{A.2}$$

while the tangential component is written as,

$$\mathbf{E}_{1x}(x,z,\omega,\theta_0) = \frac{k_{1z}}{k_1}A(\omega)e^{ik_x x}\Big[e^{ik_z z} - \tilde{r}_{12}(\omega,\theta_0)e^{-ik_{1z}z}\Big]\mathbf{e}_x. \tag{A.3}$$

By applying the electromagnetic boundary conditions to both the normal and tangential components of the electric field on both sides of the boundary at $z = 0$, we can write down the components of electric field, $E_2^<$ on the lower interface of the metal. The normal component of the field is given by

$$\mathbf{E}_{2z}^<(x,z,\omega,\theta_0) = -\frac{k_x}{k_1}\frac{\varepsilon_1}{\varepsilon_2}A(\omega)e^{ik_x x}\Big[1 + \tilde{r}_{12}(\omega,\theta_0)\Big]\mathbf{e}_z, \tag{A.4}$$

while the tangential component is given by

$$\mathbf{E}_{2x}^<(x,z,\omega,\theta_0) = \frac{k_{1z}}{k_1}A(\omega)e^{ik_x x}\Big[1 - \tilde{r}_{12}(\omega,\theta_0)\Big]\mathbf{e}_x. \tag{A.5}$$

The normal and tangential components of the field in the gold thin film are superpositions of the fields transmitted into the film and that reflected from the upper interface of the thin film. They are given respectively by

$$\begin{aligned}\mathbf{E}_{2z}(x,z,\omega,\theta_0) = &-\frac{k_x}{k_2}A(\omega)e^{ik_x x}\frac{t_{12}}{1 + r_{12}r_{23}e^{i2k_{2z}d}} \\ &\times \Big[e^{ik_{2z}z} + r_{23}e^{i2k_{2z}d}e^{-ik_{2z}z}\Big]\mathbf{e}_z,\end{aligned} \tag{A.6}$$

and

$$\begin{aligned}\mathbf{E}_{2x}(x,z,\omega,\theta_0) =& \frac{k_{2z}}{k_2}A(\omega)e^{ik_x x}\frac{t_{12}}{1+r_{12}r_{23}e^{i2k_{2z}d}} \\ &\times\left[e^{ik_{2z}z}-r_{23}e^{i2k_{2z}d}e^{-ik_{2z}z}\right]\mathbf{e}_x.\end{aligned} \tag{A.7}$$

The components of the electric field at the upper interface of the gold film, $E_2^>$ at $z=d$ are calculated similarly to yield

$$\mathbf{E}_{2z}^>(x,z,\omega,\theta_0) = -\frac{k_x}{k_2}A(\omega)e^{ik_x x}R_z(\omega,\theta_0)\mathbf{e}_z, \tag{A.8}$$

and

$$\mathbf{E}_{2x}^>(x,z,\omega,\theta_0) = -\frac{k_{2z}}{k_2}A(\omega)e^{ik_x x}R_x(\omega,\theta_0)\mathbf{e}_x, \tag{A.9}$$

where

$$\begin{aligned}R_z(\omega,\theta_0) &= \frac{t_{12}(1+r_{23})e^{i2k_z d}}{1+r_{12}r_{23}e^{i2k_{2z}d}}, \\ R_x(\omega,\theta_0) &= \frac{t_{12}(1-r_{23})e^{i2k_z d}}{1+r_{12}r_{23}e^{i2k_{2z}d}}.\end{aligned} \tag{A.10}$$

The polarization at the lower interface of the thin film, $P_{x,z}^<$ can then be determined using the electric field components at the lower interface and Eq. (4.6), yielding

$$\begin{aligned}\mathbf{P}_z^<(\mathbf{x},\omega_3,\theta_0) &= \varepsilon_0\int_{-\infty}^{\infty}\frac{d\omega_1}{2\pi}\chi_{S,zzz}^{(2)}(\omega_3;\omega_1,\omega_2)E_{2z}^<(\mathbf{x},\omega_1,\theta_0)E_{2z}^{*<}(\mathbf{x},\omega_2,\theta_0), \\ &= \mathbf{e}_z P_{0z}^<(\omega_3,\theta_0)e^{ik_x(\omega_3)x},\end{aligned} \tag{A.11}$$

$$\begin{aligned}\mathbf{P}_x^<(\mathbf{x},\omega_3,\theta_0) &= \varepsilon_0\int_{-\infty}^{\infty}\frac{d\omega_1}{2\pi}\chi_{S,xzx}^{(2)}(\omega_3;\omega_1,\omega_2)E_{2z}^<(\mathbf{x},\omega_1,\theta_0)E_{2x}^{*<}(\mathbf{x},\omega_2,\theta_0) \\ &+\varepsilon_0\int_{-\infty}^{\infty}\frac{d\omega_1}{2\pi}\chi_{S,xxz}^{(2)}(\omega_3;\omega_1,\omega_2)E_{2x}^<(\mathbf{x},\omega_1,\theta_0)E_{2z}^{*<}(\mathbf{x},\omega_2,\theta_0), \\ &= \mathbf{e}_x P_{0x}^<(\omega_3,\theta_0)e^{ik_x(\omega_3)x}.\end{aligned} \tag{A.12}$$

Here $P_{0z}^<$ and $P_{0x}^<$ are defined respectively as

$$\begin{aligned}P_{0z}^<(\omega_3,\theta_0) = \varepsilon_0\sin^2\theta\,\varepsilon_1^2\int_{-\infty}^{\infty}\frac{d\omega_1}{2\pi}\chi_{S,zzz}^{(2)}(\omega_3;\omega_1,\omega_2)\frac{A(\omega_1)A^*(\omega_2)}{\varepsilon_2(\omega_1)\varepsilon_2^*(\omega_2)} \\ \times(1+\tilde{r_{12}}(\omega_1,\theta_0))(1+\tilde{r}_{12}^*(\omega_2,\theta_0)),\end{aligned} \tag{A.13}$$

$$
\begin{aligned}
P_{0x}^{<}(\omega_3,\theta_0) &= \varepsilon_0 \sin\theta_0 \cos\theta_0 \varepsilon_1 \int_{-\infty}^{\infty} \frac{d\omega_1}{2\pi} \chi_{S,xzx}^{(2)}(\omega_3;\omega_1,\omega_2) \frac{A(\omega_1)A^*(\omega_2)}{\varepsilon_2(\omega_1)} \\
&\times (1+\tilde{r}_{12}(\omega_1,\theta_0))(1-\tilde{r}_{12}^*(\omega_2,\theta_0)) \\
&+ \varepsilon_0 \sin\theta_0 \cos\theta_0 \varepsilon_1 \int_{-\infty}^{\infty} \frac{d\omega_1}{2\pi} \chi_{S,xxz}^{(2)}(\omega_3;\omega_1,\omega_2) \frac{A(\omega_1)A^*(\omega_2)}{\varepsilon_2^*(\omega_2)} \\
&\times (1-\tilde{r}_{12}(\omega_1,\theta_0))(1+\tilde{r}_{12}^*(\omega_2,\theta_0)).
\end{aligned} \tag{A.14}
$$

Similarly, the polarization of the upper interface on the metal thin film, $P_{x,z}^{>}$ is given by

$$
\begin{aligned}
\mathbf{P}_z^{>}(\mathbf{x},\omega_3,\theta_0) &= \varepsilon_0 \int_{-\infty}^{\infty} \frac{d\omega_1}{2\pi} \chi_{S,xzx}^{(2)}(\omega_3;\omega_1,\omega_2) E_{2z}^{>}(\mathbf{x},\omega_1,\theta_0) E_{2z}^{*>}(\mathbf{x},\omega_2,\theta_0), \\
&= \mathbf{e}_z P_{0z}^{>}(\omega_3,\theta_0) e^{ik_x(\omega_3)x},
\end{aligned} \tag{A.15}
$$

$$
\begin{aligned}
\mathbf{P}_x^{>}(\mathbf{x},\omega_3,\theta_0) &= \varepsilon_0 \int_{-\infty}^{\infty} \frac{d\omega_1}{2\pi} \chi_{S,xzx}^{(2)}(\omega_3;\omega_1,\omega_2) E_{2z}^{>}(\mathbf{x},\omega_1,\theta_0) E_{2x}^{*>}(\mathbf{x},\omega_2,\theta_0) \\
&+ \varepsilon_0 \int_{-\infty}^{\infty} \frac{d\omega_1}{2\pi} \chi_{S,xxz}^{(2)}(\omega_3;\omega_1,\omega_2) E_{2x}^{>}(\mathbf{x},\omega_1,\theta_0) E_{2z}^{*>}(\mathbf{x},\omega_2,\theta_0), \\
&= \mathbf{e}_x P_{0x}^{>}(\omega_3,\theta_0) e^{ik_x(\omega_3)x}.
\end{aligned} \tag{A.16}
$$

Here $P_{0z}^{>}$ and $P_{0x}^{>}$ are

$$
\begin{aligned}
P_{0z}^{>}(\omega_3,\theta_0) &= \varepsilon_0 \sin^2\theta \varepsilon_1 \int_{-\infty}^{\infty} \frac{d\omega_1}{2\pi} \chi_{S,zzz}^{(2)}(\omega_3;\omega_1,\omega_2) \frac{A(\omega_1)A^*(\omega_2)}{\sqrt{\varepsilon_2(\omega_1)}\sqrt{\varepsilon_2^*(\omega_2)}} \\
&\times R_z(\omega_1,\theta_0) R_z^*(\omega_2,\theta_0)
\end{aligned} \tag{A.17}
$$

$$
\begin{aligned}
P_{0x}^{>}(\omega_3,\theta_0) &= \varepsilon_0 \sin\theta_0 \sqrt{\varepsilon_1} \int_{-\infty}^{\infty} \frac{d\omega_1}{2\pi} \chi_{S,xzx}^{(2)}(\omega_3;\omega_1,\omega_2) \frac{A(\omega_1)A^*(\omega_2)}{\sqrt{\varepsilon_2(\omega_1)}} \\
&\times \Big[\frac{\sqrt{\varepsilon_2(\omega_2)-\varepsilon_1\sin^2\theta}}{\sqrt{\varepsilon_2(\omega_2)}}\Big]^* R_z(\omega_1,\theta_0) R_x^*(\omega_2,\theta_0) \\
&+ \varepsilon_0 \sin\theta_0 \sqrt{\varepsilon_1} \int_{-\infty}^{\infty} \frac{d\omega_1}{2\pi} \chi_{S,xxz}^{(2)}(\omega_3;\omega_1,\omega_2) \frac{A(\omega_1)A^*(\omega_2)}{\sqrt{\varepsilon_2^*(\omega_2)}} \\
&\times \Big[\frac{\sqrt{\varepsilon_2(\omega_1)-\varepsilon_1\sin^2\theta}}{\sqrt{\varepsilon_2(\omega_1)}}\Big] R_x(\omega_1,\theta_0) R_z^*(\omega_2,\theta_0).
\end{aligned} \tag{A.18}
$$

Appendix B

Matlab Codes for Simulating Nonlinear Wave Generation

```
%************************************************************************
%     Nonlinear spectrum caculations  using a polychromatic plane wave
%************************************************************************


clear
clc

%************************************************************************
%     Parameters
%************************************************************************

cc=2.99792458e8;            %speed of light in free space
mu0=4.0*pi*1.0e-7;          %permeability of free space
eps0=1.0/(cc*cc*mu0);       %permittivity of free space


epsr1=2.25;                 %permittivity of glass
epsr3=1.0;                  %permittivity of air
d=50.0e-9;                  %thickness of the gold film

omega0 = 2.325495762109696e+15;  % 810 nm, centre frequency of FW
omega30=2.446300736764744e+14; % 7.70 um, centre frequency, DFW

omegaL=omega0-1.1e15;
omegaU=omega0+1.1e15;


omega3l=omega30-1.4e14;
omega3u=omega30+1.5e14;
```

```
thetail=40.0;          %Minimum angle of incidence
thetaiu=46.0;          %Maximum angle of incidence

d_omega1=omega0*0.01;          %Integration step size
d_omega3=omega30*0.01;
d_thetai=0.01/180.0*pi;

%*************************************************************************
%     loop 1: DF angular frequency
%*************************************************************************

ii=1;
for     omega3=omega3l:d_omega3:omega3u

    lambda3=2.0*pi*cc/omega3;  %wavelength

    epsr2_w3=IB_7700(lambda3);    %frequency dependent permittivity

    k1_w3=sqrt(epsr1)*omega3/cc;  %wave number in glass
    k2_w3=sqrt(epsr2_w3)*omega3/cc; %wave number in gold film
    k3_w3=sqrt(epsr3)*omega3/cc;  %wave number in air

%*************************************************************************
%     loop 1.1: incident angle
%*************************************************************************

    jj=1;
    for thetai=thetail/180.0*pi:d_thetai:thetaiu/180.0*pi


        kx_w3=k1_w3*sin(thetai);    %wave number components of SH
        k1z_w3=sqrt(k1_w3^2-kx_w3^2);
        k2z_w3=sqrt(k2_w3^2-kx_w3^2);
        k3z_w3=sqrt(k3_w3^2-kx_w3^2);

%*************************************************************************
%     loop 1.2: Fundamental angular frequency
%*************************************************************************
```

```
        sum1z=0.0;                              %for integral caculation
        sum2z=0.0;
        sum1x=0.0;                              %for integral caculation
        sum2x=0.0;

        kkk=1;
        for omega1=omegaL:d_omega1:omegaU % linear frequency scan

%'Fresnel' calculates  \epsilon, wavevectors and spectral amplitudes
[F1_w1,F2_w1,F11_w1,A1,epsr2_w1,kxk2_w1,kzk2_w1,F22_w1]...
 =Fresnel(omega1,thetai);

            omega2=omega3-omega1;

%'Fresnel' calculates  \epsilon, wavevectors and spectral amplitudes
[F1_w2,F2_w2,F11_w2,A2,epsr2_w2,kxk2_w2,kzk2_w2,F22_w2]...
 =Fresnel(omega2,thetai);


 %Second-order surface susceptibilities
  kaizzz=kai_zzz_new(epsr2_w1,epsr2_w2,omega1,omega2);



  kaixzx=kai_xzx_new(epsr2_w1,omega1,omega2,omega3);
  kaixxz=kai_xxz_new(epsr2_w2,omega1,omega2,omega3);

  %Intergral caculation
  I1z=kaizzz*F1_w1*A1*conj(F1_w2)*A2*d_omega1/(epsr2_w1...
  *conj(epsr2_w2));
  I2z=kaizzz*F2_w1*A1*conj(F2_w2)*A2*d_omega1/(sqrt(epsr2_w1)...
  *conj(sqrt(epsr2_w2)));

  I1x=kaixzx*F1_w1*A1*conj(F11_w2)*A2*d_omega1/epsr2_w1 +...
  kaixxz*conj(F1_w2)*A1*(F11_w1)*A2*d_omega1/conj(epsr2_w2);

  I2x=kaixzx*F2_w1*A1*conj(F22_w2)*A2*kxk2_w1*conj(kzk2_w2)...
  *d_omega1 + kaixxz*conj(F2_w2)*A1*(F22_w1)*A2*conj(kxk2_w2)...
  *(kzk2_w1)*d_omega1;
```

```
%
        sum1z=sum1z+I1z;
        sum2z=sum2z+I2z;
        sum1x=sum1x+I1x;
        sum2x=sum2x+I2x;

            kkk=kkk+1;
        end

        Ilz=sum1z;
        Ilx=sum1x;

        Iuz=sum2z;
        Iux=sum2x;



    p0lz=eps0*epsr1^2*sin(thetai)^2*Ilz/2.0/pi;    %lower interface
    p0lx=eps0*epsr1*sin(thetai)*cos(thetai)*Ilx/2.0/pi;%lower interface

    p0uz=1*eps0*epsr1*sin(thetai)^2*Iuz/2.0/pi;      %upper interface
    p0ux=1*eps0*Iux/2.0/pi;                          %upper interface

    %Fresnel coefficient at SH frequencies
     r122=(epsr2_w3*k1z_w3-epsr1*k2z_w3)/(epsr2_w3*k1z_w3+epsr1*k2z_w3);
     r232=(epsr3*k2z_w3-epsr2_w3*k3z_w3)/(epsr3*k2z_w3+epsr2_w3*k3z_w3);
     t212=2.0*sqrt(epsr1*epsr2_w3)*k2z_w3/(epsr1*k2z_w3+epsr2_w3*k1z_w3);

     frsl=r232*t212*exp(2.0*1i*k2z_w3*d)/(1.0+r122*r232...
         *exp(2.0*1i*k2z_w3*d));
     frsu=t212*exp(1i*k2z_w3*d)/(1.0+r122*r232*exp(2.0*1i*k2z_w3*d));

    %DFW calculations based on Eqn (16) and (17) of "Giant spectral
    %transformations in plasmon-enhanced difference-frequency
    %generation with polychromatic light"
     Ex1 = 1i*omega3*(-sin(thetai)*p0lz + cos(thetai)*p0lx)...
         /(4*pi*cc*sqrt(epsr1*eps0));
     Ex2 = 1i*omega3*(-sin(thetai)*p0lz + cos(thetai)*p0lx)...
```

```
        *frsl/(4*pi*cc*sqrt(epsr2_w3*eps0));
    Ex3 = 1i*omega3*(-sin(thetai)*p0uz + cos(thetai)*p0ux)...
        *frsu/(4*pi*cc*sqrt(epsr2_w3*eps0));


    Ez1 = 1i*omega3*sin(thetai)*(-1*p0lx + tan(thetai)*p0lz)...
        /(4*pi*cc*sqrt(epsr1*eps0));
    Ez2 = 1i*omega3*sin(thetai)*(-1*p0lx + tan(thetai)*p0lz)...


        *frsl/(4*pi*cc*sqrt(epsr2_w3*eps0));
    Ez3 = 1i*omega3*sin(thetai)*(-1*p0ux + tan(thetai)*p0uz)...
        *frsu/(4*pi*cc*sqrt(epsr2_w3*eps0));

       Ex = Ex1 + Ex2 + Ex3;
       Ez = Ez1 + Ez2 + Ez3;

       S2(jj,ii)=abs(Ex.^2) + abs(Ez.^2);


        jj=jj+1;
    end

%************************************************************************
%     End varible loop
%************************************************************************

    ii=ii+1;
end

%Normalized Intensity
```

Appendix C

Copyright Permissions

From: Franklin Che [franklin.che@dal.ca]

Sent: Fri 6/23/2017 4:08 PM
To: permissions@iop.org;

Subject: Copyright Permission

Dear Institute of Physics Publishing,

I am the first author of the following journal article, while I was working toward my PhD degree. Now, I am preparing my PhD thesis for submission to the Faculty of Graduate Studies at Dalhousie University, Halifax, Nova Scotia, Canada. I am seeking your permission to include a manuscript version of the following paper as a chapter in the thesis.

1. F. Che, S. A. Ponomarenko, and M. Cada, Giant spectral transformations in plasmon-enhanced difference-frequency generation with polychromatic light, Journal of Optics, vol. 18, no. 12, p. 125503, 2016.

Full publication details and a copy of this permission letter will be included in the thesis.

Best Regards,
Franklin Che.

From: Kathryn Shaw [Kathryn.Shaw@iop.org]

Sent: Mon 6/26/2017 6:27 AM

To: Franklin Che;

Subject: RE: Copyright Permission

Dear Franklin Che,

Thank you for your request to reproduce IOP Publishing material.

Regarding:

Franklin Che et al 2016 J. Opt. 18 125503

The material you have requested was published under a CC BY licence (http://creativecommons.org/licenses/by/3.0/). Therefore you may reuse the content without permission, so long as you reference it adequately and adhere to the terms of the CC BY licence. Please note this does not apply to any material/figure which is credited to another source in our publication or has been obtained from a third party, which is not available under a suitable open access licence. Express permission for such materials/figures must be obtained from the copyright owner. If you have any further questions or if there is any more we can do to help, please let me know.
Kind regards,
Kathryn Shaw

Copyright and Permissions Team
Gemma Alaway Senior Rights and Permissions Adviser
Kathryn Shaw - Rights and Permissions Assistant

From: Franklin Che [franklin.che@dal.ca]
Sent: Fri 6/23/2017 4:19 PM
To: pubs-permissions@ieee.org;
Subject: Copyright Permission

Dear IEEE,
I am the first author of the following journal article, while I was working toward my PhD degree. Now, I am preparing my PhD thesis for submission to the Faculty of Graduate Studies at Dalhousie University, Halifax, Nova Scotia, Canada. I am seeking your permission to include a manuscript version of the following paper as a chapter in the thesis.
1. Che, F., Ponomarenko, S. A., Cada, M., and Nguyen-Huu, N. 2017. High Sensitivity Integrated Visible to Mid-Infrared Nonlinear Plasmonic Sensor. IEEE Photonics Journal.

Full publication details and a copy of this permission letter will be included in the thesis.

Best Regards,
Franklin Che.

From: M.E Brennan [me.brennan@ieee.org]

Sent: Mon 6/26/2017 10:23 AM

To: Franklin Che;

Subject: RE: Copyright Permission

Dear Franklin Che,

The IEEE does not require individuals working on a thesis to obtain a formal reuse license however, you must follow the requirements listed below:

Textual Material

Using short quotes or referring to the work within these papers) users must give full credit to the original source (author, paper, publication) followed by the IEEE copyright line [Year of publication] IEEE.

In the case of illustrations or tabular material, we require that the copyright line [Year of original publication] IEEE appear prominently with each reprinted figure and/or table. If a substantial portion of the original paper is to be used, and if you are not the senior author, also obtain the senior authors approval.

Full-Text Article

If you are using the entire IEEE copyright owned article, the following IEEE copyright/ credit notice should be placed prominently in the references: [year of original publication] IEEE. Reprinted, with permission, from [author names, paper title, IEEE publication title, and month/year of publication]

Only the accepted version of an IEEE copyrighted paper can be used when posting the paper or your thesis on-line. You may not use the final published version

In placing the thesis on the author's university website, please display the following message in a prominent place on the website: In reference to IEEE copyrighted material which is used with permission in this thesis, the IEEE does not endorse any of [university/educational entity's name goes here]'s products or services. Internal or personal use of this material is permitted. If interested in reprinting/republishing IEEE copyrighted material for advertising or promotional purposes or for creating new collective works for resale or redistribution, please go to
http://www.ieee.org/publications.standards/publications/rights/rights.link.html to learn how to obtain a License from RightsLink.

If applicable, University Microfilms and/or ProQuest Library, or the Archives of Canada

may supply single copies of the dissertation.

kind regards,

M.E. Brennan

Ms M.E. Brennan
IEEE
501 Hoes Lane
Piscataway, NJ 08854-4141 USA
me.brennan@ieee.org

+1 (732) 562-2660

From: Franklin Che [franklin.che@dal.ca]

Sent: Friday, June 23, 2017 3:16 PM
To: permissionshelpdesk@elsevier.com;

Subject: Copyright Permission

Dear Elsevier,

I am the first author of the following journal article, while I was working toward my PhD degree. Now, I am preparing my PhD thesis for submission to the Faculty of Graduate Studies at Dalhousie University, Halifax, Nova Scotia, Canada. I am seeking your permission to include a manuscript version of the following paper as a chapter in the thesis.

F. Che, S. Grabtchak, W. M. Whelan, S. A. Ponomarenko, and M. Cada, Relative shg measurements of metal thin films: Gold, silver, aluminum, cobalt, chromium, germanium, nickel, antimony, titanium, titanium nitride, tungsten, zinc, silicon and indium tin oxide, Results in Physics, vol. 7, pp. 593595, 2017.

Full publication details and a copy of this permission letter will be included in the thesis.

Best Regards,
Franklin Che.

From: pubs Permission [pubs-permissions+noreply@ieee.org]

Sent: Fri 6/30/2017 12:36 PM

To: Franklin Che;

Subject: RE: Copyright Permission

Dear Mr Che:.

As an Elsevier journal author, you retain the right to Include the article in a thesis or dissertation (provided that this is not to be published commercially) whether in full or in part, subject to proper acknowledgment; see https://www.elsevier.com/about/our-business/policies/copyright/personal-use for more information. As this is a retained right, no written permission from Elsevier is necessary.

If I may be of further assistance, please let me know.

Best of luck with your PhD thesis and best regards, Hop

Hop Wechsler
Permissions Helpdesk Manager
ELSEVIER — Global E-Operations Books
+1 215-239-3520 office
h.wechsler@elsevier.com

Contact the Permissions Helpdesk
+1 800-523-4069 x3808 — permissionshelpdesk@elsevier.com